

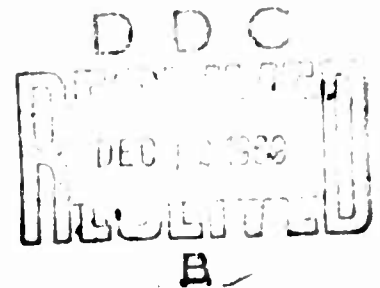
AD 697988

# THE TEMPERATURE DEPENDENCE OF THE THERMAL CONTACT RESISTANCE ACROSS NONMETALLIC INTERFACES

MERRILL L. MINGES

TECHNICAL REPORT AFML-TR-69-1

OCTOBER 1969



This document has been approved for public release and sale;  
its distribution is unlimited.

U.S. GOVERNMENT PRINTING OFFICE  
CLEARINGHOUSE  
WASHINGTON, D.C. 20540  
For sale by the Superintendent of Documents  
Stock Number 28-7520-1

AIR FORCE MATERIALS LABORATORY  
AIR FORCE SYSTEMS COMMAND  
WRIGHT-PATTERSON AIR FORCE BASE, OHIO

166

## NOTICE

When Government drawings, specifications, or other data are used for any purpose other than in connection with a definitely related Government procurement operation, the United States Government thereby incurs no responsibility nor any obligation whatsoever; and the fact that the Government may have formulated, furnished, or in any way supplied the said drawings, specifications, or other data, is not to be regarded by implication or otherwise as in any manner licensing the holder or any other person or corporation, or conveying any rights or permission to manufacture, use, or sell any patented invention that may in any way be related thereto.

This document has been approved for public release and sale; its distribution is unlimited.

WHITE SECTION <input checked="" type="checkbox"/>	
BUFF SECTION <input type="checkbox"/>	
<input type="checkbox"/>	
ENTER BOTTOM AVAILABILITY CODES	
DIST.	AVAIL. AND OF SPECIAL
↑	

Copies of this report should not be returned unless return is required by security considerations, contractual obligations, or notice on a specific document.

AFML-TR-69-1

**THE TEMPERATURE DEPENDENCE OF THE  
THERMAL CONTACT RESISTANCE ACROSS  
NONMETALLIC INTERFACES**

*MERRILL L. MINGES*

This document has been approved for public release and sale;  
its distribution is unlimited.

FOREWORD

This report was prepared under Project 7381 "Materials Applications," Task 738102, "Space, Missile, and Propulsion Systems Material and Component Evaluation," with Dr. Merrill L. Minges acting as the project engineer. The experimental research work and the analytical correlations were carried out over the period from 1 June 1966 to 1 October 1968.

This report is a follow-on to the thermal contact resistance literature analysis presented in AFML-TR-65-375, Vol I, and replaces Volumes II and III of that document.

The manuscript was released by the author in December 1968 for publication as an AFML Technical Report.

This technical report has been reviewed and is approved.



L. N. HJELM, Chief  
Space & Missiles Systems Support Branch  
Materials Support Division  
AF Materials Laboratory



## ABSTRACT

Extensive measurements of thermal contact resistance were conducted in the following study areas, where no previous systematic measurements have been performed: (1) interfaces consisting of brittle, nonmetallic components, and (2) radiative transport across the interface at high temperatures.

An apparatus for performing the measurements to elevated temperatures was designed, constructed, and performance tested. The equipment, operated in vacuum environments, utilized tantalum heaters to develop heat flow down a specimen column which was water cooled at its base. The contact resistance specimen column consisted of two high purity beryllium oxide cylinders, 1 inch in diameter and 1.5 inches in length. The successful performance of the apparatus was demonstrated by measuring the thermal conductivity of beryllium oxide and tantalum as a function of temperature. The beryllium oxide and tantalum conductivity results exhibited a precision of at least  $\pm 2\%$  while the accuracy of the data was estimated to be  $\pm 3\%$  by comparison with literature values.

Analytical predictions of heat losses from the specimen column were made through solution of the boundary-value problem for the temperature field in the insulation segment surrounding this column. The results compared favorably with experimental heat loss measurements.

The contact resistance of beryllium oxide interfaces with two levels of surface roughness were measured: (1) a sandblasted and partially polished combination exhibiting a nominal  $10\ \mu$  in. CLA random-lay finish, and (2) an interface with sandblasted surfaces exhibiting a nominal  $40\ \mu$  in. CLA random-lay finish. Quantitative surface roughness and waviness analyses were performed with a Talysurf Profilometer.

Contact resistance as a function of mean interface temperature was measured for the above mentioned combinations from about  $200^\circ\text{F}$  to  $1600^\circ\text{F}$  at 5 deadweight compressive loads ranging from 5 to 500 psi. The reciprocal of the contact resistance, the thermal contact conductance, exhibited the following trends:

- a. The values for the smoother  $10\ \mu$  in. interface were higher by a factor of 3 to 4 than those for the  $40\ \mu$  in. interface at comparable compressive load levels.

b. The values increased rapidly with compressive load.

c. Radiative heat transport across the interfaces was important at high temperatures, particularly at low compressive load levels. This contribution increases by a factor of up to 20 in the temperature range from 200 to 1600°F and was a major contributor to the net interfacial heat transport.

d. The compressive load on the interface serves to reduce the relative contributions of radiative transport indirectly by preventing the generation of large interfacial temperature drops at higher temperatures.

A combined roughness-waviness interfacial heat transfer model was formulated which successfully correlated the experimental measurements within 10%, including the contributions of high temperature radiative transport across the contact. The thermal resistance induced by surface waviness were in series with those induced by the roughness, the combination being in parallel with the thermal resistance across the radiation gap regions.

The nonlinear character of the radiative transport effects were successfully incorporated in a finite-element temperature field analysis that exhibited stable convergence over wide ranges of radiation heat transfer coefficient.

The relative contributions of radiative and conductive transport across the interface and their combined influence on the temperature field distortion were characterized by a dimensionless interfacial heat transport modulus,  $H_I = h_R \ell / k$ . This group was proportional to the 4.4 power of the mean interface temperature,  $T_m$ , expressed in °R; a 4.0 dependence was predicted theoretically for the beryllium oxide interface.

A simplified analytical procedure for predicting the temperature dependency of the thermal contact conductance was also developed and applied successfully giving essentially the same results as the more detailed combined model analysis. This simplified procedure was partially empirical in nature, however.

## TABLE OF CONTENTS

SECTION	PAGE
I INTRODUCTION	1
II APPARATUS CONSTRUCTION AND QUALIFICATION TESTING	5
A. Equipment Development	5
B. Design Considerations	13
1. Design Philosophy	13
2. Instrumentation	13
3. Heat Loss Analysis	17
C. Apparatus Performance	24
1. Thermal Conductivity Specimens	24
2. Thermal Conductivity Measurements on BeO	27
3. Thermal Conductivity Measurements on Tantalum	30
4. Heat Loss Measurements	33
III CONTACT RESISTANCE RESULTS	37
A. Contact Surface Characterization	37
B. Measurement Procedure	42
C. Graphical Presentation and Qualitative Interpretation of Results	45
IV DISCUSSION OF RESULTS	60
A. Formulation of the Contact Model	60
1. General Contact Characteristics	60
2. Surface Roughness	62
3. Surface Waviness	64
4. The Combined Model	73
B. Comparison of Analytically Predicted Results with Experimental Measurements	76
1. Input Parameters	76

## TABLE OF CONTENTS (Contd)

SECTION	PAGE
2. Analytically Developed Contact Conductances	78
C. A Simplified Analytical Prediction Procedure	87
V CONCLUSIONS AND RECOMMENDATIONS	90
A. Conclusions	90
B. Recommendations	92
APPENDIX I. HEAT LOSS ANALYSIS	97
A. Solution Considering Boundary Condition 4	97
B. Solution Considering Boundary Conditions 1 and 2	102
C. Evaluation of Fourier Coefficient Integrals	108
APPENDIX II. FINITE ELEMENT ANALYSIS	118
A. Nodal Equation Derivations	118
B. Numerical Evaluation	125
APPENDIX III. PHYSICAL PROPERTY DATA	127
A. Thermal Conductivity of the Alumina Bubble Insulation	127
B. Beryllium Oxide Emittance Data	129
APPENDIX IV. TABULATED EXPERIMENTAL DATA	134
A. Beryllium Oxide Thermal Conductivity Data	134
B. Tantalum Thermal Conductivity Data	135
C. Thermal Contact Resistance Data	135
REFERENCES	146-148

## LIST OF ILLUSTRATIONS

FIGURE		PAGE
1.	Schematic of Cut-Bar Comparative Conductance Apparatus	6
2.	Contact Resistance Apparatus Cross-Section	8
3.	Assembled Components	10
4.	Overall View of the Control - Instrumentation Assembly	11
5.	Assembled Test Cell Including Load Column	12
6.	Perturbation of Heat Flow From a Nonconducting Cylinder in an Isotropic Media	15
7.	Temperature Field Perturbation as a Function of Specimen Conductivity	17
8.	Insulation Segment and Boundary Conditions	18
9.	Typical Temperature Distributions During BeO Thermal Conductivity Measurements	28
10.	Thermal Conductivity of Beryllium Oxide as a Function of Temperature	29
11.	Thermal Conductivity of Beryllium Oxide Plotted as a Function of $(1/T)$	31
12.	Thermal Conductivity of Tantalum as a Function of Temperature	32
13.	Surface Characterization Equipment	38
14.	Surface Roughness Profile Traces	39
15.	Surface Waviness Profile Trace	40
16.	Solid Area as a Function of Vertical Displacement	41
17.	Contact Conductance as a Function of Interface Temperature: 40 $\mu$ in./40 $\mu$ in. Interface, 5.92 psia Compressive Load	46
18.	Contact Conductance as a Function of Interface Temperature: 40 $\mu$ in./40 $\mu$ in. Interface, 65.2 psia Compressive Load	47
19.	Contact Conductance as a Function of Interface Temperature: 40 $\mu$ in./40 $\mu$ in. Interface, 149.3 psia Compressive Load	48
20.	Contact Conductance as a Function of Interface Temperature: 40 $\mu$ in./40 $\mu$ in. Interface, 368.6 psia Compressive Load	49

## LIST OF ILLUSTRATIONS (Contd)

FIGURE		PAGE
21.	Contact Conductance as a Function of Interface Temperature: 40 $\mu$ in./40 $\mu$ in. Interface, 511.5 psia Compressive Load	50
22.	Contact Conductance as a Function of Interface Temperature: 10 $\mu$ in./10 $\mu$ in. Interface, 4.43 psia Compressive Load	51
23.	Contact Conductance as a Function of Interface Temperature: 10 $\mu$ in./10 $\mu$ in. Interface, 64.7 psia Compressive Load	52
24.	Contact Conductance as a Function of Interface Temperature: 10 $\mu$ in./10 $\mu$ in. Interface, 148.7 psia Compressive Load	53
25.	Contact Conductance as a Function of Interface Temperature: 10 $\mu$ in./10 $\mu$ in. Interface, 368.5 psia Compressive Load	54
26.	Contact Conductance as a Function of Interface Temperature: 10 $\mu$ in./10 $\mu$ in. Interface, 512.0 psia Compressive Load	55
27.	Vacuum and Inert Gas Environment Contact Resistance Results: 40 $\mu$ in./40 $\mu$ in. Interface	58
28.	Vacuum and Inert Gas Environment Contact Resistance Results: 10 $\mu$ in./10 $\mu$ in. Interface	59
29.	Flux Field Distribution at an Interface	60
30.	Idealized Contact Element and Associated Heat Flux - Temperature Field	63
31.	Contact Element Quadrant	66
32.	Finite Element Nodal Point Definitions	67
33.	Isotherm Distribution in the Contact Element Quadrant with Normal Radiation Heat Transfer Coefficient	71
34.	Isotherm Distribution in the Contact Element Quadrant with Increased Radiation Heat Transfer Coefficient	72
35.	Combined Model Resistance Analog	75
35.	Experimental-Analytical Contact Conductance Comparisons: 10 $\mu$ in. Interface	83
37.	Experimental-Analytical Contact Conductance Comparisons: 40 $\mu$ in. Interface	84
38.	Interfacial Heat Transport Modulus for the 10 and 40 $\mu$ in. Interfaces	86

## LIST OF ILLUSTRATIONS (Contd)

FIGURE		PAGE
39.	Experimental-Analytical Contact Conductance Comparisons: Simplified Analysis - 10 $\mu$ in. Interface	88
40.	Experimental-Analytical Contact Conductance Comparisons: Simplified Analysis - 40 $\mu$ in. Interface	89
41.	Thermal Conductivity of Aluminum Oxide Powder Insulations	128
42.	Spectral Normal Emittance of Beryllium Oxide in the Infrared	130
43.	Total Normal Emittance of Beryllium Oxide as a Function of Temperature	132

## LIST OF TABLES

TABLE		PAGE
I	Positive Roots of $u_0(K_n; r_0; r_1) = 0$ When $r_1/r_0 = 6.0$	24
II	Composition of Beryllium Oxide Test Specimens	25
III	Composition of Tantalum Test Specimens	26
IV	Experimental - Analytical Heat Exchange Comparison	34
V	Contact Resistance Error Analysis Results	44
VI	Nodal Equation Summary	68
VII	Effective Gap Width Comparisons	74
VIII	Surface Geometry Parameters	77
IX	Roughness-Waviness Contact Resistance Results	81
X	Interfacial Heat Transport Modulus Results, $H_I$	82
XI	BeO Thermal Conductivity Guarding Data	115
XII	Adjusted Temperature Distribution Data	116
XIII	"First Guess" Temperature Distribution	125
XIV	Nodal Equations for Computer Evaluation	126
XV	Beryllium Oxide Emittance Specimen Characteristics	133
XVI	BeO Thermal Conductivity Results	134
XVII	Tantalum Thermal Conductivity Results	135
XVIII	Thermal Contact Conductance Results - $40 \mu\text{in.}/40 \mu\text{in.}$ Interface: 5.02 psia Compressive Load	136
XIX	Thermal Contact Conductance Results - $40 \mu\text{in.}/40 \mu\text{in.}$ Interface: 65.2 psia Compressive Load	137
XX	Thermal Contact Conductance Results - $40 \mu\text{in.}/40 \mu\text{in.}$ Interface: 149.3 psi Compressive Load	138
XXI	Thermal Contact Conductance Results - $40 \mu\text{in.}/40 \mu\text{in.}$ Interface: 368.6 psi Compressive Load	139
XXII	Thermal Contact Conductance Results - $40 \mu\text{in.}/40 \mu\text{in.}$ Interface: 511.5 psi Compressive Load	140



## LIST OF TABLES (CONTD)

TABLE		PAGE
XXIII	Thermal Contact Conductance Results - 10 $\mu$ in./10 $\mu$ in. Interface: 4.43 psia Compressive Load	141
XXIV	Thermal Contact Conductance Results - 10 $\mu$ in./10 $\mu$ in. Interface: 64.7 psi Compressive Load	142
XXV	Thermal Contact Conductance Results - 10 $\mu$ in./10 $\mu$ in. Interface: 148.7 psia Compressive Load	143
XXVI	Thermal Contact Conductance Results - 10 $\mu$ in./10 $\mu$ in. Interface: 368.5 psia Compressive Load	144
XXVII	Thermal Contact Conductance Results - 10 $\mu$ in./10 $\mu$ in. Interface: 512.0 psia Compressive Load	145

## NOMENCLATURE

$a$	solid contact area radius, in.
$A$	cross-sectional area, $\text{ft}^2$
$b$	adiabatic contact element radius, in.
$C_v$	heat capacity at constant volume, $\text{BTU/lb-}^\circ\text{F}$
$\bar{d}$	average particle diameter, microns
$D(r, z)$	geometrical factor
$E_{\text{BB}}$	blackbody emissive power, $\text{BTU/hr-ft}^2$
$\mathcal{F}$	radiation shape factor
$g(\beta)$	constriction alleviation factor defined in Eq. 29
$G(r_i; r_j)$	cylindrical function defined in Eq. 9
$h$	contact conductance, $\text{BTU/hr-ft}^2\text{-}^\circ\text{F}$
$H_I$	interfacial heat transport modulus
$I, J$	finite element generalized indicies
$I_0, K_0$	zero order modified Bessel functions of the first and second kind, respectively
$J_0, Y_0$	zero order Bessel functions of the first and second kind, respectively
$k$	thermal conductivity, $\text{BTU-in./hr-ft}^2\text{-}^\circ\text{F}$
$\ell$	finite element unit dimension, in.
$L$	specimen column length, in.
$n$	eigenvalue index
$q$	heat flux, $\text{BTU/hr-ft}^2$
$Q$	heat flow, $\text{BTU/hr}$
$r$	radial coordinate, in.
$R$	thermal contact resistance, $\text{hr-}^\circ\text{F/BTU}$
$T$	temperature, $^\circ\text{F}$
$u(\chi'_n; r_i; r_j)$	cylindrical function defined in Equation 13

## NOMENCLATURE (Contd)

$V$	sonic velocity, ft/sec
$X, Y$	finite element cartesian coordinate
$z$	axial coordinate
$\alpha$	dimensionless axial distance
$\beta$	ratio of contact element radius to contact area radius
$\delta$	effective gap width, in.
$\epsilon$	total hemispherical emittance
$\zeta$	resistance product defined in Eq. 32, $(\text{hr}-^\circ\text{F}/\text{hr})^2$
$\eta$	constant defined in Equation 22
$\theta$	angular coordinate, radians
$\kappa$	eigenvalue parameter
$\lambda$	eigenvalue parameter
$\mu$	accommodation coefficient
$\nu$	integration variable
$\xi$	constant defined in Equation 22
$\rho$	density, $\text{lbs}/\text{ft}^3$
$\sigma$	Stefan-Boltzman constant, $\text{BTU}/\text{hr}-^\circ\text{F}^4$
$\phi$	mean free path, in.
$\psi$	stream function
$\omega$	resistance product defined in Eq. 32, $\text{hr}-^\circ\text{F}/\text{hr})^2$

NOMENCLATURE (Contd)

Subscripts

c	contact
i	insulation
l	lattice
m	mean
n	eigenvalue index
N	normal
R	radiation
s	specimen, solid
T	total
$\lambda$	spectral

## SECTION I

### INTRODUCTION

When two surfaces are brought together to form an interface the true solid-to-solid contact area between them is generally a small fraction of the apparent area over which they meet. This direct contact area may be less than 1% of the total and rarely exceeds about 10% unless bonding agents are introduced. It is intuitive that when an interface is encountered in a heat flow field there will be a resistance to heat transfer across it. As a result a temperature discontinuity will appear across the contact; this temperature drop divided by the heat flux flowing across the interface is termed the thermal contact resistance.

Early work in the contact resistance field was centered on the study of electrical energy flow in various types of electrical motor and switch applications. More recently a great amount of activity has been underway in studying the flow of heat from metal-clad nuclear fuel elements. Contact resistance is very important here because of the large heat fluxes crossing the fuel element-cladding interface. Other current applications where interfacial heat transfer is important include high temperature aircraft structural design, dissipation of heat from space vehicle systems, heat exchanger design, and the design of turbine powered engines and solid and liquid fueled rockets. Recent Soviet activity in the area has emphasized these latter applications.

An example of the practical importance of joint thermal conductance in aerospace structural component performance is illustrated in the work of Griffith, et al. (Reference 1) who studied the structural response of skin-stiffener panels heated on their external surfaces. These constructions are typical of aircraft and space vehicle structural units. The presence of joints greatly altered temperature distributions and increased thermal stresses in the panels. In a Mach 2 jet tunnel test of a wing section it was observed that flutter and dynamic failure resulted from poor thermal contact in the joint.

In higher temperature aerospace applications such as rocket nozzles and high performance reentry vehicles, many of the materials used are oxidation resistant nonmetallic refractories. In these systems interfaces are often encountered which may consist of metallic/nonmetallic or nonmetallic/nonmetallic components. During system operation it is generally found that heat is transferred across these interfaces at high temperature levels. A knowledge of thermal contact resistance ranges for such high temperature interfaces is clearly necessary. This is particularly true for the case of nonmetallic interfaces where the materials

are of a brittle nature. Accurate thermal stress analysis is vital in design with brittle materials and it is only with accurate estimates of the temperature fields in complex structures that these thermal stress calculations can be made. Examples of specific engineering applications in this area include the study of interface contact coefficients in the Minuteman solid rocket nozzle (Reference 2) and the contemplated use of nonmetallic thermal contact resistance barriers as a form of insulative liner for high pressure thrust chambers.

In a typical solid rocket the upper stages utilize a flame barrier backed up by a heat sink of graphite. In connection with this application Gilchrist (Reference 1a) studied heat transfer across contacts consisting of graphite, tungsten, and molybdenum, including various combinations of these materials. Interface temperatures from 1000 to 2000°F were studied in this investigation, together with high temperature bonding and brazing schemes. In general, the results indicated that interfacial temperature drops from about 100 to 1000°F were likely at the heat flux levels encountered in such high performance rocket systems. The possible thermal stress and reliability uncertainties can become considerable in such instances.

The author has prepared Reference 1 with the objective of reviewing and summarizing the literature in the thermal contact resistance field with particular attention to high temperature results and data on nonmetallic interfaces. The volume also reviews in some detail the available analytical approaches used for both single and multiple contact interfaces and the more successful experimental-analytical correlations. The correlations developed as well as the literature results which were of direct value will be introduced and discussed in later portions of this report.

Several general observations relevant to high temperature applications can be made as a result of the literature review (which has been continually updated to the time of this writing):

- a. The overwhelming majority of thermal contact resistance studies have been concerned with metallic/metallic interfaces.
- b. The independent variable most often employed is the compressive load on the interface.
- c. In those few cases where contact resistance is measured as a function of temperature, the maximum temperature ranges between 500-700°F.

Based on the practical importance of contact resistance data for high temperature aerospace applications and the paucity of such information as reflected in the above observations, a program was initiated to study the contact resistance characteristics of non-metallic interfaces extending to elevated temperatures. To the best of the author's knowledge no previous systematic study of heat transfer across nonmetallic interfaces has been made nor have there been any previous investigations conducted in the range though necessary to account for significant radiative contributions to the overall interfacial heat transfer.

The selection of the nonmetallic materials for study was based primarily on their aerospace importance and on experimental requirements for high accuracy contact resistance measurements. The oxide ceramics were selected initially for consideration because of their broad technological usage. From an experimental point of view, it was found that the level of thermal conductivity was one of the most important parameters, high conductivity being desirable for highest measurement accuracy. This criteria lead immediately to the selection of beryllium oxide which has the highest conductivity of the oxide ceramics.

The material has the additional attribute of being reproducibly available as high purity stock from commercial vendors; its intrinsic toxicity is minimal in sintered form and, with reasonable precautions in handling, presents no problems. Further, the temperature dependence of the thermal conductivity obeys the classical hyperbolic functionality expected theoretically for pure phonon conducting dielectrics. Because the beryllium oxide specimens were utilized as heat meters in the thermal contact resistance measurements, a precise knowledge of the conductivity was necessary.

The major variables in the thermal contact resistance measurement program on the beryllium oxide interfaces were: (1) the surface finish, (2) the mean interfacial temperature, and (3) the compressive load.

Section II describes the equipment constructed for this investigation and summarizes the results of the experimental checkout of the equipment, which included thermal conductivity measurements on beryllium oxide and tantalum. Comparison of these results with literature values were made in assessing equipment performance. Analytical equations were also developed in this section for predicting heat losses in the equipment; full derivations of these equations are given in Appendix I. The predicted heat losses were then compared with experimentally measured values as a further evaluation of apparatus performance.

The next major section of the report (Section III) presents the experimental thermal contact resistance results along with important surface characterization information.

Following this is the discussion of the results, Section IV, which includes the development of two analytical procedures for the prediction of thermal contact resistance. Again, the details of the analytical derivations were relegated to an appendix. Detailed comparison was made between these predicted contact resistance curves and the experimentally obtained results.

Section V covers conclusions and recommendations.



## SECTION II

## APPARATUS CONSTRUCTION AND QUALIFICATION TESTING

## A. EQUIPMENT DEVELOPMENT

One of the most important problems encountered in conducting experimental contact resistance measurements is controlling the waviness of the test interface. As amply demonstrated in the literature (Reference 1), inconsistencies and nonreproducibility of results can very often be traced to this factor, particularly at low compressive load levels. In addition to careful surface preparation, one of the simplest methods of minimizing this problem is to work with interfaces of minimum cross-sectional area. Another important consideration for thermal contact resistance measurements is the development of a uniform heat flux field on both sides of the interface to facilitate heat flux and temperature measurements. Meeting these two requirements leads to specimen configurations with length to diameter ratios greater than unity. Thus, in well designed contact resistance experiments, cylindrical specimens with length to diameter ratios from 1.5 to 3.0 are widely used.

For such geometries, axial heat flow is highly advantageous as long as the level of specimen thermal conductivity is fairly high. "High" in this sense implies relative to the conductivity of the insulation used along the lateral surfaces of the specimens to prevent radial heat losses. The equipment employed in this investigation is a modification of the "cut bar" design used widely in thermal conductivity measurements on high conductivity materials with cylindrical specimen configurations.

The basic design, shown schematically in Figure 1, is quite simple. A composite bar of circular cross section is built up of several specimens by stacking one upon another. One end of the column is heated, the other cooled to produce a steady axial heat flux down through the composite bar. The column is insulated laterally, and guard heaters are employed to reduce radial heat flow. The series of guard heaters are used to match the axial temperature distribution at the external surface of the insulation to that down through the specimens. If the radial heat losses are small then at steady state the ratio of  $(\partial T / \partial z)$  in each specimen is directly equal to the ratio of the respective thermal conductivities. In comparative conductivity determinations, heat meters with known conductivities are placed above and below the specimen on which thermal conductivity is to be determined (Figure 1). A nominal compressive load (10 to 100 psi) is generally applied to reduce the contact resistance between specimens.

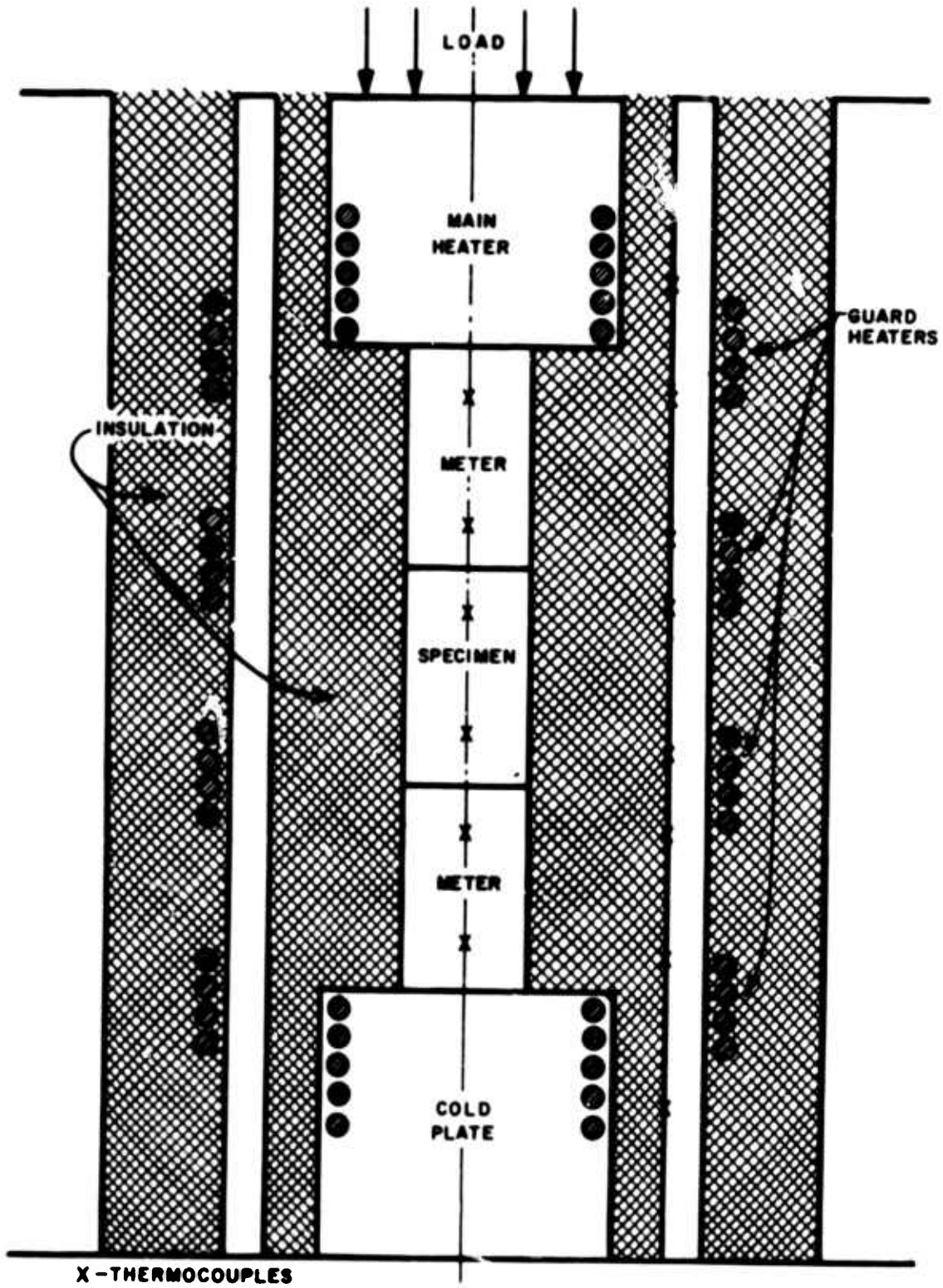


Figure 1. Schematic of Cut-Bar Comparative Conductance Apparatus

For contact resistance measurements, two specimens of known conductivity are brought together to form the interface. The temperature gradient in the specimens away from the interface and the known thermal conductivity are sufficient to determine the heat flux crossing the interface. It is obvious that the relative magnitude of lateral heat losses will be small if the specimen conductivity is high. The interfacial temperature drop generated at the mutual contact between the specimens is determined by extrapolating the steady state temperature gradients in the specimens to the contact plane. The thermal contact resistance is then defined as the ratio of this interfacial temperature drop to the steady state axial heat flux in the column. Provision is made for application of a variable dead weight compressive load along the axis of the specimens.

The particular design used in this investigation has several distinctive features which will be brought out in discussing the apparatus cross section shown in Figure 2. Overall, the apparatus has been designed for high temperature operation. The specimens (1-inch diam. x 2-inch long cylinders) for either thermal conductivity or thermal contact resistance measurements are centered on a water-cooled copper pedestal. The pedestal is machined internally with channels both in the upper face and in the neck such that water circulates upward from the bottom of the pedestal, reverses its path, and returns downward. With this arrangement no water connections are required within the vacuum chamber which surrounds the entire unit and which rests on the base plate.

The specimens are insulated laterally with low conductivity alumina bubble insulation which is contained within the tantalum cylinder. The tantalum cylinder has a flange near its upper extremity which supports the guard heater. The lower end of this cylinder is supported and cooled by the copper pedestal. The stainless steel and tantalum radiation shields for the guard heater rest on a ring of transite insulation. This ring is supported from the base plate by an Inconel 702 support stand. The upper portion of the Inconel stand is polished, thus serving as an additional radiation shield.

The main heater core is supported by an alumina disk which in turn rests on the alumina bubble insulation. This disk also serves to support the five tantalum radiation shields for the main heater. Because of the high operating temperature of the heaters it was calculated that radiation shields would be more efficient thermally than other forms of insulation.

A dead weight compressive load is transferred to the specimen column through a tantalum plug which absorbs heat from the main heaters but floats independent of it. The stainless

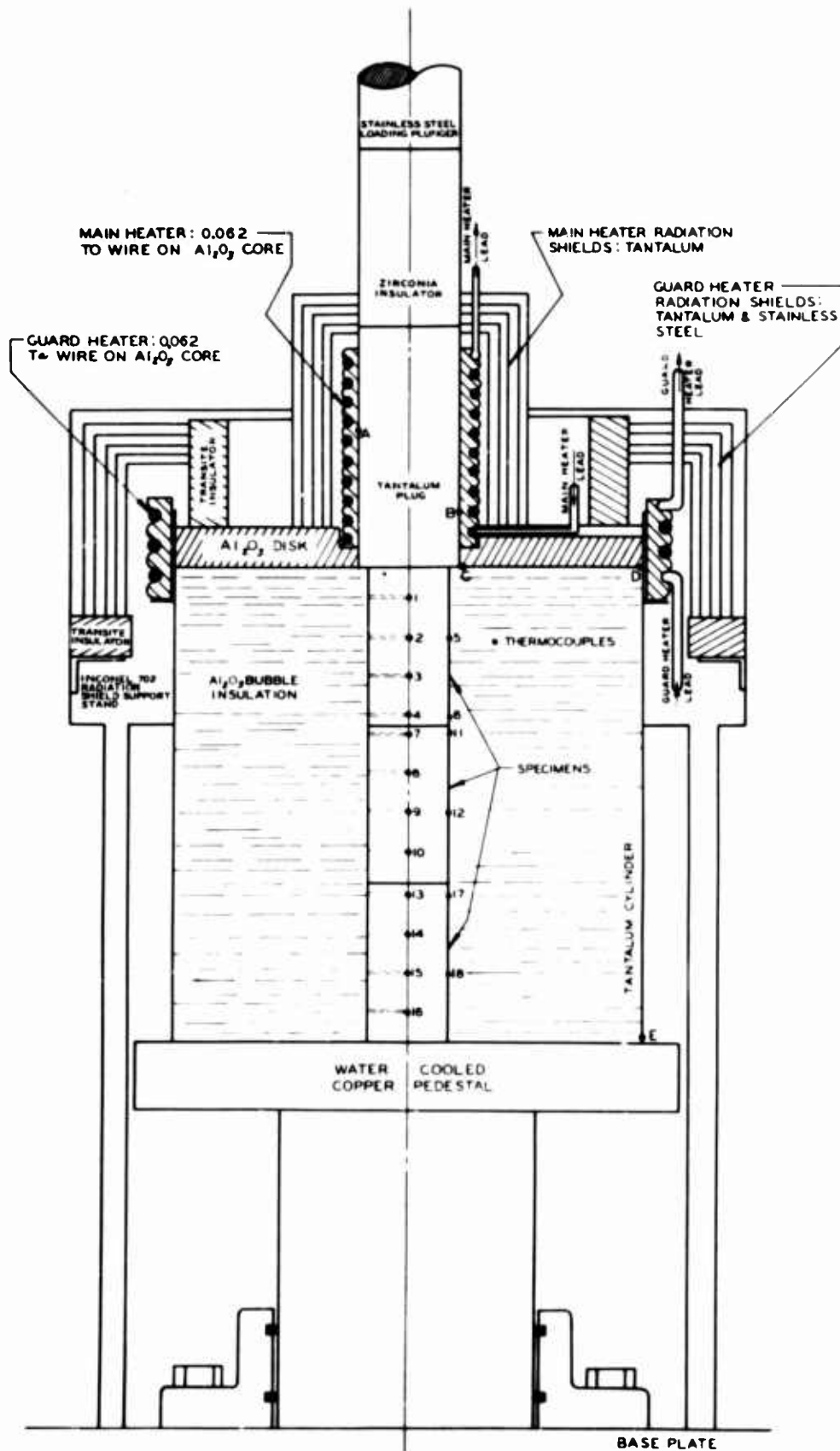


Figure 2. Contact Resistance Apparatus Cross-Section

steel load plunger is thermally insulated from the tantalum plug by a section of high compressive strength low thermal conductivity zirconia (calcia stabilized).

Instrumentation with platinum/platinum-10% rhodium thermocouples is shown in Figure 2. In this particular setup the three specimens have thermocouples attached to their surfaces. The leads of these surface couples are electrically insulated from the specimen and wrapped circumferentially about one-half turn along an isothermal plane to minimize heat leaks down the leads. Additional thermocouples are placed in radial holes drilled to the centerline of each specimen. These couples are placed in two-bore ceramic tubing which extends radially from the centerline out beyond the surface of the specimen into an isothermal plane; again, this is to prevent heat leak down the leads of the couples. High temperature "Astrocera" cement (from American Thermocatalytic Corp., Mineola, New York) was used to anchor the various couples.

During operation, the main heater power is set to provide the desired temperature distribution in the specimen column. The guard heater is adjusted so that the temperature difference between thermocouples "C" and "D" (Figure 2) is zero. In some instances these couples were connected differentially to allow automatic control of the guard heater.

Figure 3 gives a closeup photograph of the assembled apparatus. In Figure 4 is presented an overall view of the equipment. The water-cooled vacuum chamber is lowered onto the base plate during vacuum or inert environment testing. The four upright posts seen in Figure 4 support the compressive loading assembly. This loading assembly and the vacuum chamber are shown in place in Figure 5.

The fulcrum of the compression unit is mounted in a heavy gage ball bearing block. The counterweights, the compressive load and the main lever arm are all loaded on knife edges. The lever arm has a 16 to 1 mechanical advantage. The exact dimensions of the lever arm makes it simple to calculate the compressive load established by the plunger as a function of the weight on the load pan. Experimentally this was checked with the aid of a proving ring to a load level of 5200 psi. Counterweights were first added to balance the arm at zero compressive load; following this, the actual load was measured as a function of pan weight.

A deviation plot of the results was prepared by taking the percentage difference between calculated and measured values at various compressive load levels and then plotting these values as a function of load level. Deviation from theory was within 2%, while the deviation



Figure 3. Assembled Components

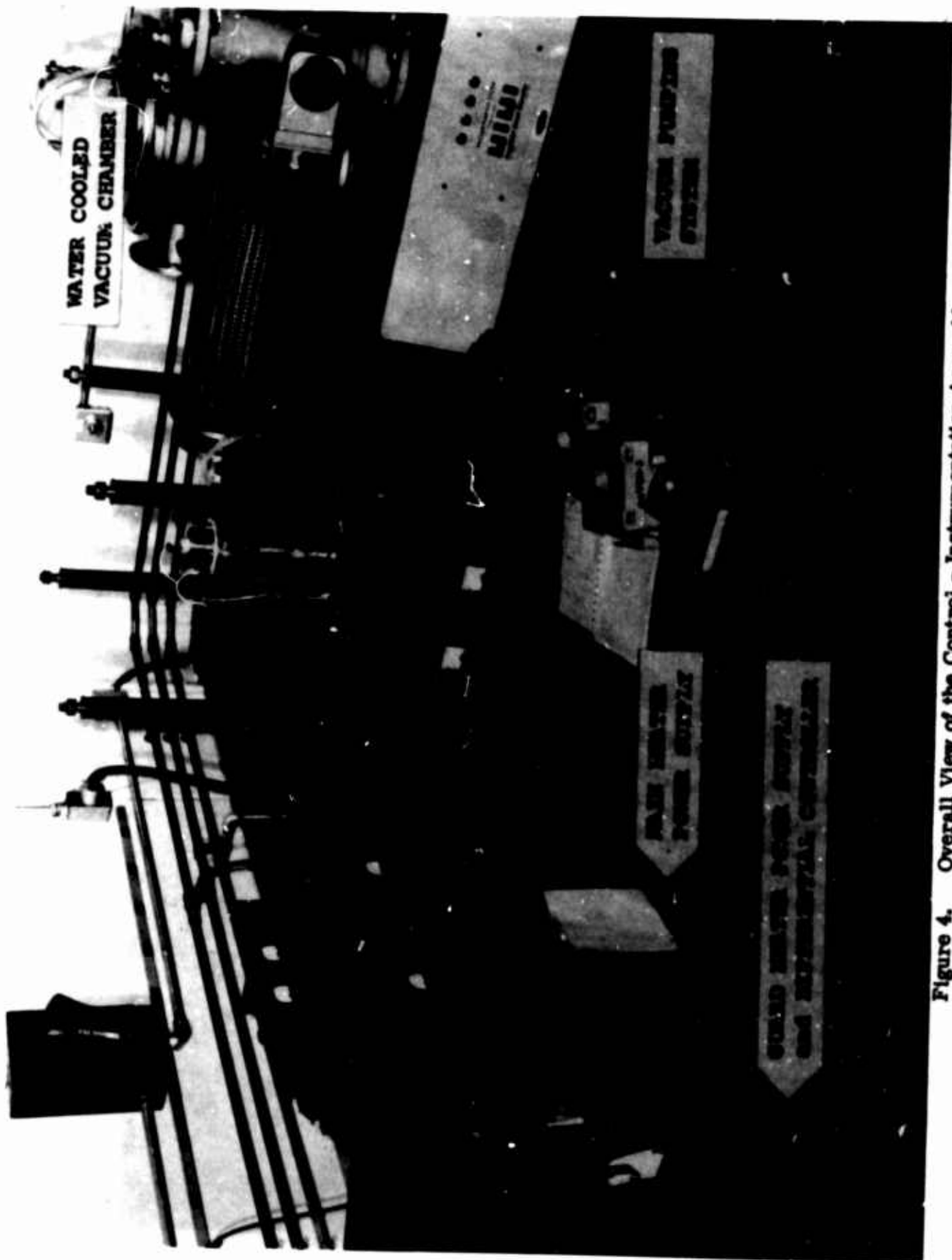


Figure 4. Overall View of the Control - Instrumentation Assembly



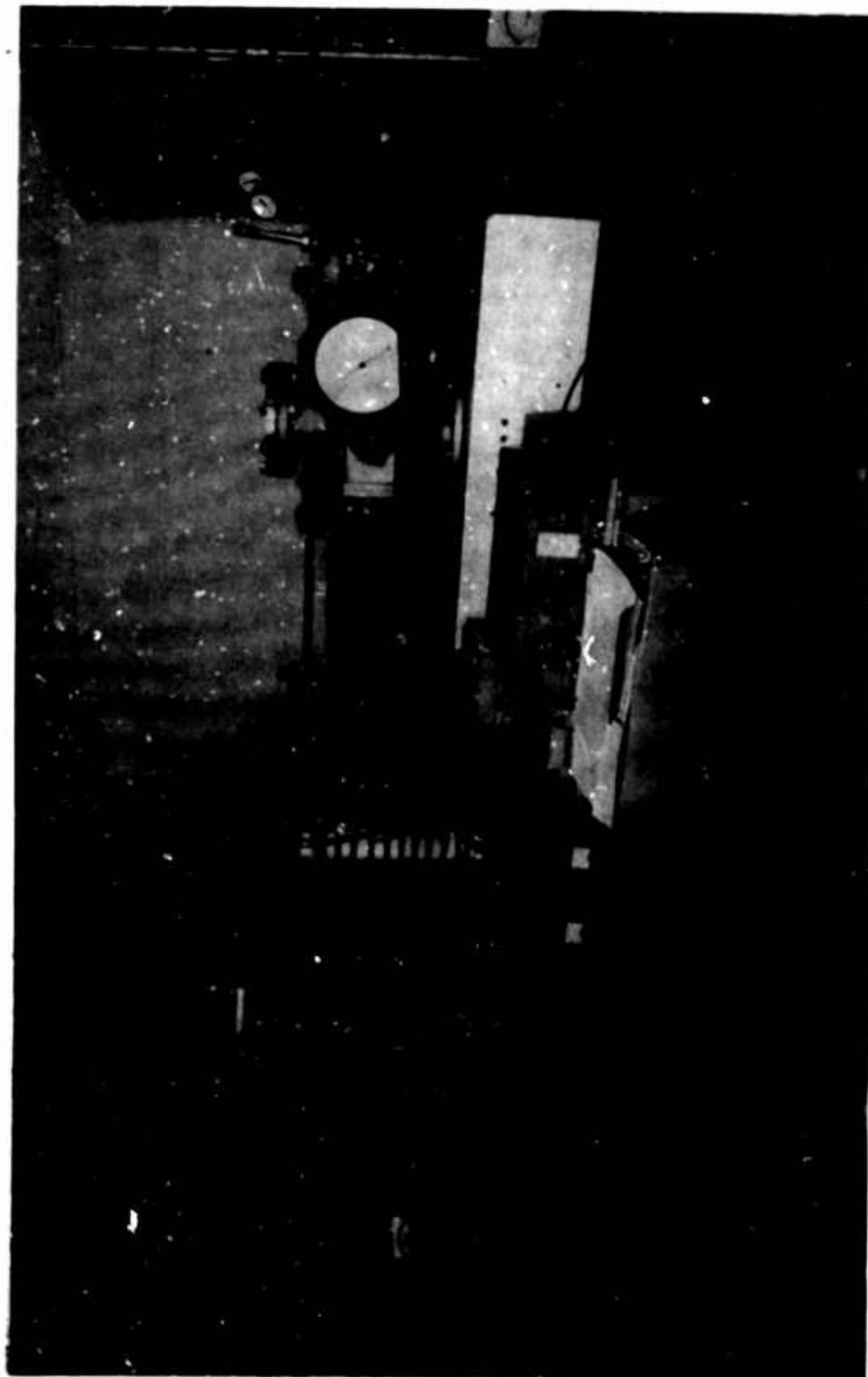


Figure 5. Assembled Test Cell Including Load Column



from an average curve through the data was within about 1%. At load levels of 1450 psi and 4200 psi, runs were made in which increases and then decreases in load about these values were used to assess the effect of friction within the assembly. Data points for increasing and decreasing loads at these two levels were within 1%, and thus frictional effects appear to be quite small.

## B. DESIGN CONSIDERATIONS

### 1. Design Philosophy

The Equipment layout just described assists in the following discussion of the rationale which led to this configuration.

With any given temperature distribution in the test section of the apparatus, that is, the gradient along the composite bar made up of the specimens and the temperature variation down the tantalum cylinder supporting the guard heater, any lateral heat flow to or from the specimens is proportional to the thermal conductivity of the insulation,  $k_i$ . If  $\bar{k}_s$  is an average conductivity of the specimen composite bar, then the importance of such spurious heat flows in apparatus performance diminishes as the ratio  $k_i / \bar{k}_s$  decreases.

For the alumina bubble insulation-beryllium oxide combination, studied here, this ratio varied from about 0.0008 at room temperature to about 0.02 at 2000° F. Simple heat transfer analysis of the system showed that heat losses were very small (on the order of 1 to 2% at most) even for cases where there was very poor matching between the temperature gradients down the specimen cylinder and the tantalum guard cylinder.

This situation was verified experimentally as discussed in some detail below in connection with the beryllium oxide and tantalum thermal conductivity measurements, and was also verified analytically with an exact Fourier analysis of the system as discussed under "Heat Losses." Thus, the use of the guard heater was mainly to provide a nearly isothermal zone for specimen thermocouple leads extending out into the insulation and to prevent excessive power dissipation from the main heater, and only secondarily to control radial heat losses from the specimen column. Of course, if the ratio  $k_i / \bar{k}_s$  were significantly larger (e.g., near unity) the above comments would not be valid.

### 2. Instrumentation

In most studies where conductivity measurements are run with cylindrical specimens, the thermocouples are mounted on the specimen surface. However, in the case of thermal

contact resistance tests, it was found from the literature that most investigators mounted the couples in radial holes drilled to the specimen centerline. In the brief analysis which follows the variables determining the best radial location of the thermocouples are discussed for the particular system used here.

The first limiting case considered is where the thermocouples are located in radial holes, the thermal conductivity of the thermocouple sensor  $k_{T.C.}$  being much less than that of the specimen,  $k_s$ . This is represented by the situation where a couple in an insulated ceramic tube is used in measurements with metals or high conductivity nonmetals. The extent to which the couple perturbs the heat flow in the specimen can be readily established using equations analogous to those developed for the fluid dynamics problem of incompressible, irrotational flow.

If a stream function  $\psi$  is defined, then the lines of constant heat flux are represented geometrically by families of curves where  $\psi = \text{constant}$ . In the case of steady-state two-dimensional heat transfer the Laplace equation in cylindrical coordinates can be written as

$$\frac{\partial^2 \psi}{\partial r^2} + \frac{1}{r} \frac{\partial \psi}{\partial r} + \frac{1}{r^2} \frac{\partial^2 \psi}{\partial \theta^2} = 0 \quad (1)$$

The solution of this equation for heat flow around a nonconducting cylinder of radius  $a$  in an isotropic media is

$$\psi = q_\infty \sin \theta \left( \frac{a^2}{r} - r \right) \quad (2)$$

The important boundary condition which permits use of this analytical approach for the heat transfer case is the condition that the  $\psi = 0$  streamline conforms to the surface of the perturbing cylinder. A plot of this function is given in Figure 6.

The extent of the perturbation in the direction  $\theta = 90^\circ$  is given by the rate of change of  $\psi$  with respect to  $r$ . The perturbation is zero when this quantity,  $\left[ \partial \psi / \partial r \right]_{\theta = 90^\circ}$ , becomes constant. From Equation 2

$$\left| \frac{\partial \psi}{\partial r} \right|_{\theta = 90^\circ} = q_\infty a^2 \left( 1 + \frac{1}{r^2} \right) \quad (3)$$

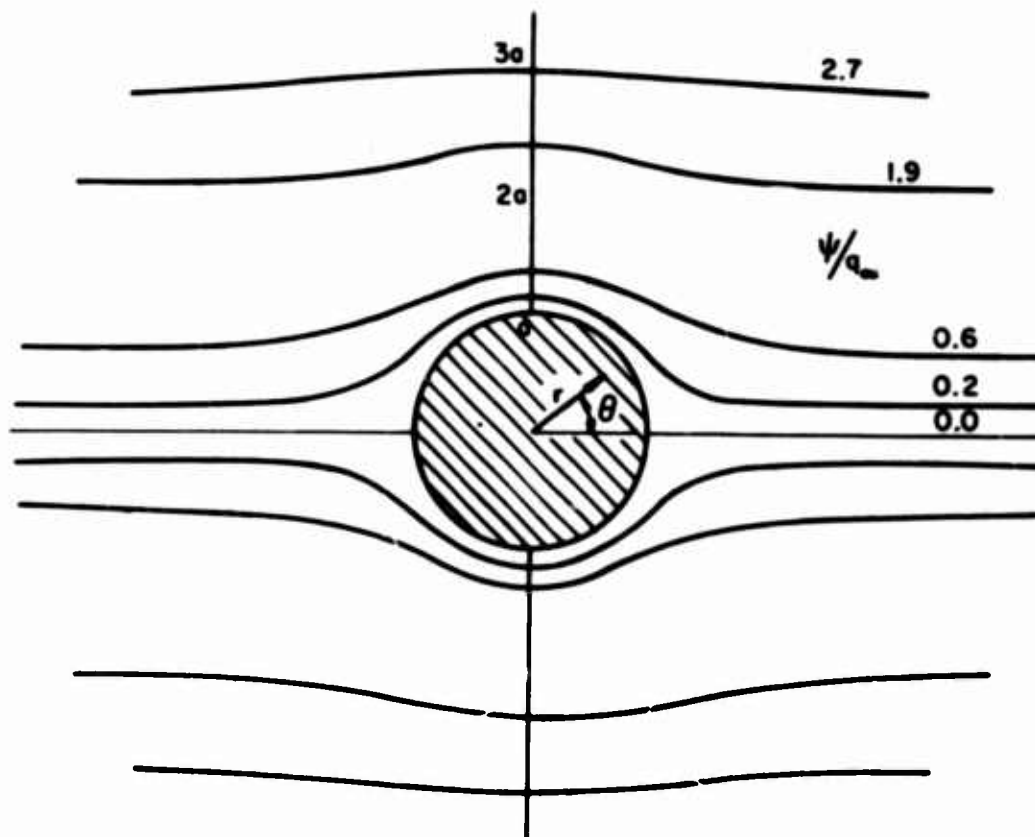


Figure 6. Perturbation of Heat Flow From a Nonconducting Cylinder in an Isotropic Media

Thus, the perturbation diminishes rapidly with radial distance, and is approximately 10% at a distance of  $r = 3a$  (one diameter away from the surface  $r = a$ ). As the conductivity of the specimen approaches that of the cylinder, the perturbation at a given radial distance decreases. The approximate variation as a function of specimen conductivity is indicated as the "Internal" curve in Figure 7.

Now considering the alternate case of surface mounting of the thermocouples, major errors could be encountered in the temperature measurement if radial heat losses become significant. These losses are proportional to  $k_i (\partial T / \partial r)$ . If the overall temperature drop down the composite bar made up of meters and specimens is assumed to be constant then the radial heat loss will be approximately constant for a given insulation. On the other hand, if this same overall drop is maintained from test to test, the specimen heat flux will be proportional to the mean conductivity of the composite bar,  $\bar{k}_g$ . The percentage heat loss, which is a direct indication of possible specimen temperature measurement errors for surface mounted thermocouples, is then given by the following equation

$$\frac{q_{\text{loss}}}{q_{\text{specimen}}} = D(r, z) \frac{k_i \frac{\partial T}{\partial r}}{\bar{k}_g \frac{\partial T}{\partial z}} \quad (4)$$

Thus, for a given system the temperature measurement error is approximately proportional to  $(1/\bar{k}_g)$ . In Equation 4 conditions typical of those used in this investigation were used to generate the "Surface" curve shown in Figure 7.

It is clearly shown that the optimum location of the thermocouple sensor for minimum error in the temperature measurement varies as a function of the conductivity of the specimen. Because the thermal conductivity of the beryllium oxide decreases rapidly with temperature it was concluded, based on the curves shown in Figure 7, that both surface and internal thermocouples should be used in studying the performance of this apparatus. For the particular experimental arrangement used in this investigation the curves are quantitative. For other systems the curves indicate qualitatively that as the thermal conductivity of the specimens under test become lower, it may be more desirable to mount the measurement thermocouple internally.

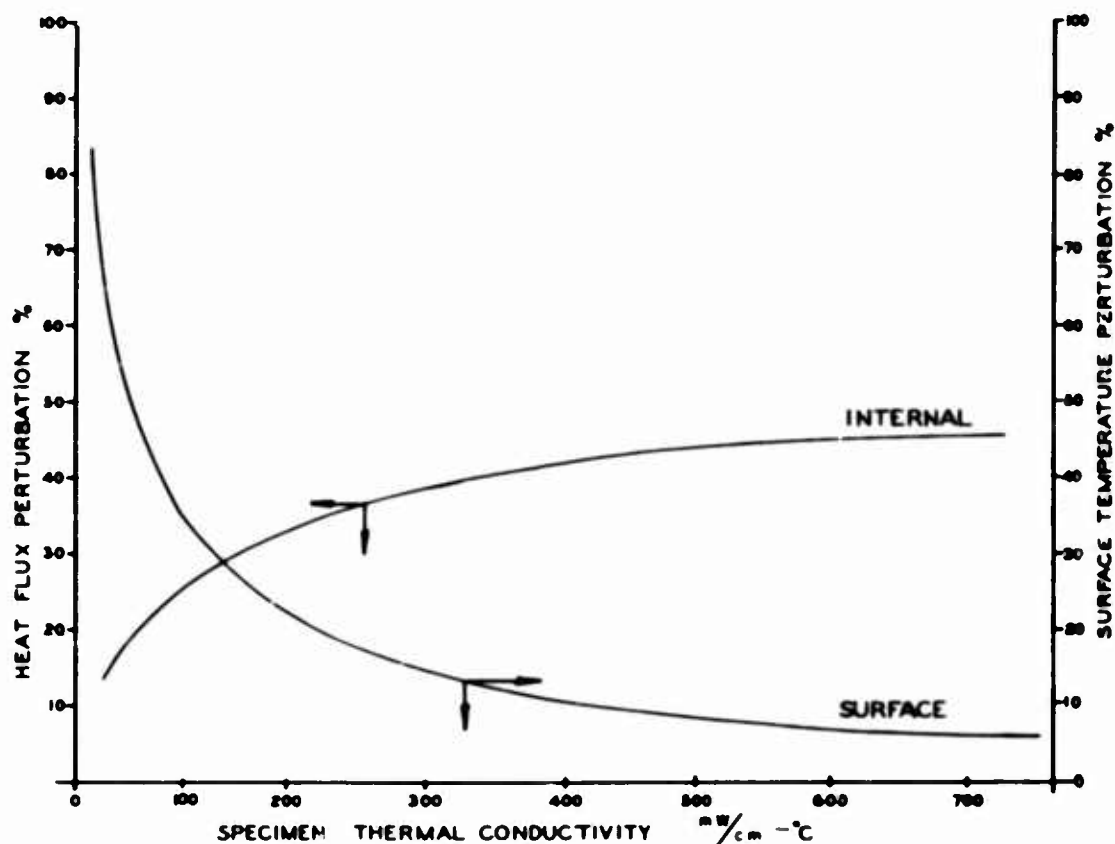


Figure 7. Temperature Field Perturbation as a Function of Specimen Conductivity

### 3. Heat Loss Analysis

In order to arrive at an analytically exact prediction of the heat exchange between the specimen column and the insulation surrounding it, it is necessary to have an expression for the radial temperature gradient variation down the column surface. If this is available then an equation of the following form can be applied,

$$q_{\text{loss}} = 2 \pi r_0 k_i \int_0^L \left( \frac{\partial T}{\partial r} \right)_{r=r_0} dz \quad (5)$$

The expression for  $(\partial T / \partial r)_{r=r_0}$  was obtained by developing a general equation for the temperature field in the annular insulation region surrounding the specimens and performing the indicated differentiation. This temperature field equation was constructed by superposition of solutions for the steady-state boundary value system made up of the insulation region with its surface temperature distributions. The most general solution developed for

this axisymmetric system was for arbitrary temperature distributions  $f_0(z)$ ,  $f_1(z)$ ,  $f_2(r)$  along the inner and outer cylindrical boundaries and the upper surface boundary respectively. The lower surface boundary was assumed to be at a constant temperature,  $T = 0$ , although this is essentially a temperature field normalization condition which could very easily be relaxed. A sketch of the system and these boundary conditions is given in Figure 8.

A complete derivation of the insulation temperature field equation  $T_{\text{insul}} = f(r, z)$  as well as the equation for  $q_{\text{loss}}$  is included in Appendix I. The discussion below summarizes the important aspects of the derivation.

Because the governing differential equation,  $\nabla^2 T = 0$ , is linear (i.e.,  $k_i \neq f(T, r, z)$ ), the various boundary conditions were considered separately, the solution for each then added to give the required result. A solution was developed for boundary conditions 1 and 2 simultaneously, and then a solution for boundary condition 4.

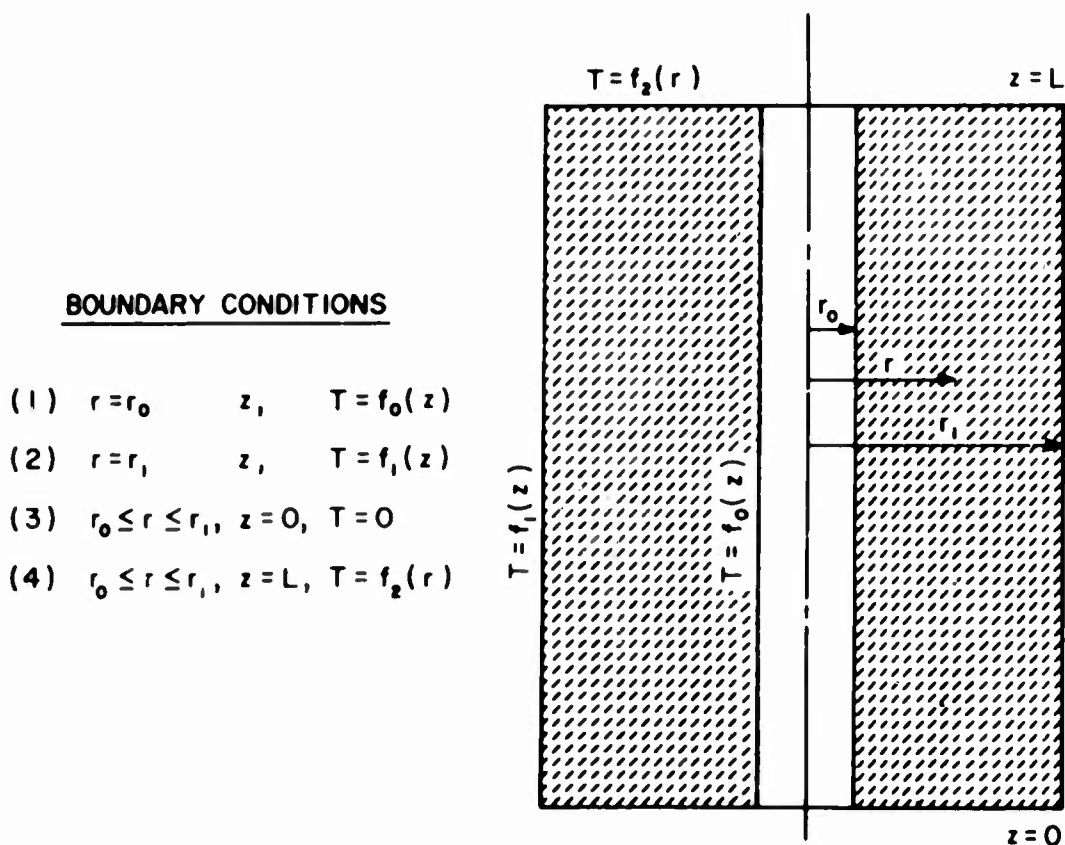


Figure 8. Insulation Segment and Boundary Conditions

The solution of Laplace's equation in cylindrical coordinates for the axisymmetric case is performed by separation of variables with integration of the resulting total differential equations. For the case when the boundary conditions (B. C. ) are a function of the axial coordinate (B. C. 1 and 2) the general product solution is in terms of  $\sin(z)$  and modified zero order Bessel functions of the first and second kind,  $I_0(r)$  and  $K_0(r)$ . When the boundary conditions are a function of the radial coordinate (B. C. 4) the general product solution is in terms of the hyperbolic function  $\sinh(z)$  and zero order Bessel functions of the first and second kind,  $J_0(r)$  and  $Y_0(r)$ .

Considering first the analysis involving boundary conditions 1 and 2, separation of variables leads to the following general solution of Laplace's equation,

$$T(r, z) = [A' I_0(\lambda r) + B' K_0(\lambda r)] [C' \cos(\lambda z) + D' \sin(\lambda z)] \quad (6)$$

where,

$$A', B', C', D' = \text{constants}$$

The  $T = 0$  boundary condition along the surface  $z = 0$  leads to the requirement that

$$C' = 0$$

The  $T = 0$  boundary condition along the surface  $z = L$  lead to the following eigenvalue restrictions on the parameter  $\lambda$ .

$$\lambda L = n\pi, \quad n = 0, 1, 2, \dots$$

Thus, a particular solution of the differential equation becomes,

$$T(r, z) = \left[ E'_n I_0\left(\frac{n\pi r}{L}\right) + F'_n K_0\left(\frac{n\pi r}{L}\right) \right] \sin\left(\frac{n\pi z}{L}\right) \quad (7)$$

The constants in this equation are now subscripted as  $E'_n$  and  $F'_n$  since there is a solution for each value of  $n$ .

To satisfy boundary conditions 1 and 2 it is necessary to utilize an infinite series solution of the differential equation constructed as a linear combination of solutions of the form given in Equation 7. Then

$$T(r, z) = \sum_{n=1}^{\infty} T(r, z)_n \quad (8)$$

This linear combination is also a solution of the original differential equation. After a regrouping of the constants in cylindrical function form the infinite series solution can be written

$$T(r, z) = \sum \frac{\rho \left( \frac{n\pi r_1}{L} \right) G_n(r; r_0) + \rho \left( \frac{n\pi r_0}{L} \right) G_n(r_1; r)}{G(r_1; r_2)} \sin \left( \frac{n\pi z}{L} \right) \quad (9)$$

where

$$\rho \left( \frac{n\pi r_0}{L} \right) = E'_n I_0 \left( \frac{n\pi r_0}{L} \right) + F'_n K_0 \left( \frac{n\pi r_0}{L} \right)$$

$$G_n(r_1; r_0) \equiv I_0 \left( \frac{n\pi r_1}{L} \right) K_0 \left( \frac{n\pi r_0}{L} \right) - I_0 \left( \frac{n\pi r_0}{L} \right) K_0 \left( \frac{n\pi r_1}{L} \right)$$

Substituting B.C. 1 and 2 in the above equation and developing the Fourier coefficient integral conditions in the usual way for this orthogonal family (Reference 2) leads to the following general solution of the differential equation meeting boundary conditions 1 and 2.

$$T(r, z) = \frac{2}{L} \sum_{n=1}^{\infty} \frac{\sin \left( \frac{n\pi z}{L} \right)}{G_n(r_1; r_0)} \left\{ G_n(r; r_0) \int_0^L f_1(z) \sin \left( \frac{n\pi z}{L} \right) dz \right. \\ \left. + G_n(r_1; r) \int_0^L f_0(z) \sin \left( \frac{n\pi z}{L} \right) dz \right\} \quad (10)$$

Considering now the solution involving boundary condition 4, separation of variables leads to the following general solution of Laplace's equation:

$$T(r, z) = \left[ A J_0(Kr) + B Y_0(Kr) \right] \left[ C \cosh(Kz) + D \sinh(Kz) \right] \quad (11)$$

where

A, B, C, D = constants

The  $T = 0$  boundary condition along the surface  $z = 0$  leads to the requirement that

$$C = 0$$

Applying the boundary conditions

$$r = r_0, \quad z, \quad T = 0$$

$$r = r_1, \quad z, \quad T = 0$$



and eliminating the constants A and B from the resultant equations leads to the following condition which must be fulfilled:

$$Y_0(K r_0) J_0(K r_1) - Y_0(K r_1) J_0(K r_0) = 0 \quad (12)$$

The above condition is met by an infinite number of eigenvalues,  $K_n$ , which are the positive roots of this equation. Introducing cylindrical function notation,

$$u_0(K_n; r_0; r_1) \equiv J_0(K_n r_0) Y_0(K_n r_1) - J_0(K_n r_1) Y_0(K_n r_0) \quad (13)$$

We can now define the eigenvalues,  $K_n$ , by

$$u_0(K_n; r_0; r_1) = 0, \quad n = 1, 2, 3, \dots \quad (14)$$

Thus, a particular solution of the differential equation becomes

$$T(r, z) = [A_n J_0(K_n r) + B_n Y_0(K_n r)] [D_n \sinh(K_n z)] \quad (15)$$

where again the constants are subscripted to reflect the family of solutions represented by the eigenvalues,  $K_n$ .

Writing the corresponding infinite series solution and recasting the form of the constants leads to the following representation for  $T(r, z)$ ,

$$T(r, L) = f_2(r) = \sum_{n=1}^{\infty} \frac{Q(K_n r_1) [u_0(K_n; r_0; r)] + Q(K_n r_0) [u_0(K_n; r_1; r)]}{u_0(K_n; r_0; r_1)} \sinh(K_n L) \quad (16)$$

where

$$Q(K_n r) \equiv E_n J_0(K_n r) + F_n Y_0(K_n r)$$

Substituting B.C. 4. in the above equation and developing the Fourier coefficient integral conditions leads to the general solution given below in Equation 17 as a cylindrical function Fourier series. The norm  $N\{u_0(r)\}$  for this class of orthogonal functions is found by applying Lommel integral relations.

$$T(r, z) = \frac{\pi^2}{2} \sum_{n=1}^{\infty} \frac{K_n^2 J_0^2(K_n r_0) u_0(K_n; r; r_1) \sinh K_n z}{[J_0^2(K_n r_0) - J_0^2(K_n r_1)] \sinh K_n L} \int_{r_0}^{r_1} r f_2(r) u_0(K_n; r; r_1) dr \quad (17)$$

The general solution of the original differential equation meeting all the boundary conditions given in Figure 8 is simply the sum of Equations 10 and 17.

For this particular experimental arrangement, boundary condition 4 is not arbitrary. The constraint on  $f_2(r)$  is of a physical nature rather than mathematical. If  $f_1(L)$  and  $f_0(L)$  are the temperatures on the  $z = L$  plane at points  $r = r_1$  and  $r = r_0$ , respectively, then, as developed in Appendix I, to satisfy  $\nabla^2 T = 0$ ,

$$T = f_0(L) + \{f_1(L) - f_0(L)\} \left[ \frac{\ln \frac{r}{r_0}}{\ln \frac{r_1}{r_0}} \right] \quad (18)$$

It will be shown later that  $f_0(z)$  and  $f_1(z)$  can be quite accurately represented in the form,

$$f_0(z) = T_0(1-\alpha) + \alpha T_{L_0} \quad (19)$$

$$f_1(z) = T_1(1-\alpha) + \alpha T_{L_1} \quad (20)$$

where

$$\alpha = \frac{z}{L}$$

$$T_0 = f_0(0), T_{L_0} \equiv f_0(L)$$

$$T_{L_1} \equiv f_1(L)$$

Using Equations 18 - 20 for explicit evaluation of the various Fourier coefficient integrals leads to the following equation for the temperature distribution in the insulation segment:

$$\begin{aligned} T(r, z) = & \frac{\pi}{\ln\left(\frac{r_1}{r_0}\right)} \sum_{n=1}^{\infty} \left[ \frac{J_0(K_n r_0) u_0(K_n; r; r_0) \sinh(K_n z)}{[J_0^2(K_n r_0) - J_0^2(K_n r_1)] \sinh(K_n L)} \right] \times \\ & \left\{ \left[ T_{L_0} \ln\left(\frac{r_1}{r_0}\right) (1 + \ln r_0) - T_{L_1} \ln(r_0) \right] \{J_0(K_n r_0) - J_0(K_n r_1)\} \right. \\ & \left. + (T_{L_1} - T_{L_0}) \{J_0(K_n r_0) \ln r_1 - J_0(K_n r_1) \ln r_0\} \right\} \\ & + \frac{2}{L} \sum_{n=1}^{\infty} \frac{\sin\left(\frac{n\pi z}{L}\right)}{G_n(r_1; r_0)} \left\{ G_n(r; r_0) \left(\frac{1}{n\pi}\right) [T_1 - T_{L_1} (-1)^n] + G_n(r_1; r) \left(\frac{1}{n\pi}\right) [T_0 - T_{L_0} (-1)^n] \right\} \quad (21) \end{aligned}$$

Equation 5 is now applied to determine the total heat exchange between the composite specimen bar and the insulation. In using this equation we assumed that the insulation thermal conductivity,  $K_i$ , was temperature and position independent. A temperature and spatially dependent conductivity could be introduced in evaluating the Equation 5 integral although it is important to bear in mind that this is still only an approximation since the use of the condition  $\nabla^2 T = 0$  implies temperature independent properties.

The final result of the substitution and integration of Equation 5 is as follows,

$$\begin{aligned}
 q_{\text{loss}} &= 2\pi r_0 k_i \int_0^L \left( \frac{\partial T}{\partial r} \right)_{r=r_0} dz = \\
 &2\pi r_0 k_i \left\{ 2 \sum_{n=1}^{\infty} \left[ \frac{G'_n(r_0; r_0)}{G_n(r_1; r_0)} \{T_1 - T_{L_1} (-1)^n\} + \frac{G'_n(r_0; r_1)}{G_n(r_1; r_0)} \{T_0 - T_{L_0} (-1)^n\} \right] \left\{ \frac{1 - (-1)^n}{n\pi} \right\} \right. \\
 &\quad \left. - \frac{2}{r_0 \ln \left( \frac{r_1}{r_0} \right)} \sum_{n=1}^{\infty} \xi_n \eta_n \frac{J_0(K_n r_1)}{J_0(K_n r_0)} \left[ \frac{\cosh(K_n L) - 1}{K_n} \right] \right\} \quad (22)
 \end{aligned}$$

where

$$\begin{aligned}
 \xi_n &= J_0(K_n r_0) / \left[ \{J_0^2(K_n r_0) - J_0^2(K_n r_1)\} \sinh(K_n L) \right] \\
 \eta_n &= T_{L_0} \ln \left( \frac{r_1}{r_0} \right) (1 + \ln r_0) - T_{L_1} \ln r_1 \left[ J_0(K_n r_0) - J_0(K_n r_1) \right] \\
 &\quad + (T_{L_1} - T_{L_0}) \{J_0(K_n r_0) \ln r_1 - J_0(K_n r_1) \ln r_0\} \\
 G'_n(r; r_0) &\equiv I_1 \left( \frac{n\pi r}{L} \right) K_0 \left( \frac{n\pi r_0}{L} \right) + I_0 \left( \frac{n\pi r_0}{L} \right) K_1 \left( \frac{n\pi r}{L} \right)
 \end{aligned}$$

Alternate terms of the first summation are zero due to the factor  $[1 - (-1)^n]$ ; hence only odd values of  $n$  need be considered. In the second summation, a determination of the eigenvalues  $\chi_n$  as defined by Equation 14 is necessary. An infinite series approximation given by Gray and Mathews (Reference 3) was applied; limited tabulations are also found in Jahnke and Emde (Reference 4). The first few roots are given in Table I for the case where  $r_1/r_0 = 6.0$ . For  $n > 6$  the roots are given to within 0.1% by Equation 23,

$$\chi_n r_0 = \frac{n\pi}{5} \quad (23)$$

TABLE I  
 POSITIVE ROOTS OF  $u_0(\chi'_n; r_0; r_1) = 0$  WHEN  $r_1/r_0 = 6.0$

n	$r_0 \chi'_n$	n	$r_0 \chi'_n$
1	0.226	5	3.134
2	1.233	6	3.764
3	1.874	7	4.393
4	2.506	8	5.023

Digital computer evaluation of Equation 22, a discussion of its convergence characteristics, and a comparison of the computer values with experimental heat loss measurements are given in the following section, which concerns the experimental performance of the apparatus.

### C. APPARATUS PERFORMANCE

#### 1. Thermal Conductivity Specimens

For the thermal contact resistance measurements, it is necessary to know the thermal conductivity of the test specimens quite accurately since these specimens are used as heat meters. A variety of thermal conductivity measurements were conducted on beryllium oxide (BeO) and tantalum with two objectives in mind: (1) to assess apparatus performance, and (2) to obtain accurate thermal conductivity data on the BeO for the later use in the contact resistance measurement series.

The beryllium oxide specimens were obtained from Coors Porcelain Company, Golden, Colorado. The Coors body designation was BD-995; the composition obtained by spectrographic analysis is given in Table II. The specimens were isostatically pressed from powder stock with average particle size of approximately one micron; prefired to 1100° C followed by drilling of the thermocouple instrumentation holes; and finally fired at 1690° C for approximately 4 hours. Based on a theoretical density of 3.01 the specimens were 94.7% dense. On the conductivity specimens the flat end faces were lapped to within 3 fringes (about 35  $\mu$ in.).

The tantalum specimens were obtained from Fansteel Metallurgical Corp., Chicago, Illinois. The sintered rod stock was unannealed, metallurgical grade and was fabricated into specimens in this condition. The composition is given in Table III. The theoretical

TABLE II  
COMPOSITION OF BERYLLIUM OXIDE TEST SPECIMENS

CONSTITUENT	WEIGHT PERCENT
$\text{Al}_2\text{O}_3$	0.30
$\text{SiO}_2$	0.18
$\text{MgO}$	0.10
$\text{Na}_2\text{O}$	0.05
$\text{CaO}$	0.02
$\text{Fe}_2\text{O}_3$	0.01
$\text{BeO}$	99.34

Density: 2.85 gms/cm<sup>3</sup>

Geometry: Cylinders - 1.0 inch diameter x 1.5 inch length

TABLE III  
COMPOSITION OF TANTALUM TEST SPECIMENS

CONSTITUENT	WEIGHT PERCENT
Ta	99.8 Minimum
Cb	0.02
C	0.03
Ni	0.02
Fe	0.02
Ti	0.01
Si	0.02
W	0.03
H	0.01
N	0.015
O	0.03
Density: 16.56 gms/cm <sup>3</sup> Geometry: Cylinders - 1.0 inch diameter x 2.0 inch length	

density was near 16.66 gms/cm<sup>3</sup>, thus this specimen material was 99.4% of theoretical. As a check of the metallurgical condition of the specimens, extensive Vickers hardness measurements were made. Generally, the Vickers hardness of tantalum is approximately 160 for unannealed material and drops to around 90 for fully annealed metal. Measured values of our tantalum specimens, in units of kgms/mm<sup>2</sup>, were nearly constant at 125, independent of load level variations from 150 to 1000 grams.

## 2. Thermal Conductivity Measurements on BeO

For the beryllium oxide thermal conductivity determinations, a 1.0 inch diameter x 1.5 inch length specimen was positioned between two Armo Iron cylinders of the same diameter. Armco iron is a widely used reference standard in comparative measurements, its conductivity being known with high accuracy (Reference 5). Very thin, 0.0001 inch platinum foil was placed between the contacting surfaces to reduce thermal contact resistance.

Reference grade 0.008 inch diameter Pt/Pt-10 Rh thermocouples were used throughout. The Armco Iron specimens had couples mounted in grooves on the surface and couples inserted radially to the specimen centerline. The centerline couples were mounted in two-bore 42 mil OD alumina tubing (high purity stock from McDanel). In all cases the thermocouple leads extended radially in a nearly isothermal plane for a distance of at least 2 inches. Temperature readings were taken with a Leeds and Northrup K-3 potentiometer. Thermocouple calibrations were run before and after the conductivity determinations. Maximum deviations were 0.2%. All measurements were conducted in vacuum, the level varying between  $1.0 \times 10^{-5}$  and  $1.2 \times 10^{-6}$  torr.

Two typical temperature distribution plots during the conductivity determinations are given in Figure 9. A dead weight compressive load of 375 psi was maintained on the test column to reduce interfacial temperature drops. The average contact conductance of the BeO/Armco interfaces with the platinum foil shim was about 1000 BTU/hr-ft<sup>2</sup> - °F. At a 375 psi load level this is a fairly high value for an interface with a brittle material component, and indicated that the platinum foil was effective. Figure 9 shows the consistency of the temperature readings to be quite good. The guard was adjusted such that it matched closely the temperature gradient in the BeO test specimen.

The thermal conductivity results are given in Figure 10 along with several curves from the literature for BeO specimens in the same density and purity range (References 6-9). For clarity, a curve has not been drawn through the data points obtained in this investigation. The precision of the data was found to be better than  $\pm 2\%$ . An exact accuracy figure relative to literature results was not calculated since slightly differing curves were obtained by various investigators using material of the same composition studied here. A 3% scatter interval is shown, however, to indicate the close agreement between literature values and the data obtained here. The experimental data are tabulated in Appendix IV.

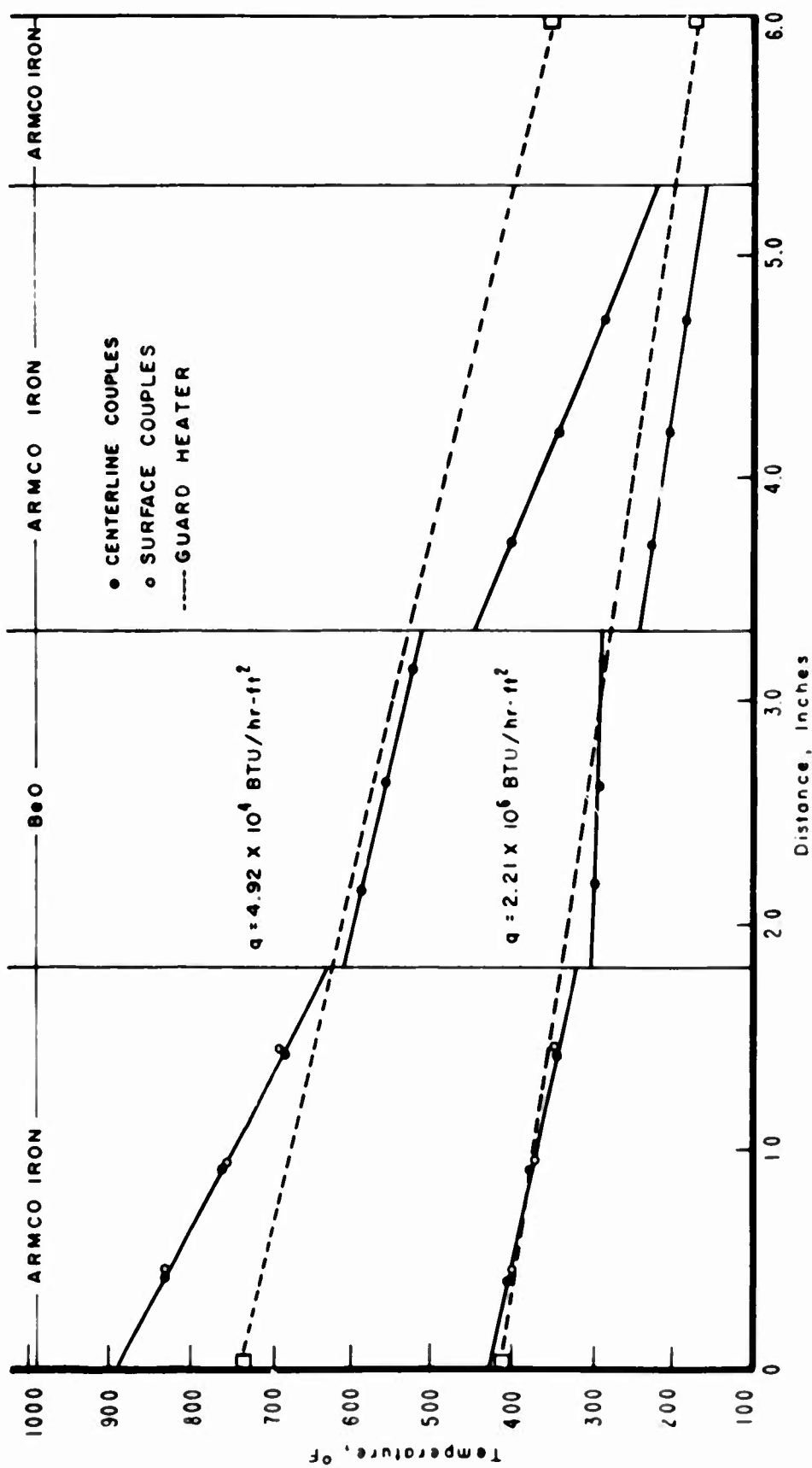


Figure 9. Typical Temperature Distributions During BeO Thermal Conductivity Measurements



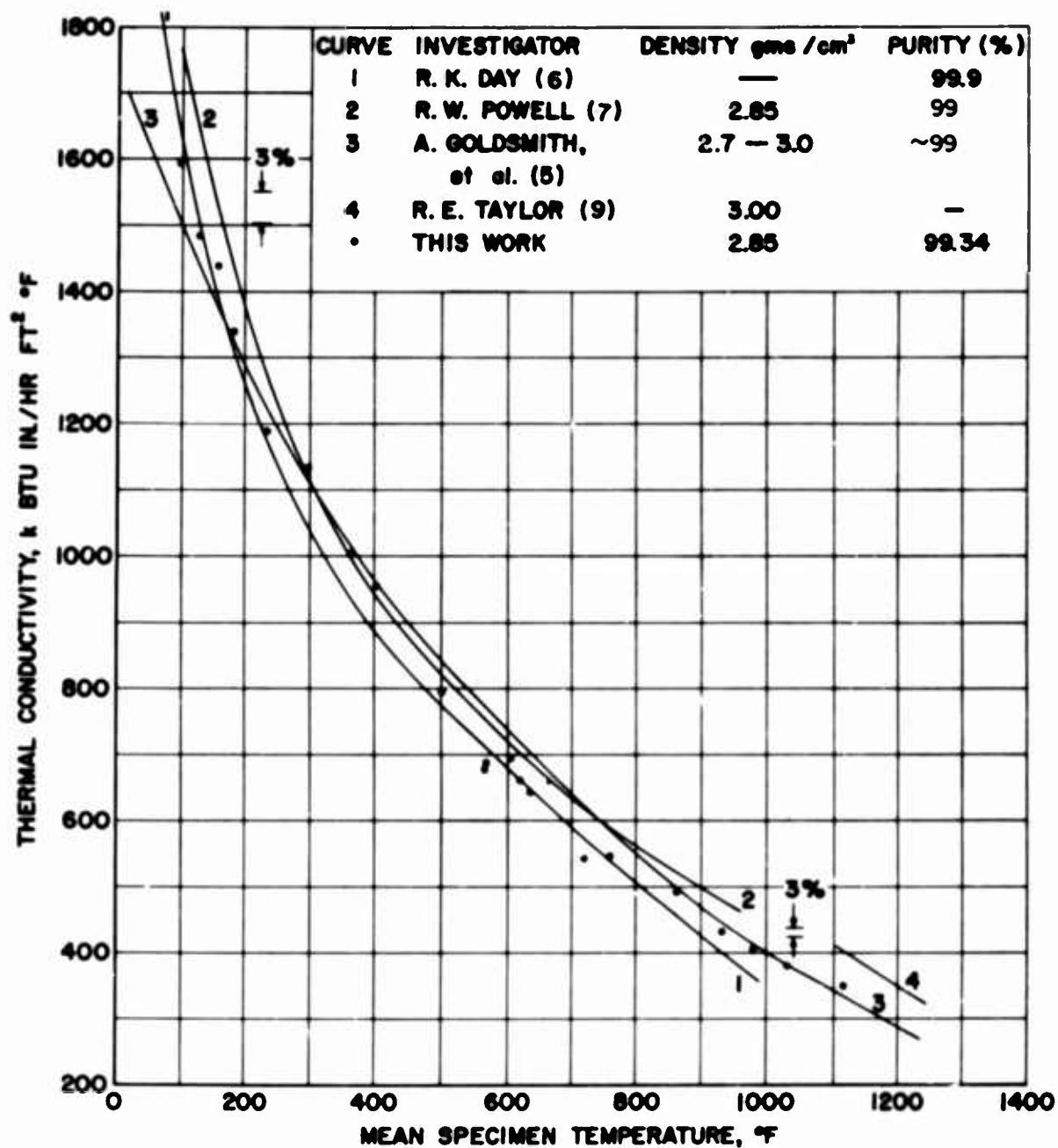


Figure 10. Thermal Conductivity of Beryllium Oxide as a Function of Temperature

For beryllium oxide and other dielectric materials the thermal conduction process is due entirely to phonon transport, the electronic contribution being negligible. Applying the conventional mean free path concept, this lattice thermal conductivity can be expressed as

$$k_l = \frac{1}{3} C_v V \phi \quad (24)$$

Correlations of phonon scattering predict that  $\phi$  for crystalline dielectrics is nearly proportional to  $1/T$ . Since  $V$  is a weak function of temperature (proportional to the 0.5 power of the elastic modulus) and since  $C_v$  is approximately constant in the temperature range studied here, it is expected that the thermal conductivity of BeO would be proportional to  $1/T$ . This dependence should be obeyed to temperatures of about 3000° F, where radiation heat transfer starts to become significant (Reference 10).

The experimental results of this investigation are replotted in this form in Figure 11 together with data from the literature (References 6, 7, and 11). The "recommended" curve in this figure was formulated by the Thermophysical Property Research Center and based on an analysis of about 50 different sets of literature data on BeO. This curve is for material of theoretical density,  $\rho = 3.01$ . Its agreement with theory is excellent, the data clearly defining a straight line. Further, this line falls between the curves obtained by other investigators for material in the same density and purity range. The experimental data points of Powell and Day are not plotted in Figure 11 to avoid cluttering. Separate plots of their data produced scatter about the same as that observed in this investigation. Based on this correlation the conductivity data from this investigation was extrapolated to 1800° F, this being the maximum temperature to which conductivity data were required in the contact resistance computations. The highest temperature data point was taken at 1120° F.

### 3. Thermal Conductivity Measurements on Tantalum

Measurements with tantalum were performed in a manner identical to those with BeO. The scatter of the data points about a mean line through them was a small degree higher than that observed with the BeO, the maximum amounting to  $\pm 1.5\%$ . The data are plotted in Figure 12 together with data from the literature. The numerical value tabulation is included in Appendix D.

The most probable value of thermal conductivity for this metal is more open to question than for the beryllium oxide, as is apparent from the curves in Figure 12. For this reason the recommended curve is somewhat uncertain. The data from this work agree with the

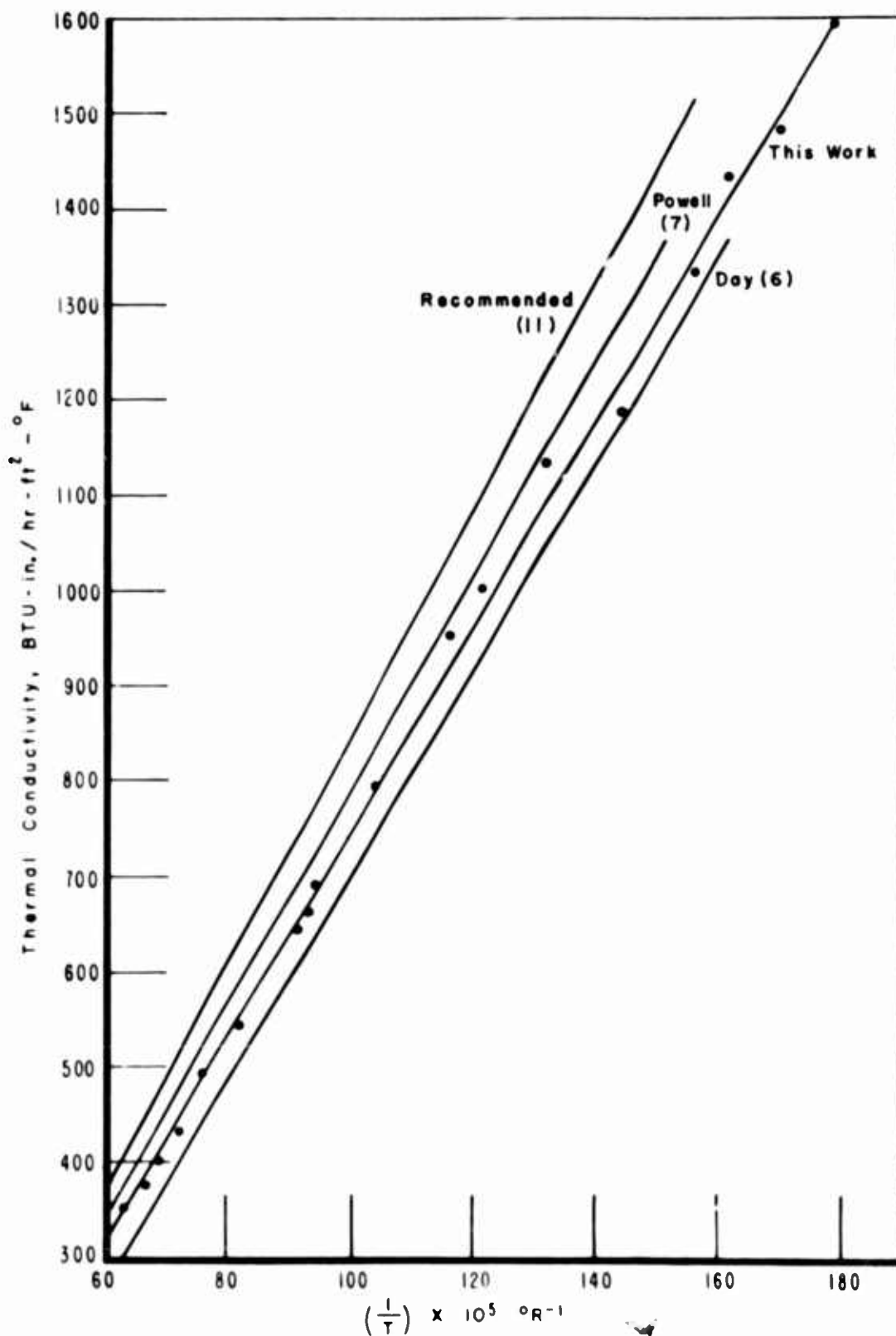


Figure 11. Thermal Conductivity of Beryllium Oxide Plotted as a Function of  $(1/T)$

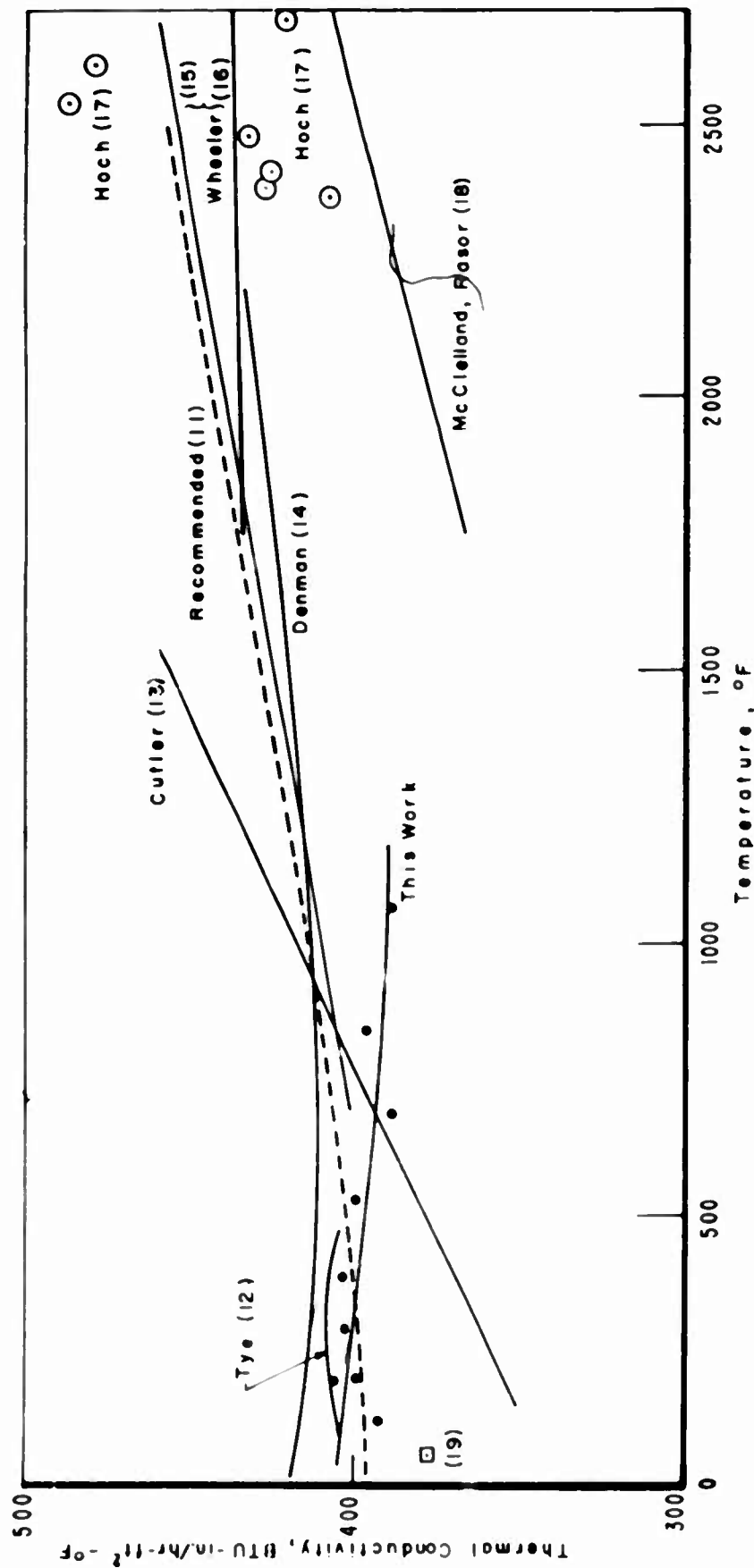


Figure 12. Thermal Conductivity of Tantalum as a Function of Temperature

recommended curve in the range from room temperature to 500° F, but because of a difference in slope, there is a 7.5% disagreement at the highest test temperature, 1150° F. However, other literature data at much higher temperatures show disagreement with the recommended curve ranging from 0.1 to 15%, and the deviations are in the same direction as those for the data obtained here. From limited electrical resistivity measurements and application of the Wiedeman-Franz relationship it has been estimated that the electronic component of the thermal conductivity of tantalum is approximately 88% (Reference 12). The lattice component is thus about 12%. Some of the disagreement among authors indicated in Figure 12 could be resolved if electrical resistivity data were available. Such measurements have not yet been made on the tantalum studied in this investigation since it was beyond the scope of the project. It is felt, however, that the tantalum conductivity results are a further demonstration of the successful performance of the equipment used in this report.

#### 4. Heat Loss Measurements

During the beryllium oxide conductivity determinations, data was obtained on heat exchange between the insulation and the specimen column. This data consisted of measured differences between the heat flux through each of the meter bars as a function of absolute temperature level and variations of the flux in the specimen column as the guard heater temperature distribution was changed.

To evaluate Equation 22, it was necessary to have vacuum environment values of the alumina bubble insulation conductivity,  $k_i$ , as a function of temperature. The rationale for determining this functionally is given in Appendix III. Table 11, Appendix A, gives a summary of the temperature distribution and insulation conductivity data required in Equation 22.

In evaluating the series in Equation 22, term by term printout of the computer results was employed to observe convergence characteristics. Hand calculation of several terms was also run to check the computer results. The first series was carried to  $N = 40$ . For  $n > 20$  each term contributed no more than 0.3% to the sum. In the case of the second series, the first term in the summation, represented by  $K_1$ , varied between 70 and 93% of the series sum. Subsequent terms alternated sign with decreasing magnitude as might be expected for a series having linear  $J_0(K_n r)$  factors. Summation through  $K_9$  was performed to obtain a sum varying less than 1% with inclusion of higher terms.

The comparisons between the experimental heat loss measurements and those predicted by Equation 22 are given in Table IV as percentages of the average heat flux in the specimen column. Positive values represent heat flow from the specimen column into the insulation.

TABLE IV  
EXPERIMENTAL-ANALYTICAL HEAT EXCHANGE COMPARISONS

Data Point	Average Heat Flux in the specimen Column (BTU/hr)	Predicted Value %	Experimental Value %
2	37.4	2.6	5.4
4	62.7	2.8	6.4
9	193.5	7.1	5.5
10	230.7	9.0	5.4
11	230.3	10.0	5.4
12	229.3	11.9	4.1
13	276.5	14.0	4.0
15	354.0	16.8	-1.1
18	443.7	19.7	-5.5

If  $(T_{\text{BeO}})_m$  is the midpoint temperature of the beryllium oxide specimen and  $T_{\text{guard}}$  is the guard heater temperature at the same axial position, then  $(T_{\text{guard}}/(T_{\text{BeO}})_m - 1)100$  is the percentage by which the guard temperature exceeds that of the BeO specimen; this quantity will be termed the guard mismatch. For data points 10-12, the mean temperature of the BeO was held approximately constant, while the guard mismatch varied from 8 to 23%. As seen in Table IV the heat exchange between specimen column and insulation varied only 1.3% as observed experimentally and only 2.9% according to the analytical prediction. Thus, thermal guarding of the specimen column does have an effect on the heat flowing in the column but as suggested in the design philosophy, the effect is not of high sensitivity. The experimental conductivity data was obtained with guard mismatching ranging from +23 to -11%. Across this wide range the average heat exchange between insulation and specimen column was 4.7%.

It is important to note that there is some uncertainty in the experimental heat exchange values. For data points 10 and above these exchange values are obtained by taking the difference between large heat flux values, hence uncertainty in these fluxes greatly accentuates uncertainties in the heat exchange values. For data points 1 to 9 the principal uncertainty in the heat exchange values is the error in the temperature gradient determinations

in the meter bars above and below the BeO specimen. This uncertainty is particularly important for the lower temperature data points where the overall temperature drops in the meter bars are relatively low.

The change in sign of the experimental heat exchange values for the higher temperature data points are internally consistent. That is, in the cases where the exchange is positive (heat flow into the insulation), the thermocouples on the specimen surface give lower readings than those in the same plane at the specimen centerline. When the experimentally observed heat exchange values change sign, the surface thermocouples are found to read higher than the corresponding centerline couples.

Now, a comparison of the experimental heat exchange values with the analytical predictions, based on the uncertainties in the experimental values discussed above, shows the predictions consistent at least through data point 13.

The last two data point comparisons in Table IV require further elaboration. The experimental thermocouple data reveals an uncertainty of gradient in the meter bars of 3.1%. In the cases where the measured heat exchange is near zero and going negative this uncertainty in the meter bar gradient introduces a particularly large uncertainty in the heat exchange value. The range for data point 15 is from -1.1 to +2.8%, and for data point 18, from -5.5 to -2.2%.

Further, the magnitude of the heat exchange is large here compared with the low temperature cases. For data points 15 and 18 this radial flux is from 10 to 12 times that for data point 2. For these higher temperature data points, the comparatively high radial fluxes introduces the possibility of significant temperature drops at the specimen-insulation interfaces and the insulation-guard heater interface. These temperature discontinuities result from the contact resistance associated with the interfaces and become significant when the radial flux is large. If a conservatively high interface thermal contact conductance of  $20 \text{ BTU/hr-ft}^2\text{-}^\circ\text{F}$  is assumed, the interfacial temperature drop is at least  $20^\circ\text{F}$  for the last two data points in Table IV. This factor is significant with respect to the analytical predictions because the temperature distributions used in evaluating Equation 22 were not measured directly in the insulation but in the specimen column and the guard heater ring. This is certainly one of the largest factors in the disagreement between the heat exchange values for the high temperature data points.

In general, the heat exchange predictions are of the right magnitude. However, it is apparent that to provide a more rigorous test of heat exchange predictions it would be necessary to conduct extensive measurements with that specific aim in mind. Such measurements would be most difficult to perform due to the necessity of accurately measuring temperatures directly in the low density insulation material. The temperature field equations developed earlier can easily be generalized for predicting heat flows in any right-circular element with arbitrary boundary conditions. For this more general application, the temperature would be written in dimensionless form such as an unaccomplished temperature ratio, and the physical dimensions of the hollow cylindrical element would also be written in dimensionless form.



### SECTION III

## CONTACT RESISTANCE RESULTS

#### A. CONTACT SURFACE CHARACTERIZATION

Because contact surface condition has a great influence on interfacial heat transfer, surface preparation and characterization were carefully controlled from the inception of the program. It was concluded that surfaces with random roughness were most desirable for study. In this context "random" implies a roughness independent of position on the surface. To develop this condition, the beryllium oxide surfaces were first polished flat with diamond paste to within 3 interference fringes. This was followed by a vapor-blasting operation which produced finishes in two roughness ranges: nominally 10 and 40  $\mu$  in. centerline-average (CLA). These designations were used simply for shop control of the roughness range.

Detailed quantitative surface characterization was accomplished with a high precision profilometer. The instrument employed was a Taylor-Hobson "Talysurf" Model 3 profilometer with a 0.0001 inch radius diamond stylus. Horizontal drive speeds giving 20 and 100X magnification were used. Vertical amplifications of from 1000 to 50,000X were used depending on the type of surface irregularity being studied. The physical configuration of the various components is shown in Figure 13.

Two types of surface characterization data were obtained: waviness and roughness traces. In the waviness measurements, relatively large scale surface undulations were recorded by tracing the specimen surface with the stylus support arm moving along an external optical flat. The flat thus provided a reference line external to the specimen surface. Vertical magnification on these traces was fairly low to follow surface irregularities of large amplitude. In the roughness measurements the vertical amplification was increased to observe small scale surface irregularities having amplitudes on the order of a few micro-inches. To prevent the surface waviness patterns from driving the roughness traces off scale at these high amplifications, an external reference line was not used. Rather, the specimen surface itself was used as a reference, the stylus following a small skid or shoe that moved ahead of the recording tip.

The difference in surface character between the 10 and 40  $\mu$  in. specimens is shown in Figure 14. Note that the vertical magnification on the 10  $\mu$  in. specimen trace is twice that of the 40  $\mu$  in. specimen trace. The 10  $\mu$  in. trace reflects the higher degree of surface



Figure 13. Surface Characterization Equipment

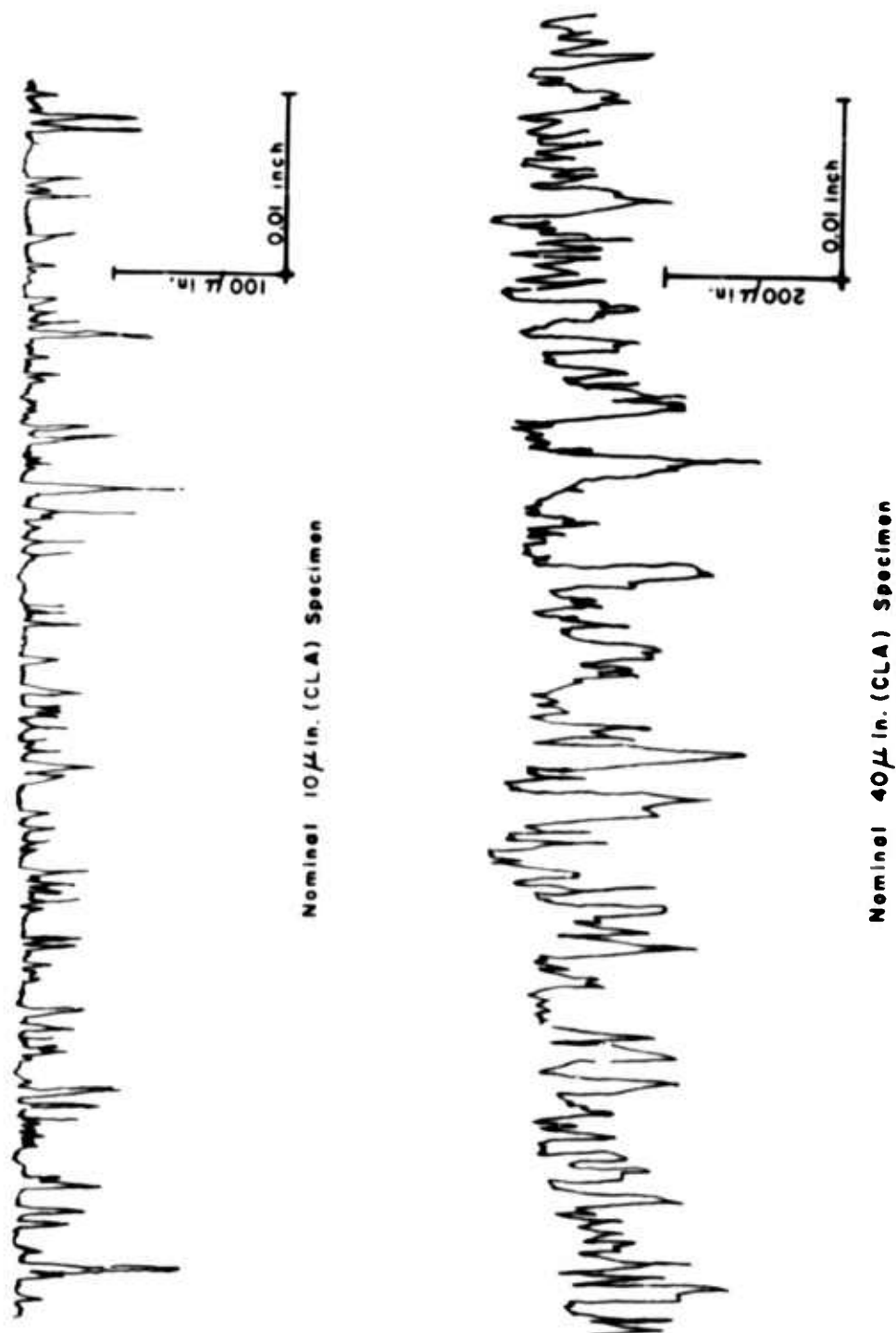


Figure 14. Surface Roughness Profile Traces

polish used to obtain the smoother finish. For both roughness and waviness characterization, numerous traces were run at different orientations across the specimen surfaces. These studies confirmed the random lay of the surface roughness.

A typical waviness trace is shown in Figure 15. When diametrical traces of this form were run, it was observed that the shape of the profile was independent of the orientation of the specimen. This leads to the conclusion that the waviness irregularities were in the form of concentric circular patterns. This observation is consistent with the specimen fabrication and surface finishing procedures used and was of considerable consequence in the formulation of the interfacial contact model outlined in the discussion of results (Section IV).

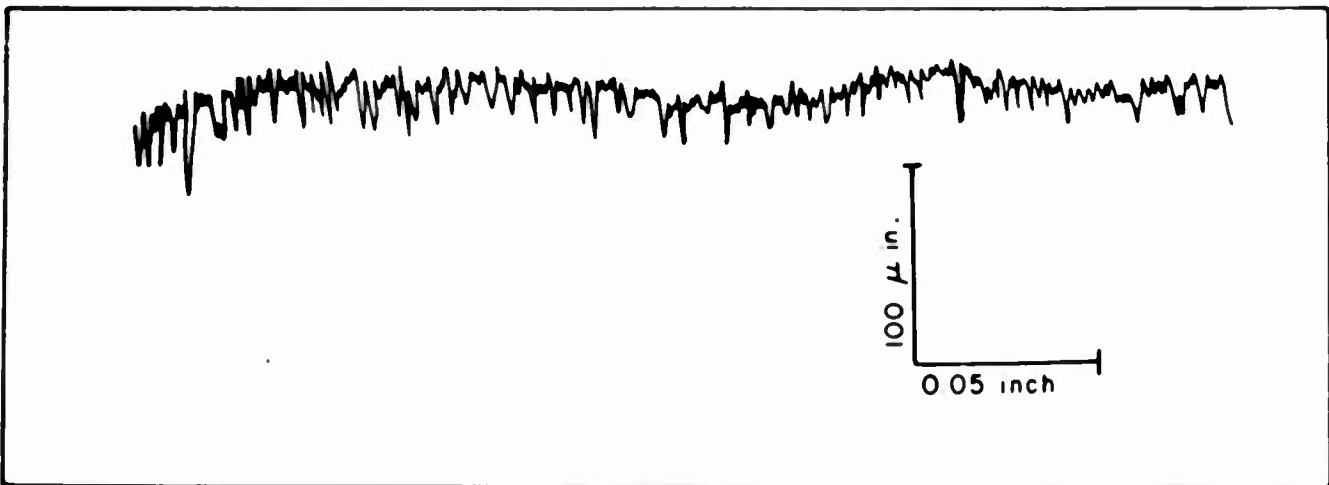


Figure 15. Surface Waviness Profile Trace

For the contact resistance correlations as a function of compressive load, it was necessary to know the variation in the solid-solid contact area as the surfaces were pressed together. Plots of this form are given in Figure 16 which were generated in the following fashion. First, a linear least squares line was fitted through the profile traces in Figure 14 such that the average distance between "peaks" and "valleys" on either side of the line was the same. A reference line with the same slope was then displaced upward until it just touched the uppermost peak. A family of parallel lines was then drawn at various distances between the reference line and the least-squares line. The percentage of solid area intercepted by each of these lines was plotted as a function of their distance from the reference line to give the roughness curves in Figure 16. The waviness plots in this figure were generated in a similar fashion using data of the form shown in Figure 15.

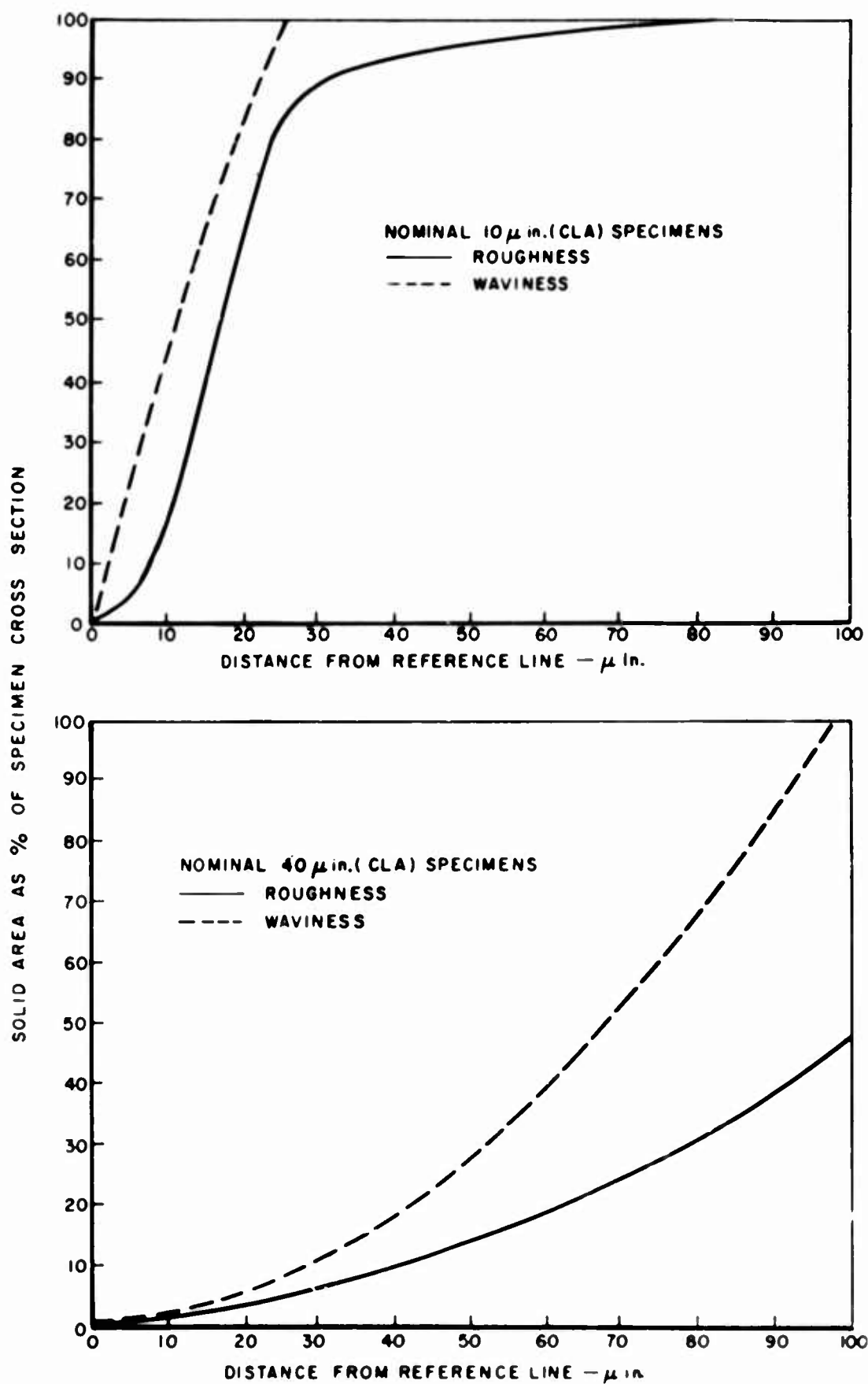


Figure 16. Solid Area as a Function of Vertical Displacement

The quantitative data in Figure 16 reflect the surface characteristics which are evident in Figure 14. For the rougher surface, the increase in solid area with vertical displacement is quite gradual. On the same displacement scale, the increase in intercepted area is much more abrupt for the smoother surfaces. Even though the waviness irregularities are of much lower frequency than that of the roughness, the amplitudes are of the same order of magnitude in each surface finish range. Further discussion of these distinctive characteristics will be given in Section IV.

## B. MEASUREMENT PROCEDURE

The beryllium oxide thermal contact resistance specimens were of the same configuration as the thermal conductivity specimens: right circular cylinders of 1.0 inch diameter and 1.5-inch length. Each specimen was instrumented with three centerline thermocouples mounted at axial distances of 0.20, 0.70, and 1.20 inches from the contact interface. The thermocouples, with inert gas welded junctions, were formed of 8 mil pt versus 8 mil pt/10% Rh and inserted in 0.042 inch OD two bore tubing of high purity aluminum oxide. To ensure good physical contact with the specimens, the tips of the couples were wound with fine platinum wire, and the aluminum oxide probes were then force-fit into the 0.048 inch radial holes drilled to the specimen centerline. The centerline thermocouple positions were determined by observing the inclination of rigid steel pins inserted full depth into the instrumentation holes. A traveling stage microscope was used for this purpose.

After assembly of the apparatus in a configuration similar to that shown in Figure 2, the thermocouples were checked by taking room temperature readings with respect to the ice point. Post test elevated temperature calibrations were run also; in both cases consistent readings within  $\pm 1 \mu$  volt ( $\pm 0.2^\circ$  F) were obtained. A predetermined compressive load was applied and after reaching a vacuum level of at least  $5 \times 10^{-6}$  torr, the power to the main heater was adjusted to the desired mean interface temperature. The guard heater was then adjusted to match the gradient in the contact resistance column. Typical temperature distributions were similar to those shown in Figure 9, except that only beryllium oxide specimens were involved. Depending on the temperature level, a period of between 8 and 24 hours was allowed for system stabilization before temperature readings were recorded. The longer time periods were required at low temperatures due to system thermal inertia. Provisions were made for automatic temperature adjustment of the guard heater relative to the main heater; however, manual adjustments were used most of the time because the thermal inertia of the system changed with temperature level. Steady-state conditions were defined such that, with matched guarding, the temperature variations were less than  $1.0 \mu$  volt ( $0.2^\circ$  F) over the period of readout (approximately 1 hour).

Temperature readings were taken with a Leeds and Northrup K-3 potentiometer with reference junction compensation. Readings were made to within  $\pm 0.1 \mu$  ( $\pm 0.02^\circ \text{F}$ ). The magnitude of the interfacial temperature drop was determined by extrapolating the temperature profiles in each specimen to the contact interface. Deviations of the specimen gradients from linearity due to the temperature variation of the thermal conductivity had an extremely small influence on the calculated interfacial drop. Because the overall temperature drops in the specimens were small, no deviations from the linear gradient condition were noted except at the highest test temperature. To minimize errors, all temperature discontinuity calculations were made numerically; graphical plots of the temperature distributions were used only to check relative consistency of the readings.

The thermal conductivity data obtained in Section II. C. 2. and the measured temperature gradients in the two BeO specimens were used to calculate the heat flux crossing the interface. The ratio of the interfacial temperature drop to this average heat flux gave the thermal contact resistance in units of  $(\text{BTU}/\text{hr-ft}^2\text{-}^\circ \text{F})^{-1}$ . The difference in the heat flux in the specimen above and below the interface gave a quantitative measure of heat exchange with the surrounding insulation.

After data was taken at one temperature level, the power to the main heater was increased followed by equilibration of the guard cylinder temperature distribution. When a full curve of contact conductance as a function of mean interface temperature had been generated at a given load level the system was cooled. In some cases, data points were taken during the cooling cycle. After increasing the compressive load, another contact resistance curve was obtained. Typical variations of the measured quantities are given in Table V along with the resulting uncertainty in the contact resistance calculation.

Several important points can be distinguished in Table V. In operation of the apparatus, an increase in mean interface temperature is attained by increasing the main heater temperature, the "cold-end" temperature remaining essentially constant. Thus, as the temperature level of the interface increases, two effects are occurring simultaneously: (1) the overall temperature drop down the column is increasing, and (2) the specimen thermal conductivity is decreasing rapidly. Since the overall heat flux is proportional to the product of these quantities, it is noted in this column of Table V that the increasing gradient effect predominates at lower temperatures (increasing flux) while decreasing specimen conductivity predominates at the higher temperatures (decreasing flux). The uncertainty in the heat flux involves several factors: (1) the uncertainty in the temperature gradient

TABLE V  
CONTACT RESISTANCE ERROR ANALYSIS RESULTS

Mean Interface Temperature Range ° F	Temperature Gradient		Interfacial Temperature Drop		Heat Flux		Contact Resistance	
	Range ° F/in.	Error %	Range ° F	Error %	Range BTU hr-ft <sup>2</sup>	Error %	Range hr-ft <sup>2</sup> -° F BTU	Error %
<u>Low:</u> 100 - 500°	7.6	±9.2	70.2	±0.6	4442	±11.1	0.011	±12.0
<u>Intermediate:</u> 500 - 1000°	18.9	±1.8	129.0	±0.4	8744	±13.7	0.015	±13.8
<u>High:</u> 1000 - 1500°	11.4	±8.0	75.0	±1.4	2410	±19.4	0.032	±23.4



reflected in the second column of Table V, (2) the specimen thermal conductivity uncertainty amounting to  $\pm 2\%$  (Section II. C. 2), and (3) heat exchange with the thermal insulation due to small radial temperature gradients.

At lower temperatures the uncertainty in the thermal contact resistance is due mainly to errors in the gradient determination. These net gradients are small for two reasons: (1) the heat flux is low, and (2) the thermal conductivity is high. At high temperatures the exchange of heat between the specimen column and the insulation becomes important because the insulation thermal conductivity is increasing (Appendix III), while the magnitude of the specimen column flux is decreasing due to the drop in conductivity. The combined influence effects (Table V) on the contact resistance measurements is minimized in the intermediate temperature range.

A complete tabulation of the experimental result is given in Appendix IV. Graphical presentation of the results along with brief qualitative interpretations are given in the next section.

### C. GRAPHICAL PRESENTATION AND QUALITATIVE INTERPRETATION OF RESULTS

The graphical presentation of measurement results giving the contact conductance as a function of mean interface temperature are presented in the next 10 Figures, Figures 17-26. The first five are for the 40  $\mu$  in./40  $\mu$  in. interface at compressive load levels ranging from about 5 psia to about 500 psia. The second group of five is for the 10  $\mu$  in./10  $\mu$  in. interface covering about the same sequence of compressive load levels. Formulation of an interfacial heat transfer model and correlation of the experimental results are given in Section IV. The following brief discussion merely points out the general features and trends in the data.

In comparing the contact conductance ordinate on Figures 17-21 for the 40  $\mu$  in./40  $\mu$  in. interface, it is noted that the contact conductance level increases rapidly as the compressive load increases. The  $h_c$  values range from about 20 Btu/hr-ft<sup>2</sup>-°F at a compressive load of approximately 5 psia to about 250 at a load of 511 psia. A similar load dependence of  $h_c$  for the smoother 10  $\mu$  in./10  $\mu$  in. interface is noted in Figures 22-26. Because the contacting surfaces are much smoother in this second sequence of tests, the level of interfacial conductance is higher by a factor of between 3 and 4 at any given load. The range of  $h_c$  is from about 60 to 1000 for compressive loads ranging from about 5 to 500 psia. The scatter in the experimental data tends to decrease as the load level increases in accordance with the observations of the previous section.

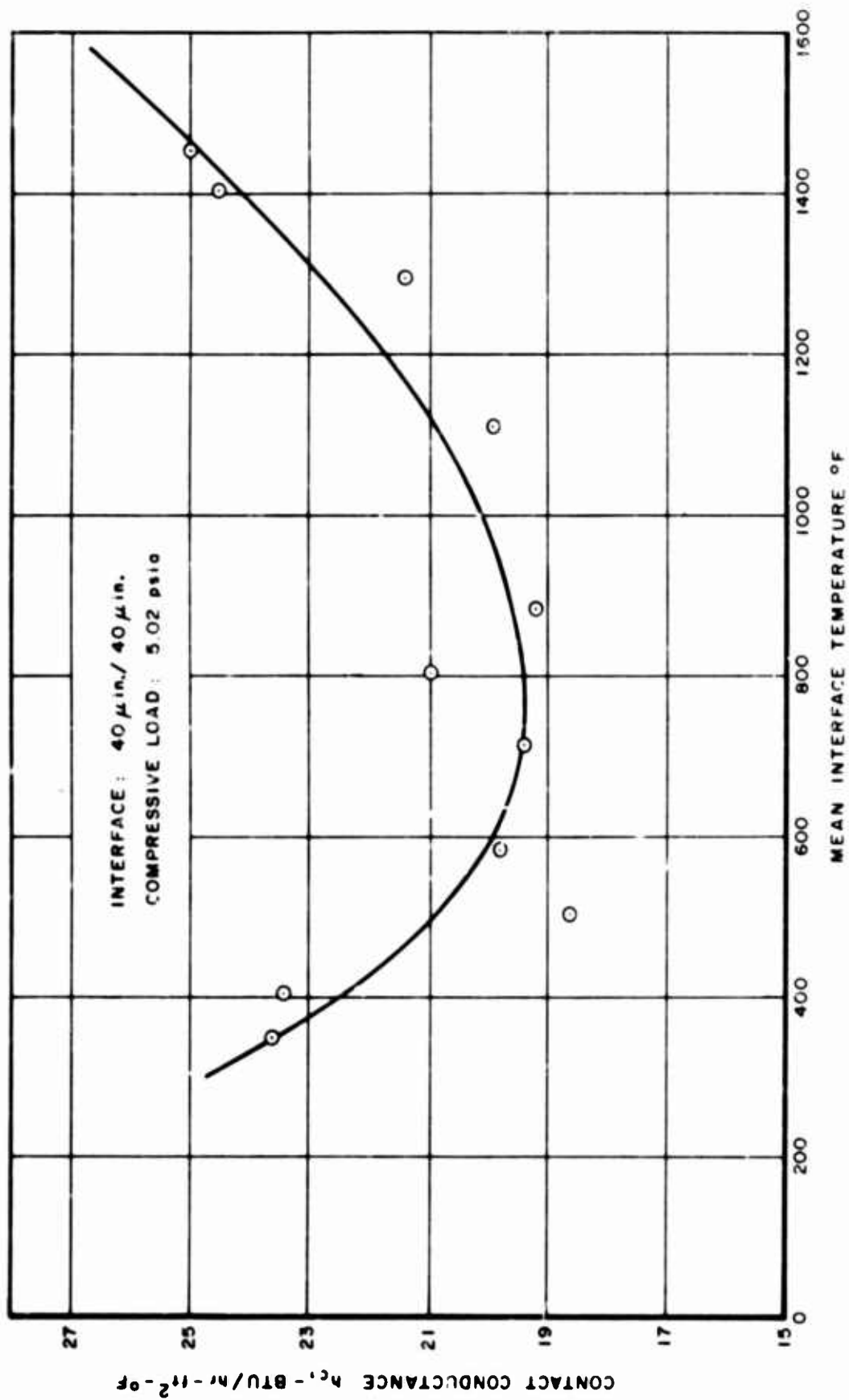


Figure 17. Contact Conductance as a Function of Interface Temperature:  
40  $\mu$ in./40  $\mu$ in. Interface, 5.02 psia Compressive Load

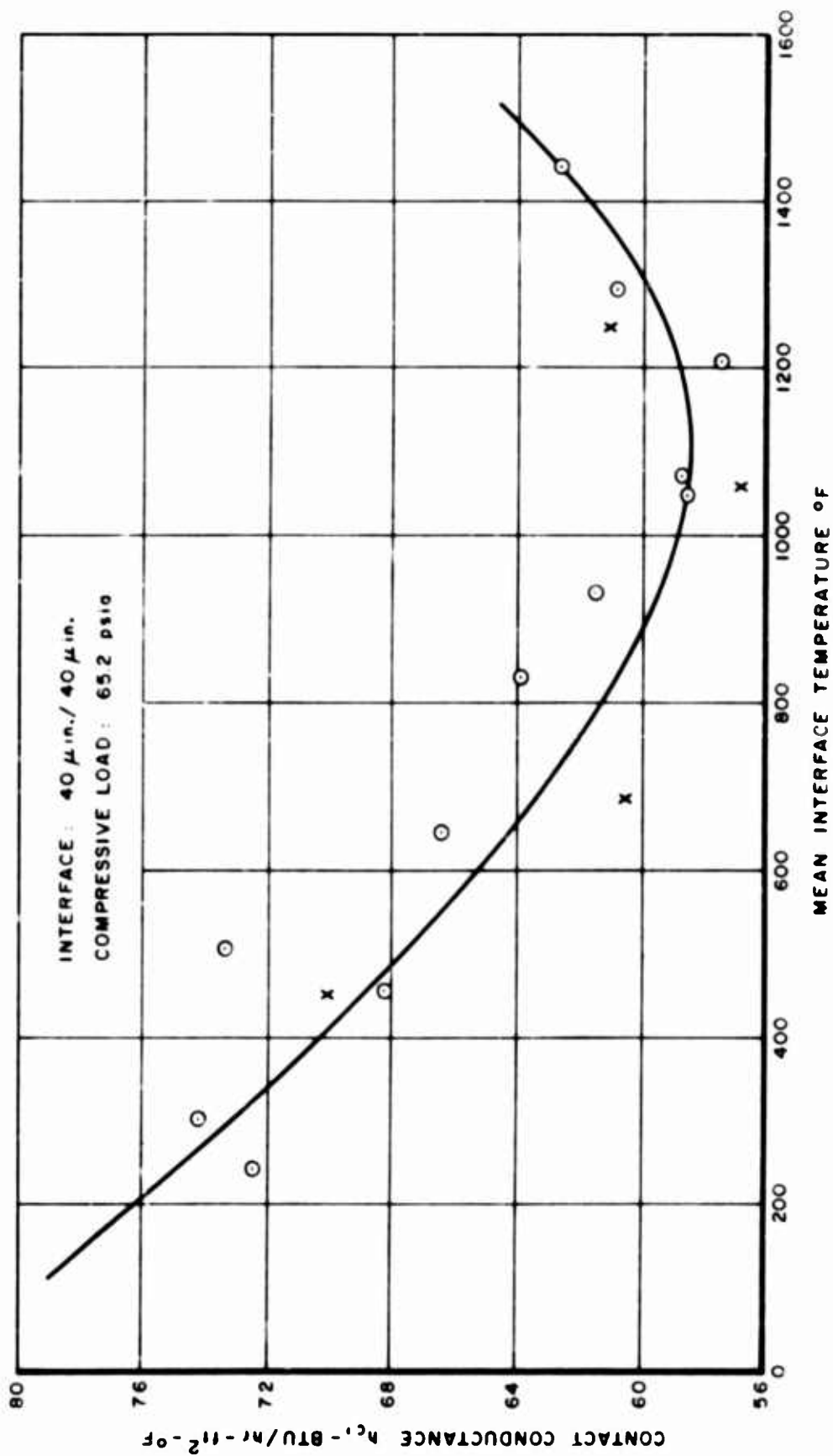


Figure 18. Contact Conductance as a Function of Interface Temperature:  
40  $\mu$ in./40  $\mu$ in. Interface, 65.2 psia Compressive Load

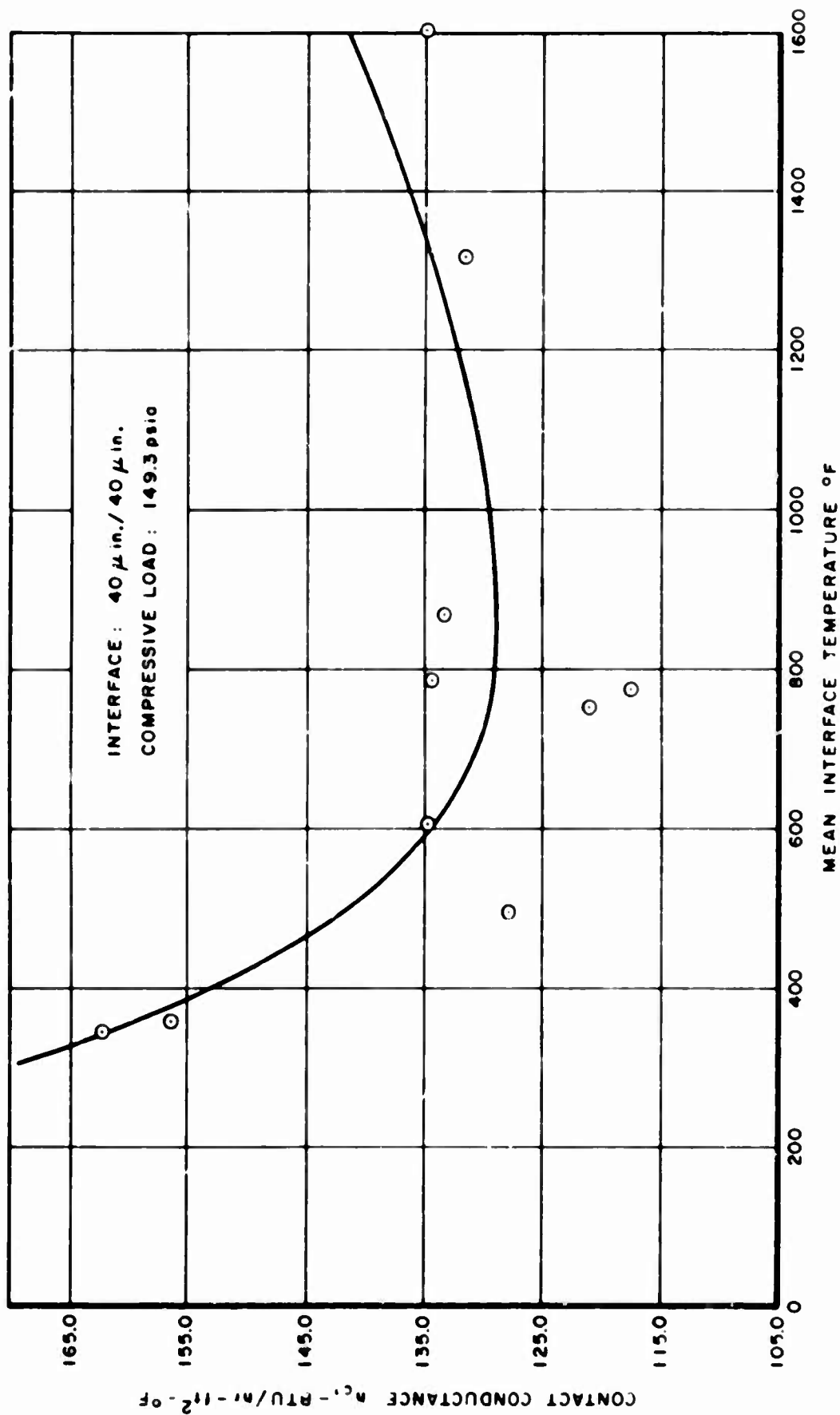


Figure 19. Contact Conductance as a Function of Interface Temperature:  
40  $\mu$ in./40  $\mu$ in. Interface, 149.3 psia Compressive Load

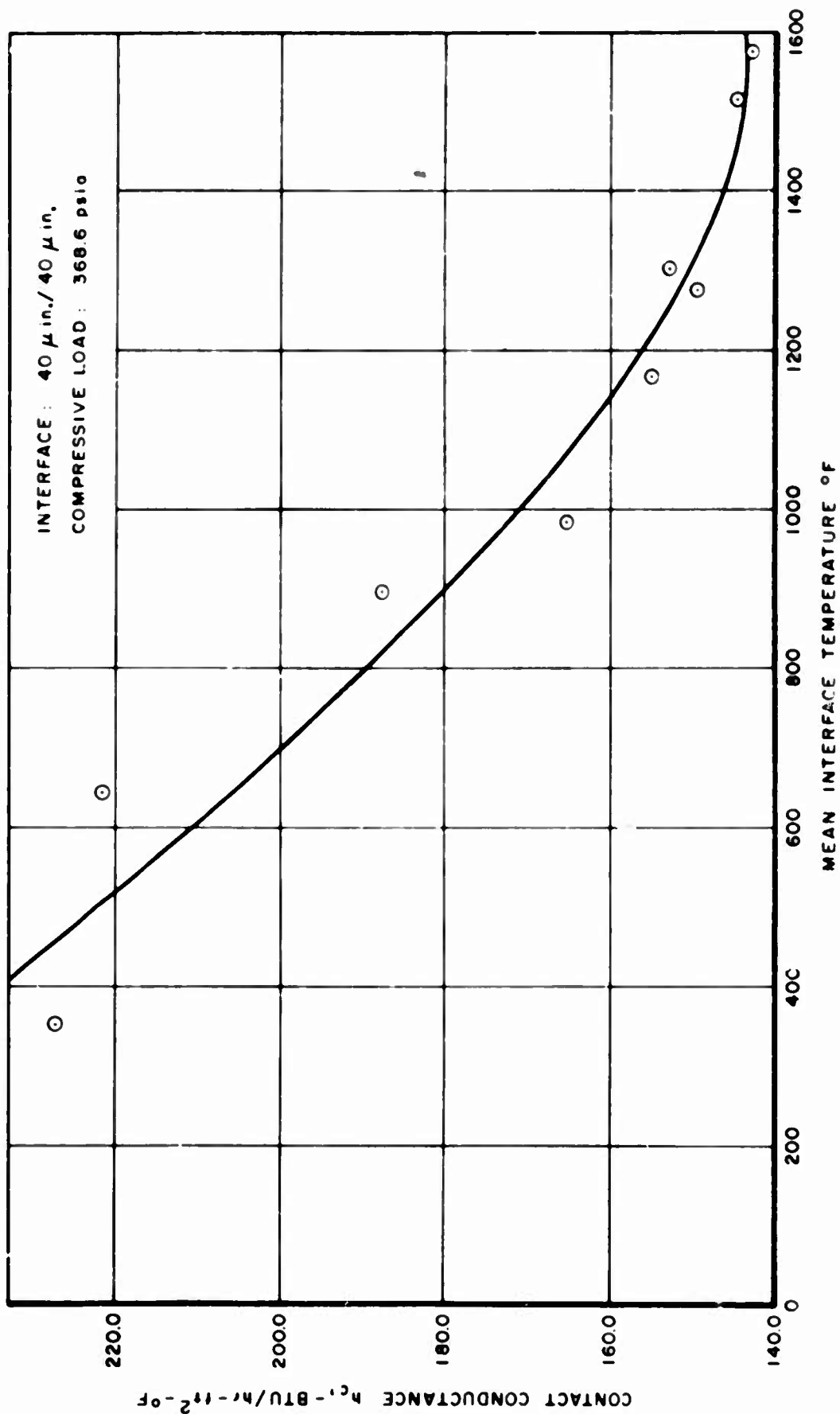


Figure 20. Contact Conductance as a Function of Interface Temperature:  
40  $\mu$ in./40  $\mu$ in. Interface, 368.6 psia Compressive Load

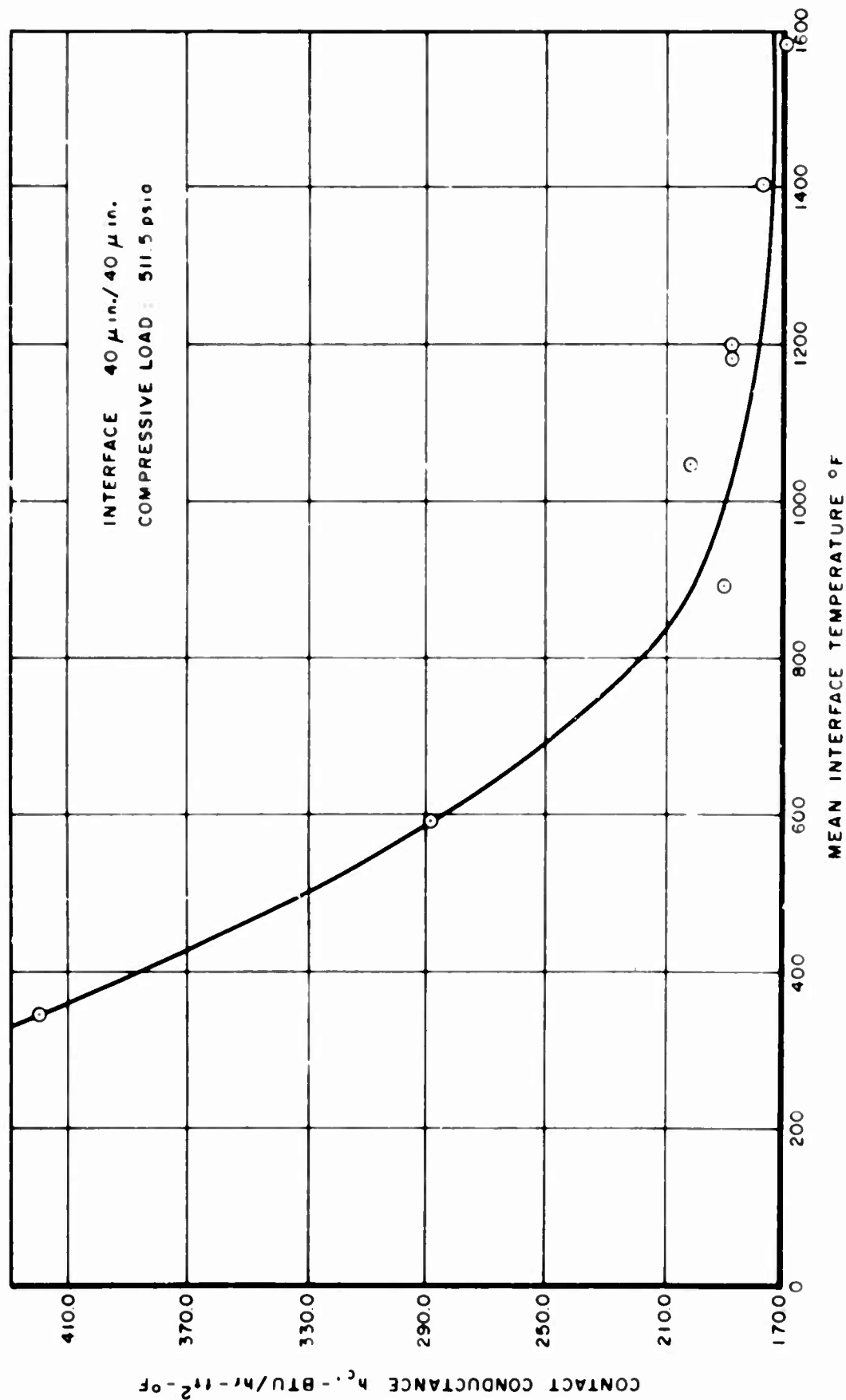


Figure 21. Contact Conductance as a Function of Interface Temperature:  
40  $\mu$ in./40  $\mu$ in. Interface, 511.5 psia Compressive Load

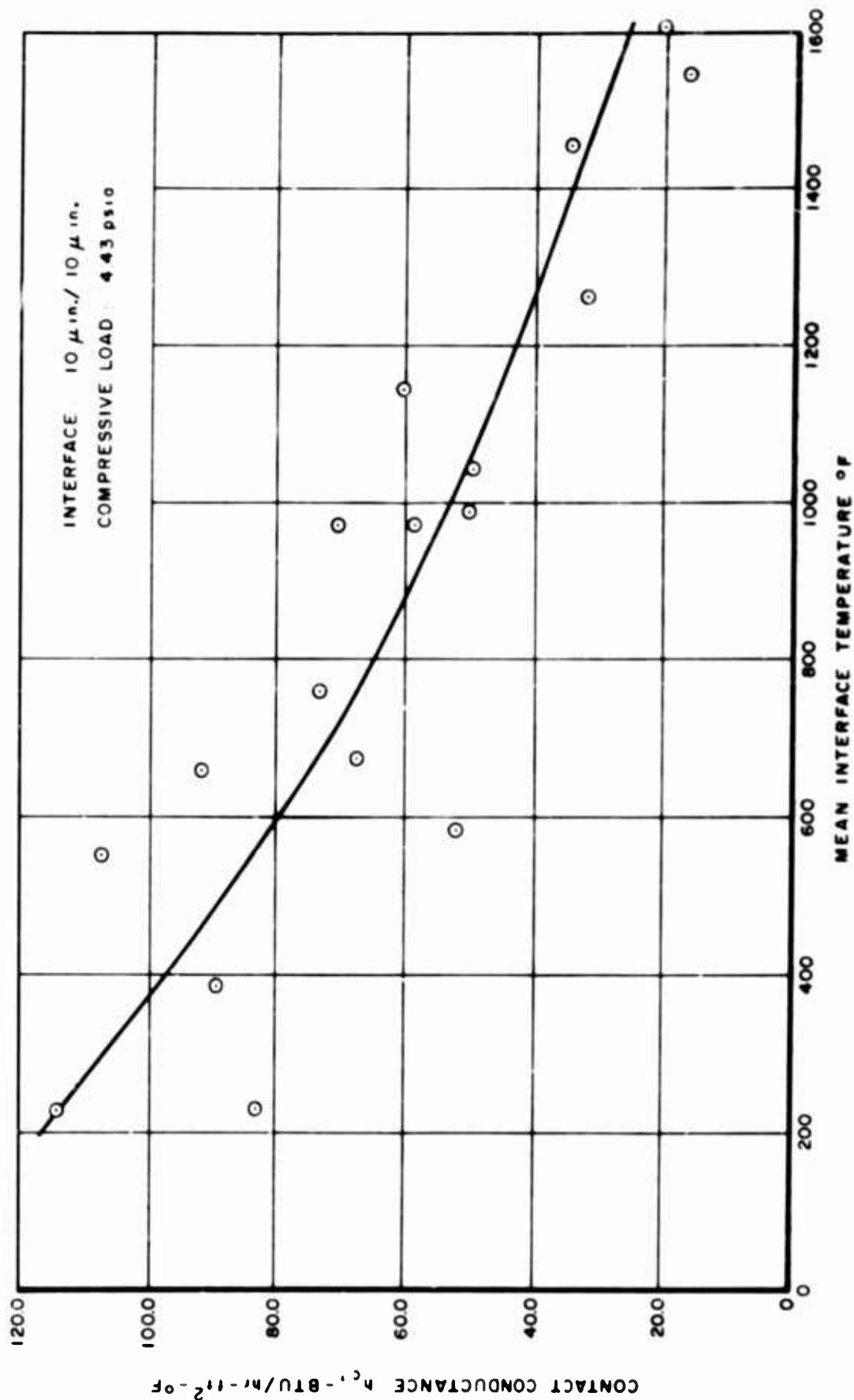


Figure 22. Contact Conductance as a Function of Interface Temperature:  
10  $\mu$ in./10  $\mu$ in. Interface, 4.43 psia Compressive Load

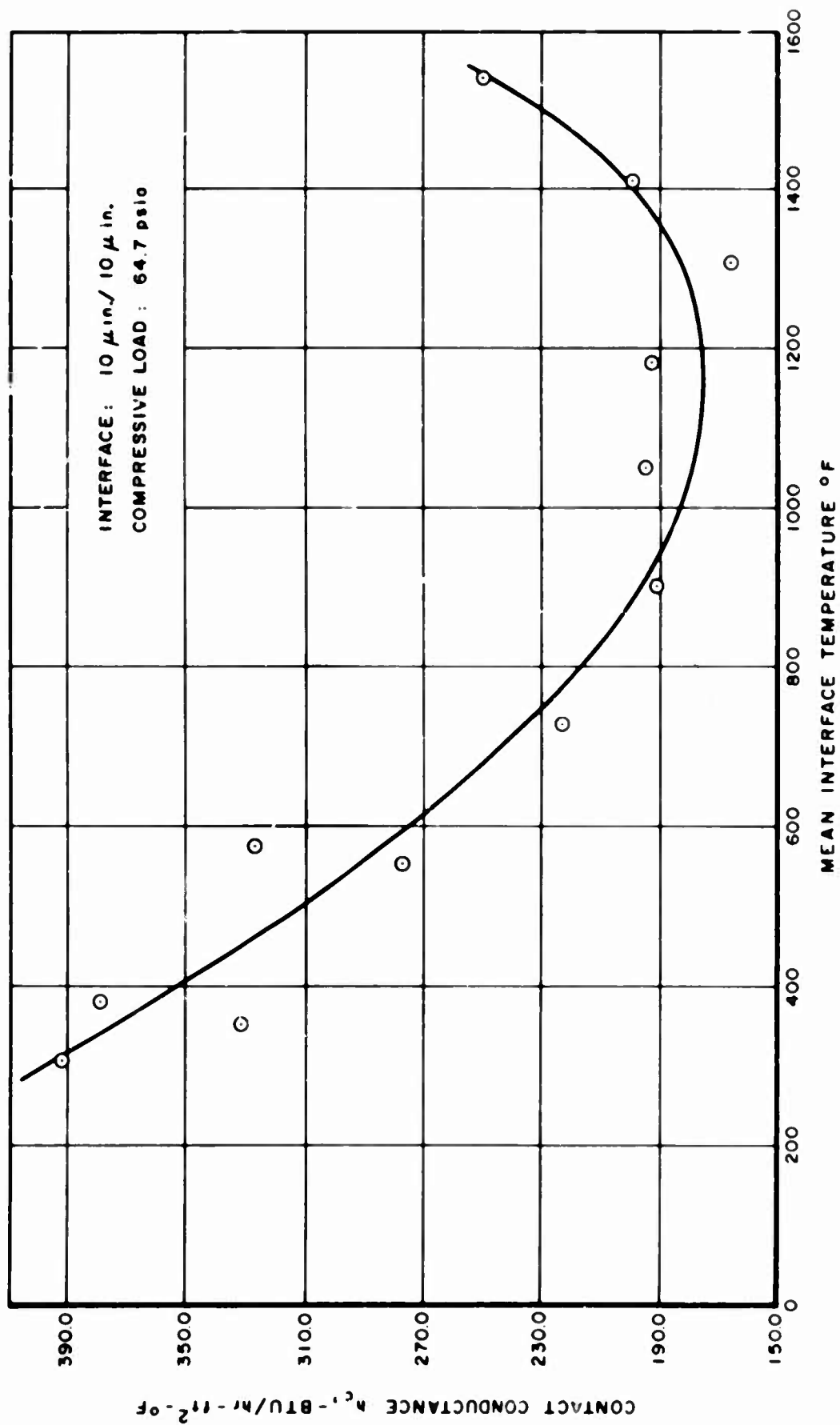


Figure 23. Contact Conductance as a Function of Interface Temperature:  
10  $\mu$ in./10  $\mu$ in. Interface, 64.7 psia Compressive Load



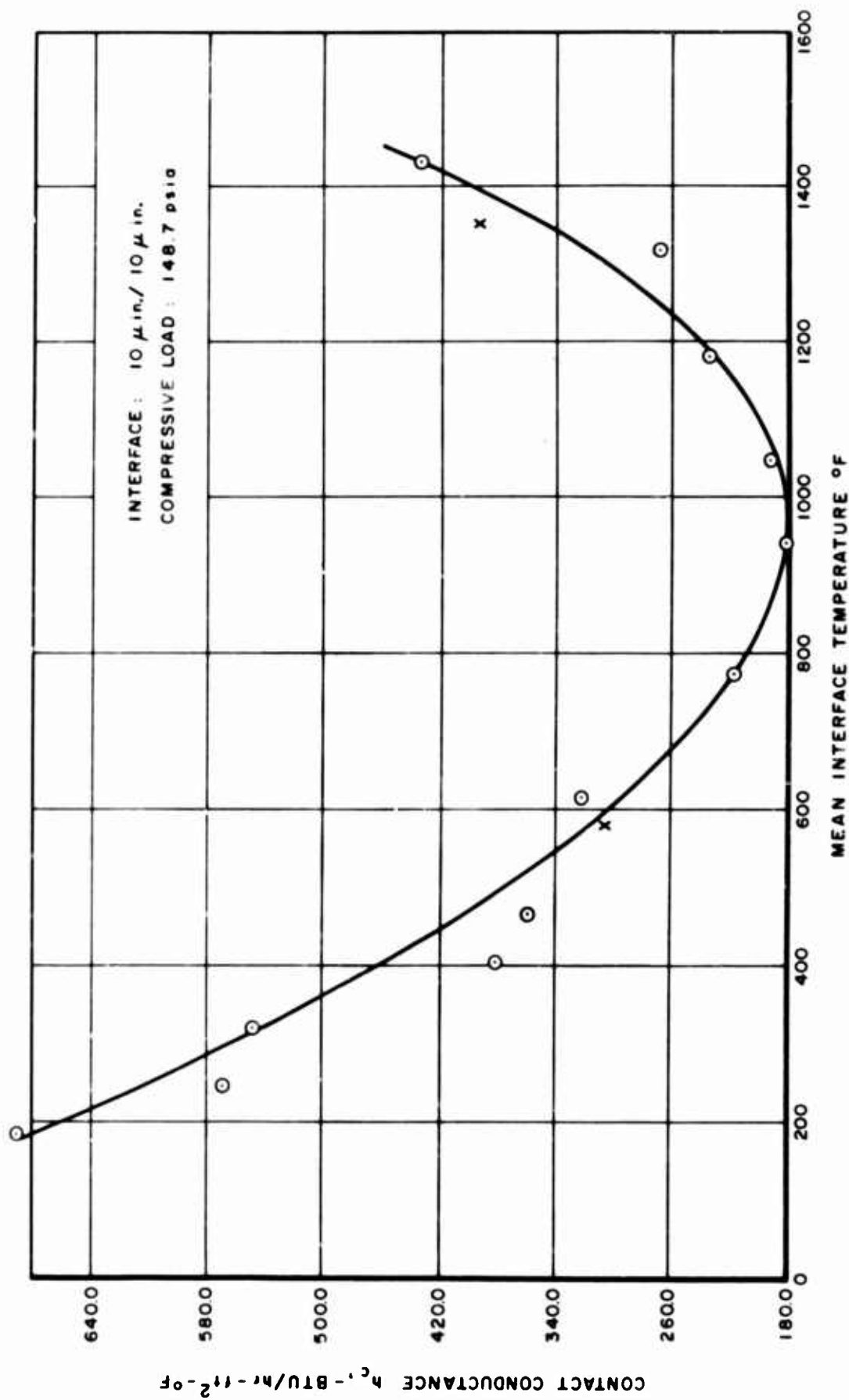


Figure 24. Contact Conductance as a Function of Interface Temperature:  
10  $\mu$  in./10  $\mu$  in. Interface, 148.7 psia Compressive Load

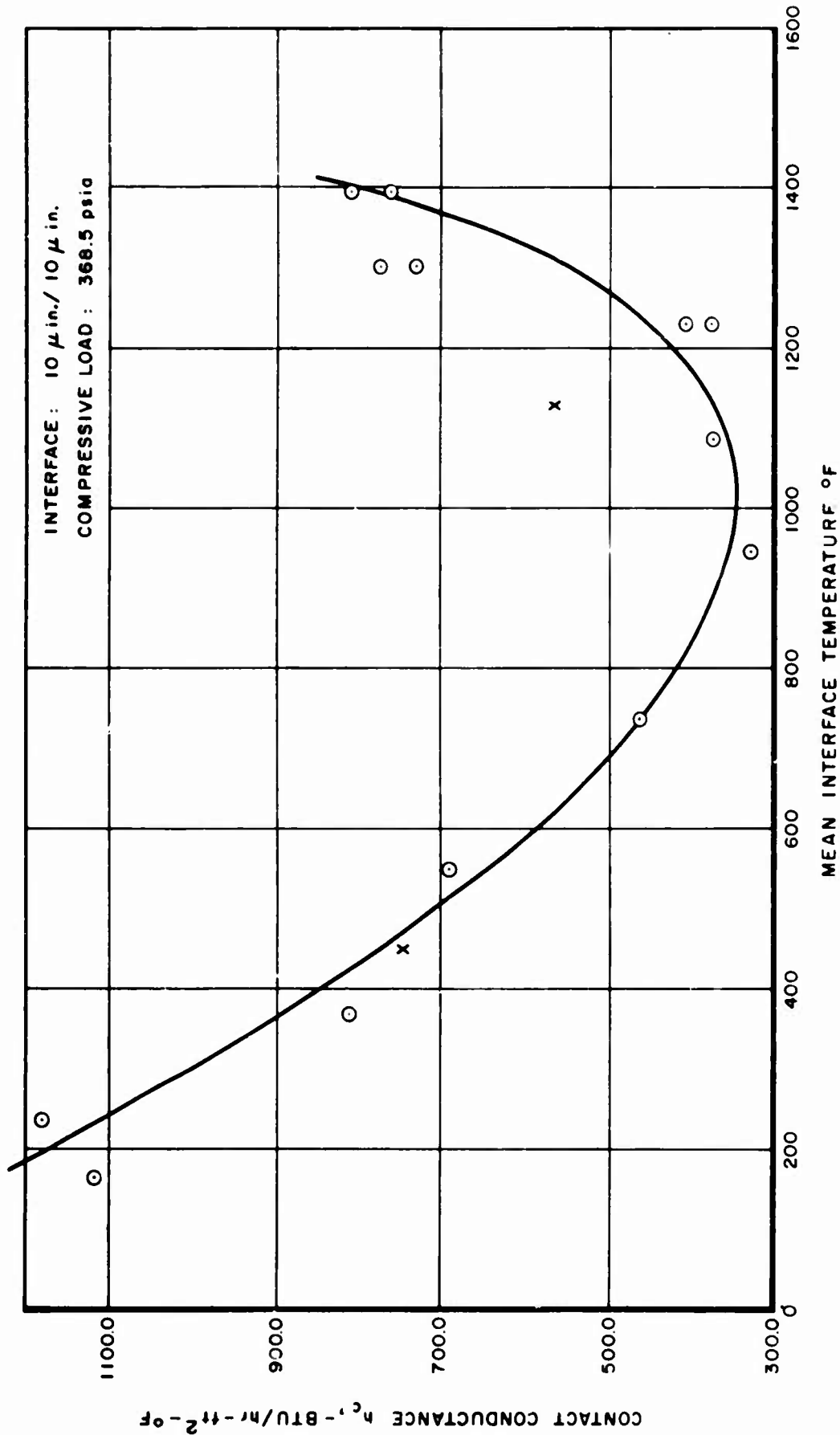


Figure 25. Contact Conductance as a Function of Interface Temperature:  
10  $\mu$ in./10  $\mu$ in. Interface, 368.5 psia Compressive Load

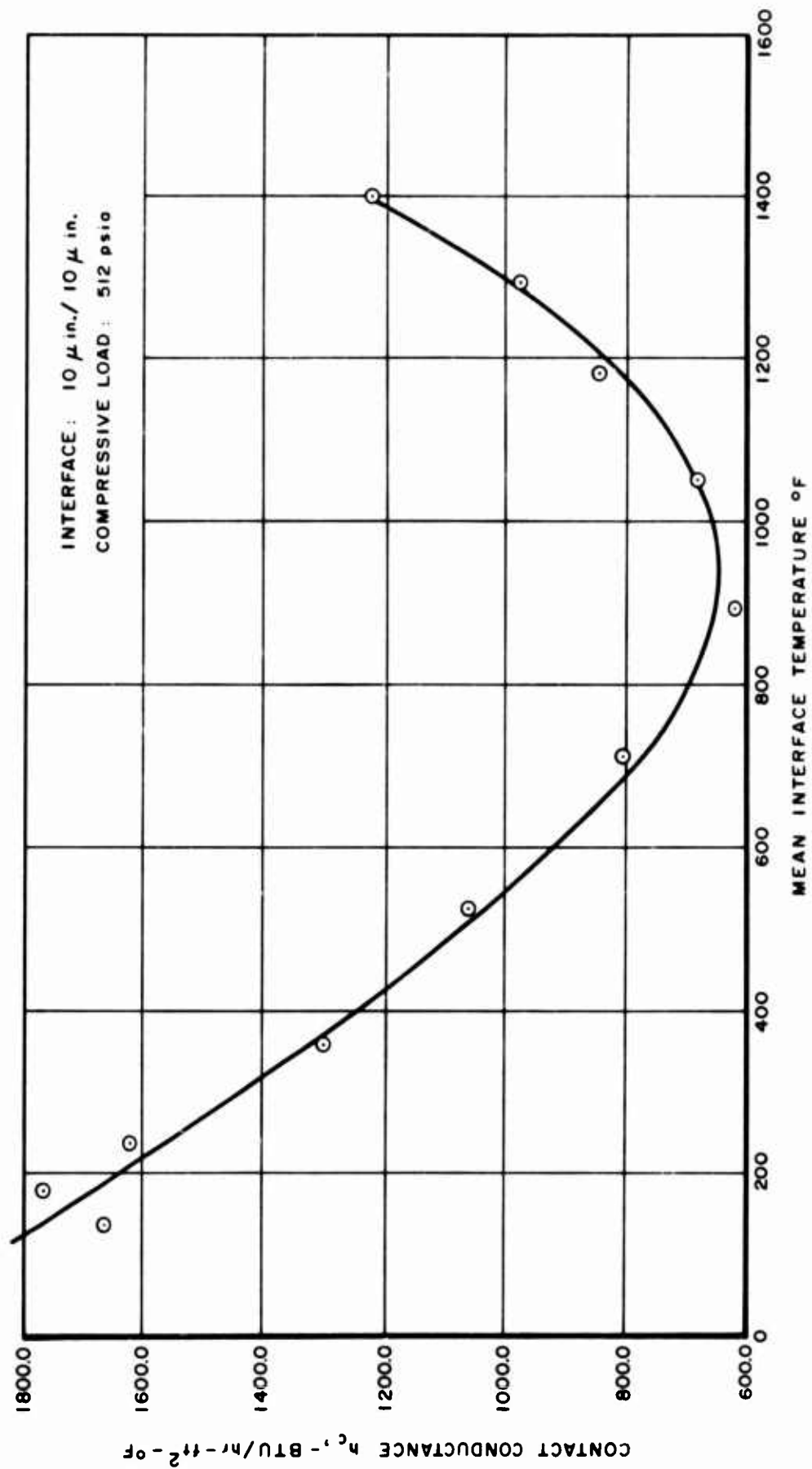


Figure 26. Contact Conductance as a Function of Interface Temperature:  
10  $\mu$  in./10  $\mu$  in. Interface, 512.0 psia Compressive Load

The data points given as "X's" in Figures 18, 24, and 25 are cooling curve results. These points indicate that there is no significant difference in conductance values on cooling from the high temperature exposure.

Consider now the general shape of the curves in these ten figures; it would be expected that, if the heat were transferred across the interface only at the actual solid-solid contact areas, the contact conductance would exhibit the same temperature dependence as the beryllium oxide thermal conductivity, that is, a decrease in contact conductance following a  $1/T$  dependency. All the  $h_c$  versus  $T$  curves exhibit this characteristic at low temperatures. In all cases, however, the  $h_c$  values deviate in a positive sense from this dependency as the temperature level increases. As noted in the previous section, the heat flux in the specimen column increases with mean interface temperature as does the interfacial temperature drop. Since the radiative heat transfer across the interfacial gap area varies as  $T_m^3 \Delta T_c$  it would be expected that this heat transfer mechanism becomes important at higher temperatures. Between 300 and 1600° F, which represents a threefold increase in absolute temperature, the interfacial temperature drop across the 40  $\mu$  in. / 40  $\mu$  in. contact increases by a factor of between 4.5 and 7, depending on the compressive load. The magnitude of the radiative contribution thus increases by a factor of 20 or more. The situation is similar for the 10  $\mu$  in. / 10  $\mu$  in. case, the interfacial temperature drop increasing by a factor of between 6 and 7 over the same temperature interval.

The net result is a predominance of the radiative contribution at high temperatures which determines the shape of the  $h_c$  versus  $T$  curve in this range. In most cases these curves shift to a positive temperature dependency; a quantitative assessment of this postulation is given in the next section.

Considering the shapes of the curves giving the 40  $\mu$  in. / 40  $\mu$  in. results, Figures 17-21, the general influence of the compressive load on the relative contributions of conductive and radiative transport across the interface region can be inferred. As the load level increases, it is clear that the magnitude of solid conductance contribution is increasing rapidly; the magnitude of the low temperature  $h_c$  values verifies this observation. The radiative contribution, on the other hand, is not directly affected by the compressive load. Because the solid conduction contribution is comparatively large at the higher loads the interfacial temperature drops are lower and the radiative contributions to the effective contact conductance are consequently lower. Thus, as seen in Figures 20 and 21 which give the higher load data for the 40  $\mu$  in. / 40  $\mu$  in. interface, the upturn in the  $h_c$  curves noted

at lower loads has been eliminated. In effect the increased solid conduction prevents the generation of large  $\Delta T_c$  values and the radiative contributions are consequently reduced.

To obtain an experimental estimate of the effective gap width across the contact region, additional contact conductance tests were run in argon. The results for the 40  $\mu$  in. / 40  $\mu$  in. and the 10  $\mu$  in. / 10  $\mu$  in. interfaces are given in Figures 27 and 28, respectively. By comparing the vacuum environment thermal contact conductance values with the contact conductance measurements made in argon at the same compressive load and temperature level, the contribution of gas phase conduction to the total heat transfer across the gap can be calculated. Knowing this value, the effective gap width can be determined according to Equation 25,

$$\delta = \frac{k_{\text{argon}}}{(h_c)_{\text{argon}} - (h_c)_{\text{vacuum}}} \quad (25)$$

These data were obtained at a temperature low enough to minimize radiation transport across the gap. The values of  $\delta$  calculated in the above manner were used as a check of the effective gap width calculated independently from the surface roughness-waviness profile data. These results are discussed in the next section.

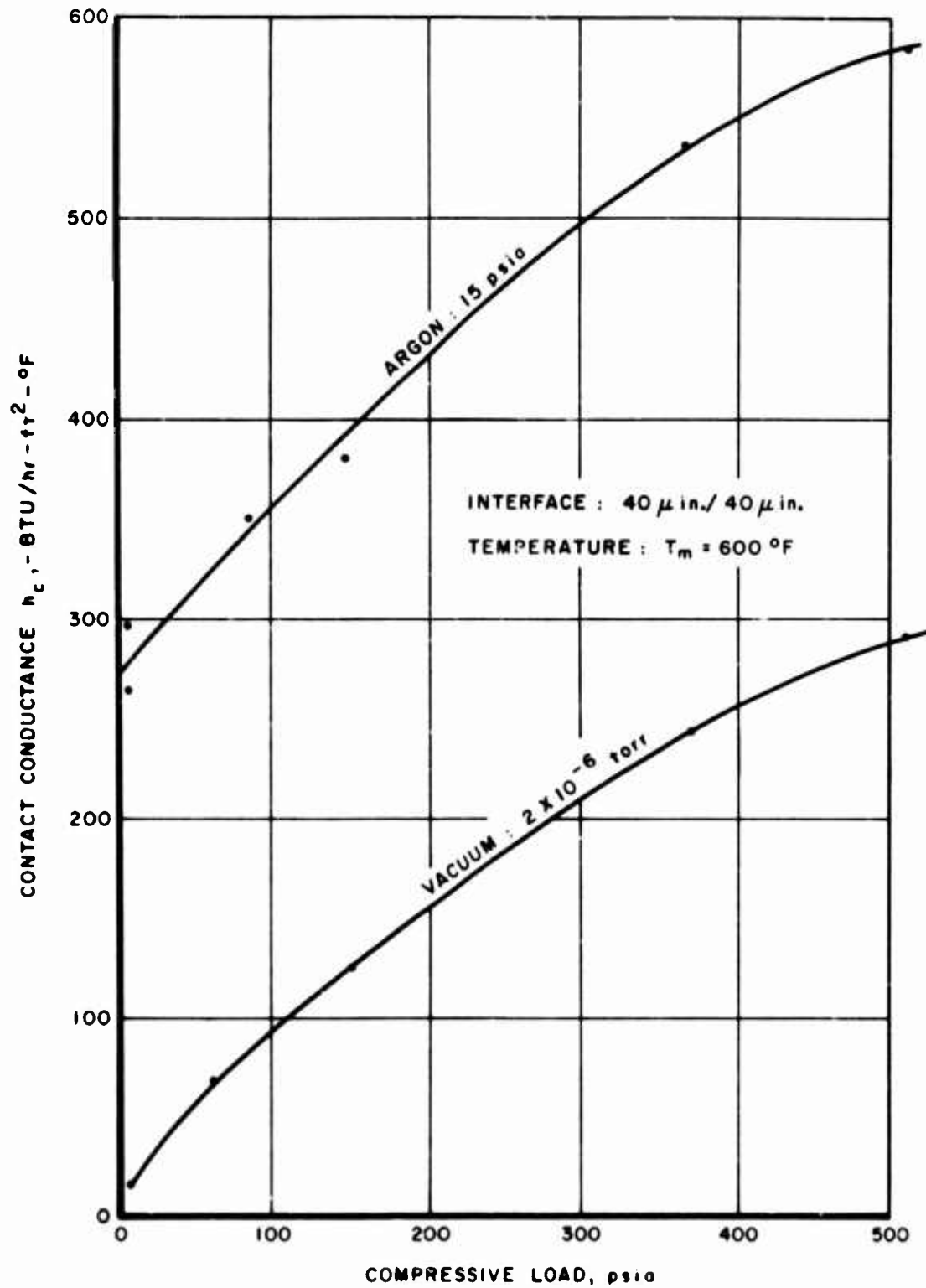


Figure 27. Vacuum and Inert Gas Environment Contact Resistance Results:  $40 \mu\text{in.}/40 \mu\text{in.}$  Interface

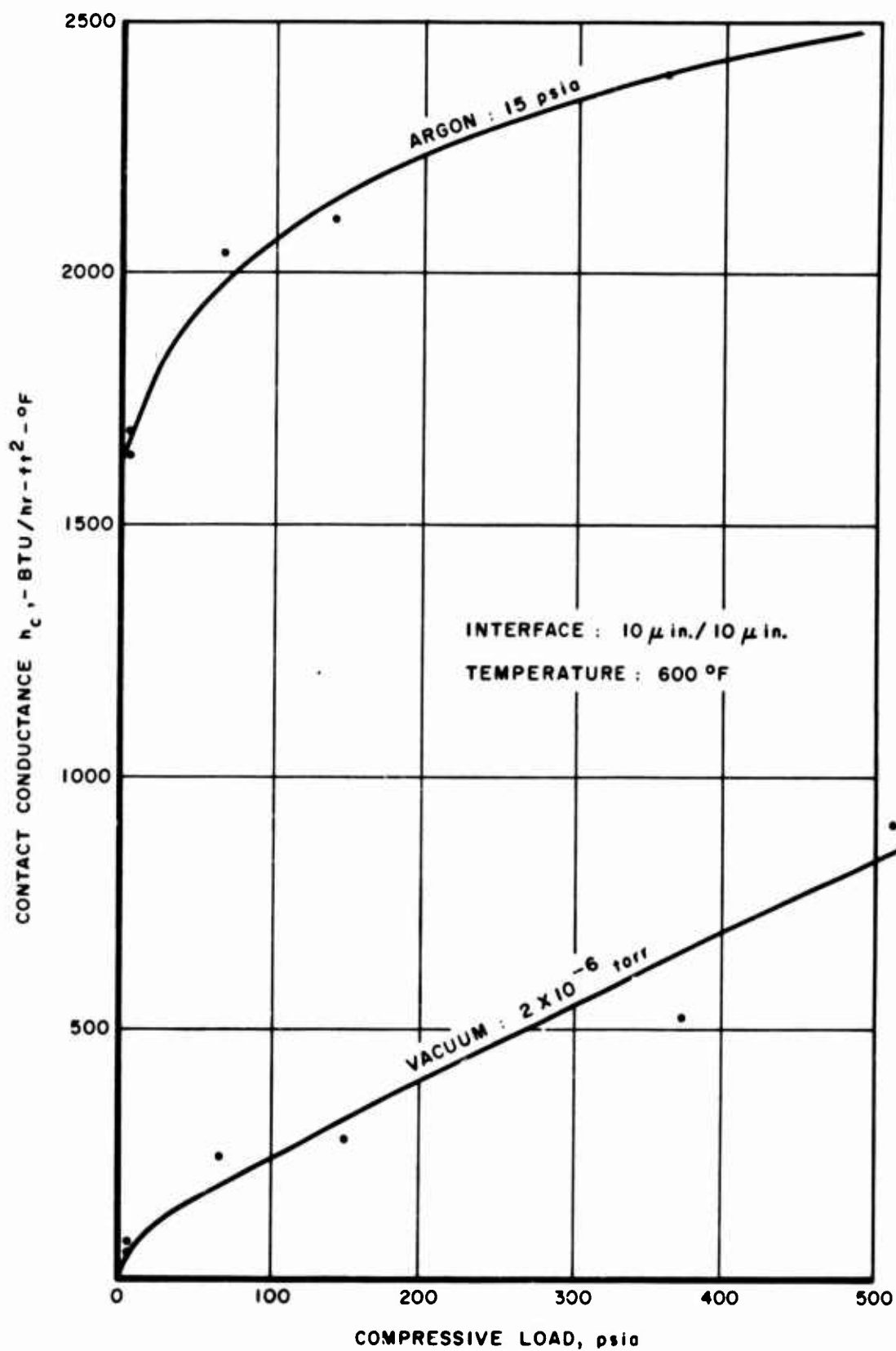


Figure 28. Vacuum and Inert Gas Environment Contact Resistance Results:  
10  $\mu$ in./10  $\mu$ in. Interface

## SECTION IV

### DISCUSSION OF RESULTS

#### A. FORMULATION OF THE CONTACT MODEL

##### 1. General Contact Characteristics

The temperature discontinuity observed across an interface transferring heat results from the imperfect nature of contact, as shown schematically in Figure 29 (Reference 1).

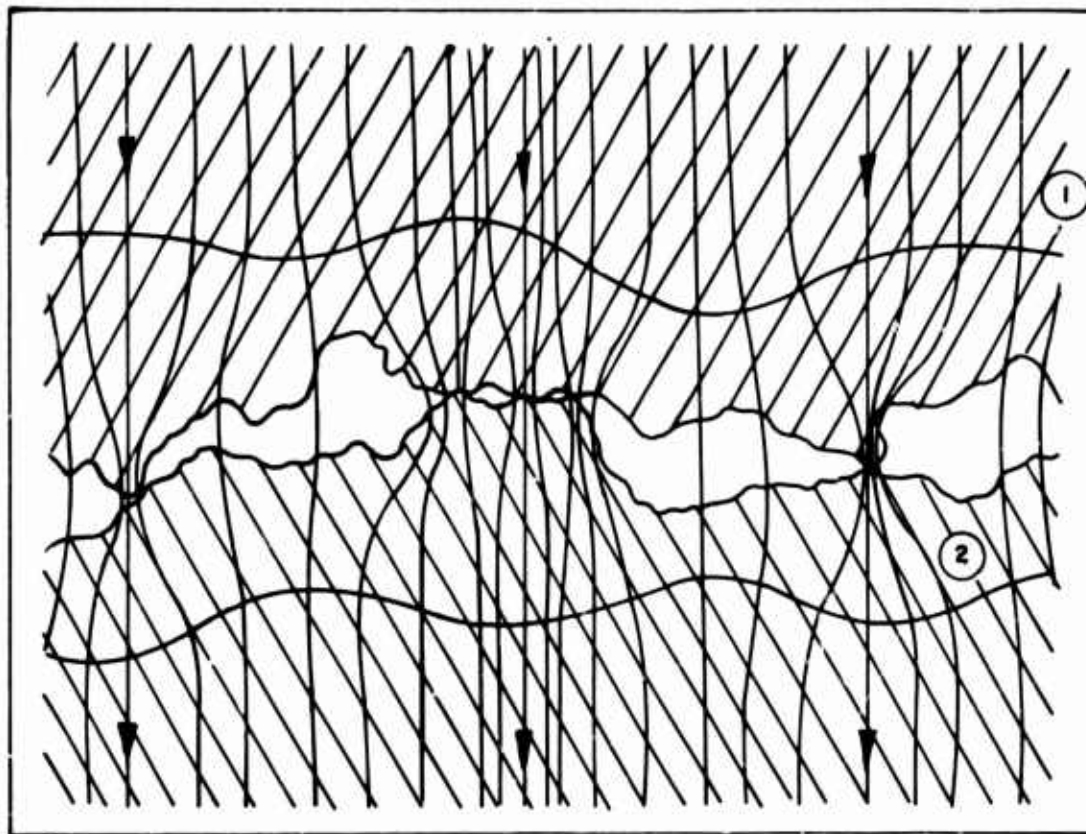


Figure 29. Flux Field Distribution at an Interface



As the interface is approached the flux lines tend to converge to the direct solid-to-solid contact points, since this flow path generally offers considerably less resistance to heat transfer than the surrounding void areas. This situation would be altered, of course, if the void areas contained a gas which had a high conductivity or if the temperature level were so high that significant radiative transport developed across these gap areas.

The convergence of the flux lines to the solid-solid contact areas produces a "constriction resistance" and an interfacial temperature drop to compensate for it. This can be noted in Figure 29 where the equipotential (isothermal) surfaces ① and ②, which are orthogonal to the flux field, are seen to curve away from the contact plane at the constriction points.

Early investigations in this field either neglected surface characterization definition or lumped the effects of surface finish on interfacial heat transfer into an effective surface roughness, usually expressed in a simple RMS or CLA value. Beginning in 1957-1958 (e.g., References 20 and 21), as the results of surface finish analyses were applied to studies of interfacial heat transfer, it became apparent that such a simple surface characterization procedure was entirely inadequate in correlating heat transfer across real surfaces in contact. Not only is microscopic roughness, resulting from conventional forming and finishing operations, present but also roughness on a larger wavelength scale such as surface waviness or, in the extremes, surface curvature (Reference 1). If an interface is made up of surfaces which are both rough and wavy, relatively large contact regions governed by the waviness will be formed. Each of these areas will consist of a number of smaller solid-to-solid contact points, the size and distribution of which are governed by the surface roughness. In Figure 29, the central contact region illustrates this characteristic, since it is not only formed as a result of the contact of undulations of larger scale but consists also of many smaller individual contacts.

As a result of extensive surface characterization studies described briefly in Section III. A., the beryllium oxide specimens used in this investigation were found to be both rough and wavy. The waviness patterns were in the form of concentric rings; the roughness pattern was of random lay, as expected from the finishing procedure, and consisted of individual asperities.

The treatments of roughness and waviness contributions to the net contact resistance are given in the next two sections. Following this is the presentation of the combined model used in correlating the experimental contact resistance data obtained in this investigation.

## 2. Surface Roughness

It is usually assumed that the surface roughness of the contacting specimens is such that a group of point contacts with approximately circular cross section are formed when the specimens are brought together. With this approximation it is then necessary to develop an expression for the constriction resistance of a single circular cross-sectional contact as a function of the contact area radius. Since this relationship is known and the contact points are all in parallel, the total resistance of the group of contacts is found simply by summing reciprocals of each individual resistance. The individual contact points are generally assumed to have the geometry shown on the left in Figure 30. The contact area radius is  $a$ , the average gap width is  $\delta$ , and the radius of the element delivering heat to the solid-solid contact is  $b$ . An expression for the constriction resistance of this geometry with no flow across the gap area was worked out many years ago by Kottler (Reference 22) for the equivalent electrical case. Many derivations, producing essentially the same result, both exact and numerical, have been given for the heat transfer case as discussed in Reference 1. The briefest and most direct solution was given by Clark and Powell (Reference 23), who considered the case of steady-state heat transfer as being a gap between two semi-infinite regions (1 and 2) joined by a circular contact region of radius  $a$ .

The Laplace equation,  $\nabla^2 T = 0$ , in axisymmetric cylindrical coordinate form was written for each region with the following coupling boundary conditions along the contact plane.

$$\begin{aligned} z = 0, \quad r > a; \quad \frac{\partial T_1}{\partial z} = 0, \quad \frac{\partial T_2}{\partial z} = 0 \\ z = 0, \quad r < a; \quad T_1 = T_2, \quad \frac{\partial T_1}{\partial z} = \frac{\partial T_2}{\partial z} \quad (k_1 = k_2) \end{aligned}$$

The solution by "Hankel transformation" for region 1 is given in Equation 26, where evaluation of the integration constants has been completed under the above boundary conditions.

$$T_1 = (T_1)_\infty - \frac{(T_1)_\infty}{\pi} \int_0^\infty e^{-\nu z} \sin(\nu a) J_0(\nu r) \frac{\partial \nu}{\nu} \quad (26)$$

A sketch of this temperature field and the orthogonal heat flux paths is given at the right in Figure 30. The constant temperature surface at the distance from the interface where the temperature field is no longer distorted due to the constriction is represented by  $T_1 = (T_1)_\infty$ . If  $k_1 = k_2$ , the temperature distribution on either side of the interface is symmetrical, as depicted in Figure 30. The quantity of heat flowing from one region to the other is given by Equation 27, using the relationship expressed by Equation 26, so that

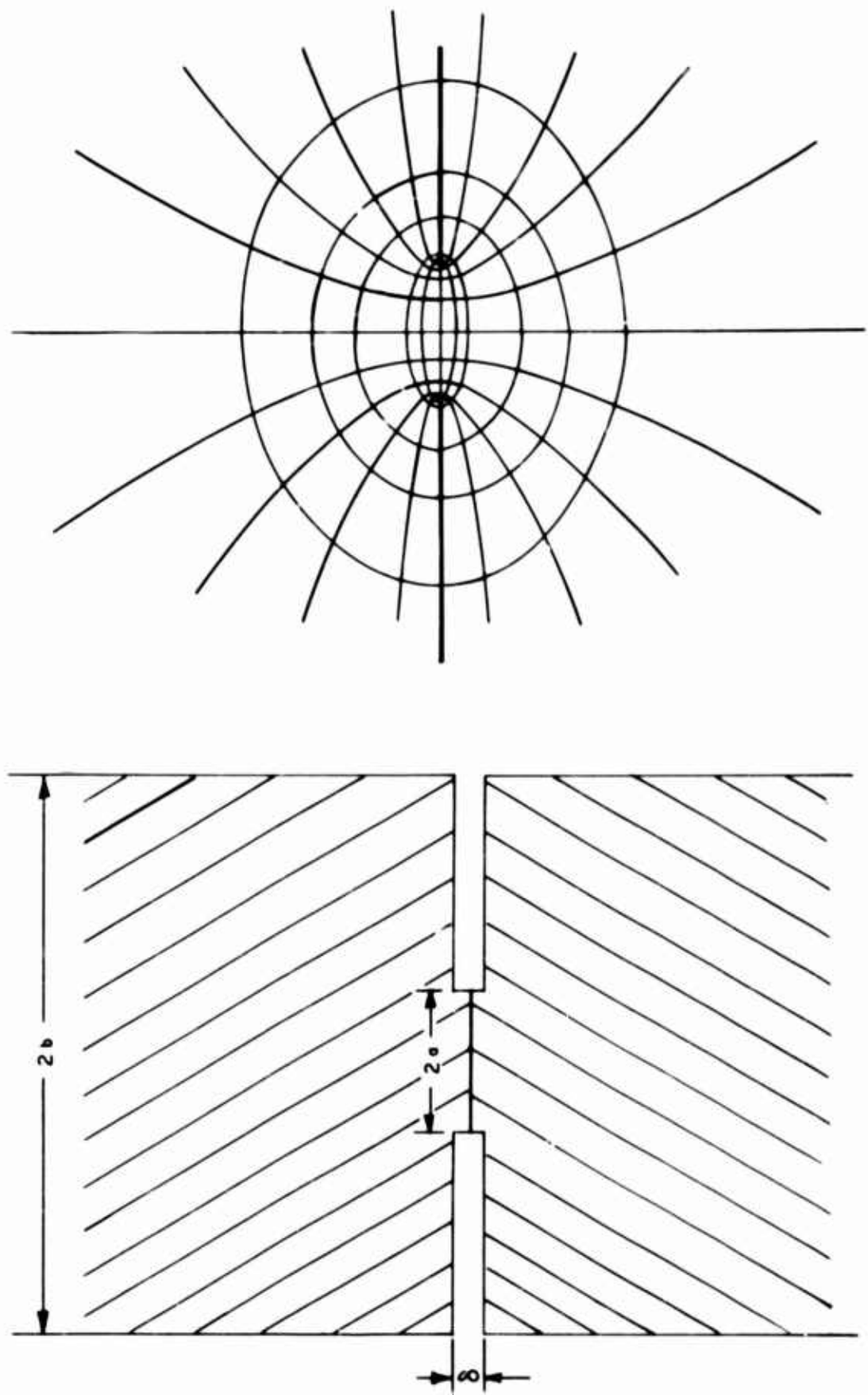


Figure 30. Idealized Contact Element and Associated Heat Flux - Temperature Field

$$Q \left( \frac{\text{BTU}}{\text{hr}} \right) = 2 \pi k_1 \int_0^a r \left( \frac{\partial T_1}{\partial z} \right)_{z=0} dr = 2 k_1 (T_1)_{z=0} a \quad (27)$$

The constriction resistance is then defined as,

$$R_c = \frac{(T_1)_{z=0}}{Q} = \frac{1}{2 k_1 a} \quad (28)$$

Equation 28 is the fundamental relationship for the thermal resistance induced in a conducting element by a coaxial region of reduced cross-sectional area where there is no heat transfer across the gap area.

The diameter of the "feeder" element,  $b$ , does not appear (Equation 28). This would be expected as long as  $b$  is somewhat greater than  $a$  since it is the constriction area of radius  $a$  which predominates in producing the temperature field distortion. The situation where  $a$  approaches  $b$  has been studied by Roess (Reference 24) and Clausing and Chao (Reference 25). The result is the application of a constriction alleviation factor  $g(\beta)$  to correct Equation 28 as follows,

$$R_c = \frac{g(\beta)}{2 k_1 a} \quad (29)$$

where

$$\beta = \frac{b}{a}$$

$$g(\beta) = 1 - 1.40925\beta + 0.29591\beta^3 - + \dots$$

Equation 29 was employed in calculating the surface roughness contributions to the total interfacial contact resistance using experimentally measured thermal conductivities for the beryllium oxide,  $k_1$ , and values of  $a$  and  $\beta = b/a$  obtained from analysis of the surface roughness traces.

### 3. Surface Waviness

The configurations of the contact areas between the beryllium oxide specimens produced by the surface waviness were in the form of concentric rings. The contact ring area and the cross section shown is in two-dimensional Cartesian coordinates. The contact parameters  $a$ ,  $b$ , and  $\delta$  were determined from analysis of the surface waviness profiles.

The simple analysis of the previous section is not applicable in treating surface waviness contributions to the total contact conductance because heat transport across the gap area ( $a \leq r \leq b$ ) by radiation is likely to be important at higher temperatures, as discussed qualitatively in Section III. C. Radiation contributions were neglected in the case of the roughness contact resistance calculation for two reasons:

- (1) The temperature field distortions caused by the waviness patterns result in low temperature drops in the region of the roughness contacts, while the temperature drops across the gap regions between waviness contact areas are relatively high.
- (2) The percentage of the total interfacial regions occupied by roughness contacts is very small and thus the radiating surface area is small. The total radiation contribution is, of course, proportional to the product of these two factors.

To ensure a significant degree of flexibility in handling the potentially nonlinear effects of radiative transport in the gap regions between waviness contact areas, the temperature field in the contact element was determined numerically by the finite difference solution.

If a symmetrical conducting element has a constriction region, the centerline of the element becomes a line of symmetry. If it is also assumed that the temperature field is symmetrical with respect to the constriction plane, which is valid when  $k_1 = k_2$ , then study of the temperature field in the element can be confined to a quadrant region such as that sketched in Figure 31; heat flux paths are indicated.

After the steady-state temperature field in the region is determined with the boundary conditions observed experimentally, the effective contact conductance can be inferred from the extent of distortion of the heat flux path. Radiation boundary conditions occur along the surface

$$a \leq r \leq b, \quad 0 \leq z \leq \frac{\delta}{2}$$

A typical finite element network is shown in Figure 32. In this Figure there are 72 nodal points, whereas the networks used in the beryllium oxide analysis averaged about 500 nodal points. All the different types of nodal points and their relative locations are shown in this figure, however. There are six types of nodal points including fixed temperatures along the surfaces I, J = 1 and 8.

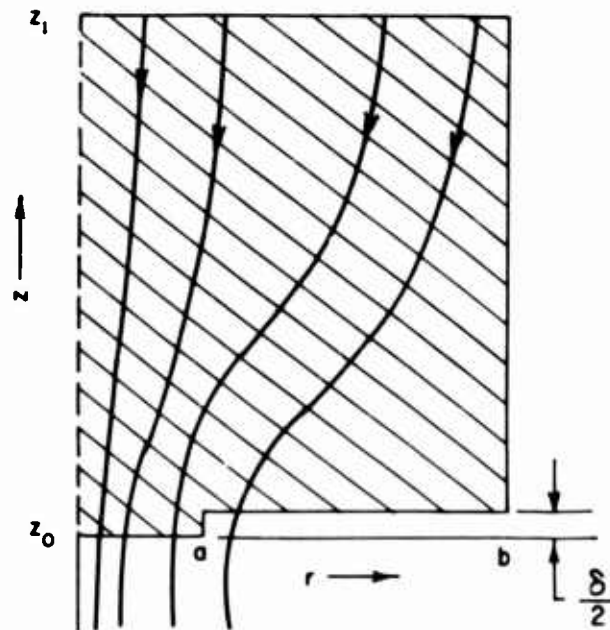


Figure 31. Contact Element Quadrant

Two approaches can be used in formulating the nodal equations (the results are identical). In one case, the finite difference form of the equation

$$\nabla^2 T = 0$$

can be employed, writing equations for the nodal temperatures in terms of the temperatures adjacent, such that the above equation is obeyed. In the other case, the heat fluxes into each node can be summed and nodal temperature equations derived based on the steady-state condition

$$q_{\text{net}} = 0$$

The latter approach was used here because it was convenient to express the radiation boundary conditions in terms of heat flux rather than temperature equations.

The derivations of these nodal equations are given in Appendix B. The results are given below in Table VI. The equations given here have been simplified from those derived in the Appendix by assuming that  $\Delta x = \Delta y = \ell$ , throughout the nodal network. The evaluation of the geometrical and emissivity shape factors in the heat transfer coefficient equation is discussed in the next section.

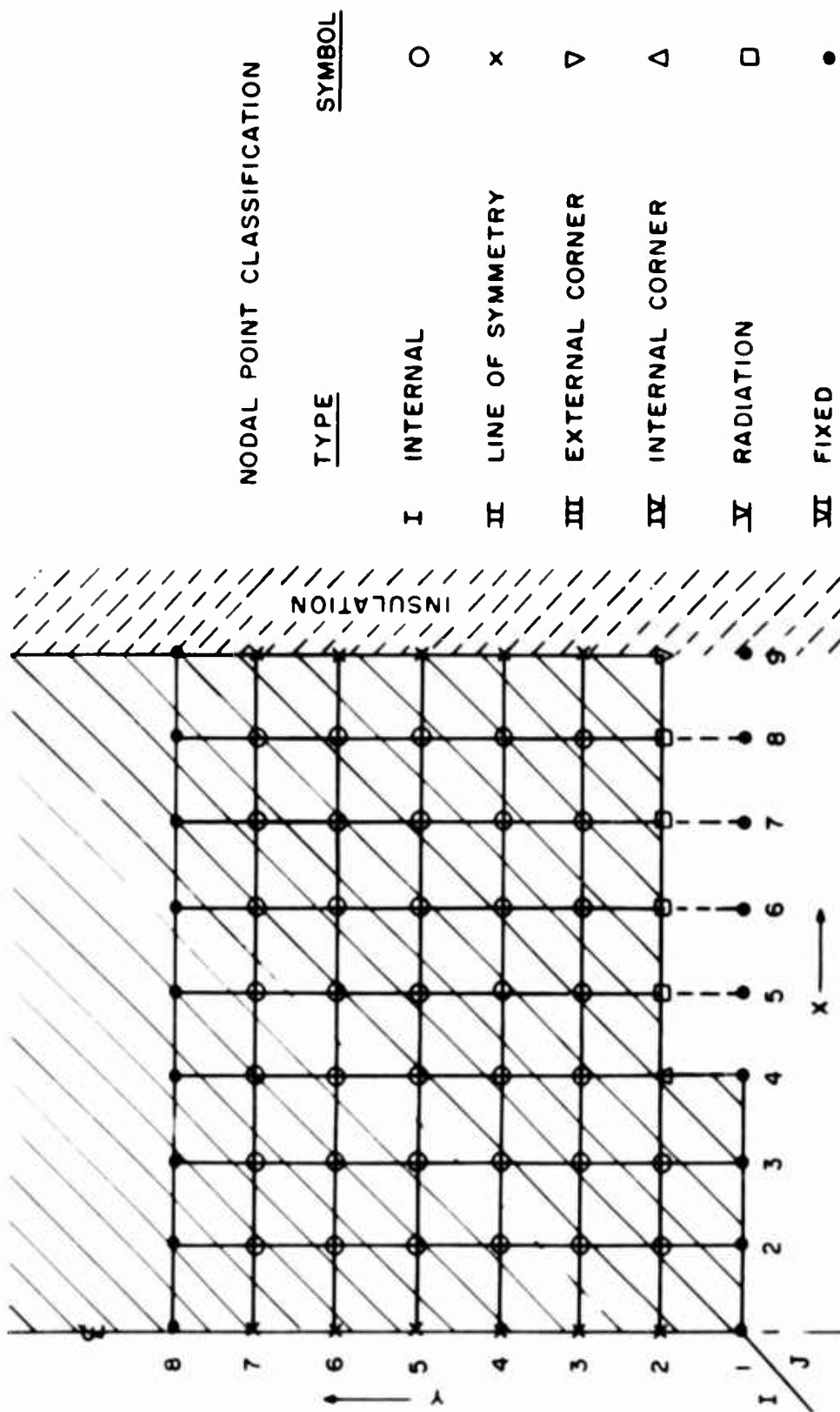


Figure 32. Finite Element Nodal Point Definitions

TABLE VI  
NODAL EQUATION SUMMARY

Type	Nodal Equation
Internal	$T(I, J) = \frac{1}{4} [T(I, J+1) + T(I, J-1) + T(I+1, J) + T(I-1, J)]$
Line of Symmetry { + = $\epsilon$ Boundary { - = Insulated	$T(I, J) = \frac{1}{4} [T(I, J+1) + T(I, J-1) + 2T(I \pm 1, J)]$
Internal Corner	$T(I, J) = \left\{ \frac{2[T(I-1, J) + T(I, J+1) + T(I+1, J) + T(I, J-1)] + \frac{h_R \ell}{k} T(I, J-1)}{(6 + \frac{h_R \ell}{k})} \right\}$
External Corner	$T(I, J) = \left\{ \frac{T(I-1, J) + T(I+1, J) + 2T(I, J+1) + \frac{2h_R \ell}{k} T(I, J-1)}{4 + (2 \frac{h_R \ell}{k})} \right\}$
Radiation	$T(I, J) = \left\{ \frac{T(I-1, J) + T(I+1, J) + 2T(I, J+1) + \frac{2h_R \ell}{k} T(I, J-1)}{(4 + \frac{2h_R \ell}{k})} \right\}$
Heat Transfer Coefficient	$h_R = \frac{q}{\Delta T} = \sqrt[4]{\epsilon_0 \epsilon_e} \sigma (T_i^3 + T_i^2 T_o + T_i T_o^2 + T_o^3)$



It is noted in the equations of Table VI that the parameter describing the influence of boundary radiative transport on the temperature field is the dimensionless group  $h_R \ell / k$ . This group, of Biot modulus form, gives the ratio of boundary radiative transport to in-depth thermal conduction:  $h_R / (k / \ell)$ . For a given overall temperature drop in the element, the magnitude of the temperature gradient is inversely proportional to  $\ell$ , hence this parameter is grouped in the conduction term  $(k / \ell)$ .

The method of evaluating the finite element equations consisted of assuming an initial temperature distribution, calculating new temperatures for each nodal point, and correcting the original temperature by a small percentage of the difference between the original and newly calculated temperature. This is basically a relaxation method with the use of a damping factor to ensure smooth convergence to the correct temperature field as repeated iterations of the full temperature distribution are performed. Convergence stability is a concern, of course, due to the nonlinear nature of the radiative boundary condition; the radiative heat transfer coefficient is a function of temperatures which vary from iteration to iteration. A program for the IBM 7094 computer was written to perform the iterative calculations. Depending on the number of nodal points used, convergence was achieved after 100 to 600 iterations of the entire network. Computer output consisted of the final temperature distribution and a plot of the nodal residuals throughout the network.

As an illustration of the procedure used in calculating the contact resistance using the finite element analysis, the results of two cases will be given in which the simple network depicted in Figure 32 will be used. In the first case the temperature along the surface I,  $J = 1$ , was assumed to be  $500^\circ \text{F}$ , while that along the surface I,  $J = 8$ , was assumed to be  $1500^\circ \text{F}$ . Other numerical information is given under "Numerical Evaluation" in Appendix II. Nodal residuals for the entire network were printed after 2, 10, 50, and 100 iterations. Maximum values of these residuals were 8.3, 3.2, 0.59, and 0.12% of the mean element temperature, respectively. The temperature field after 100 iterations is shown in Figure 33. The total heat flux flowing in the element is determined using Equation 30 and the temperature distribution away from the interface (e.g., the 1400 and 1500° F isotherms) is

$$q_{\text{total}} = k \sum_{I=1}^8 A_I \left( \frac{\Delta T}{\Delta Y} \right)_I \quad (30)$$

where  $\Delta T$  is  $100^\circ \text{F}$  in this case and  $\Delta Y$  is the distance between these two isotherms. The radiative heat transfer across the gap area was calculated similarly using Equation 31 and the temperature distribution along the gap surface.

$$q_{\text{radiation}} = \sum_{I=4}^{\infty} h_I (T_{I,J}) A_I \Delta T_I \quad (31)$$

The heat flow across the solid contact area is calculated as the difference between the above quantities or can be determined directly by using the temperature field data in the vicinity of the solid contact area along with an equation of the same form as Equation 30.

For this case only 3% of the heat flows across the radiation gap which produces the large distortion of the temperature field noted in Figure 33.

To test the stability of the relaxation iteration technique the influence of radiative heat transport in the gap was accentuated by arbitrarily increasing the constants in the equation for ( $h_{\text{Radiation}}$ ) by a factor of 1000. This artificially high effect of radiative transport produces the temperature field distribution shown in Figure 34. After 100 iterations the maximum nodal residuals in this case were on the order of 0.0001%. Thus, excellent stability is attained with the damping factor even in the presence of large radiation contributions. The form of the temperature field in Figure 34 indicates that heat is preferentially transferred across the gap region. Indeed, heat flux calculations using Equations 30 and 31 indicated that 65% of the heat flowing in the element was transferred across this region.

The Biot modulus,  $h_R \ell/k$ , for these two cases differ by a factor of greater than 400. For the temperature distribution given in Figure 33 the value was 0.011; for the distribution in Figure 34 the value was 4.66.

To calculate the thermal contact conductance from these temperature field distributions the following procedure was used. First, the temperature drop required to transfer the same amount of heat in an element with no discontinuity was calculated. For the distribution shown in Figure 33 the total heat flowing (with the constriction present) was 4,243 BTU/hr. The overall  $\Delta T$  as shown in the Figure was  $1500 - 500 = 1000^\circ \text{F}$ . The temperature drop required to transfer this amount of heat in this element with no constriction was  $668^\circ \text{F}$ . Thus, the temperature drop developed due to the presence of the contact was  $\Delta T_c = 1000 - 668 = 332^\circ \text{F}$ . Stated another way, the presence of the constriction causes displacement of the  $1168^\circ \text{F}$  isotherm ( $1500 - 332 = 1168^\circ \text{F}$ ), shown as the dashed curve in Figure 33, to the  $I, J = 8$  plane. This  $\Delta T_c$  divided by the heat flux crossing the solid and gap areas gives the thermal contact resistance of each region. The total contact conductance for the

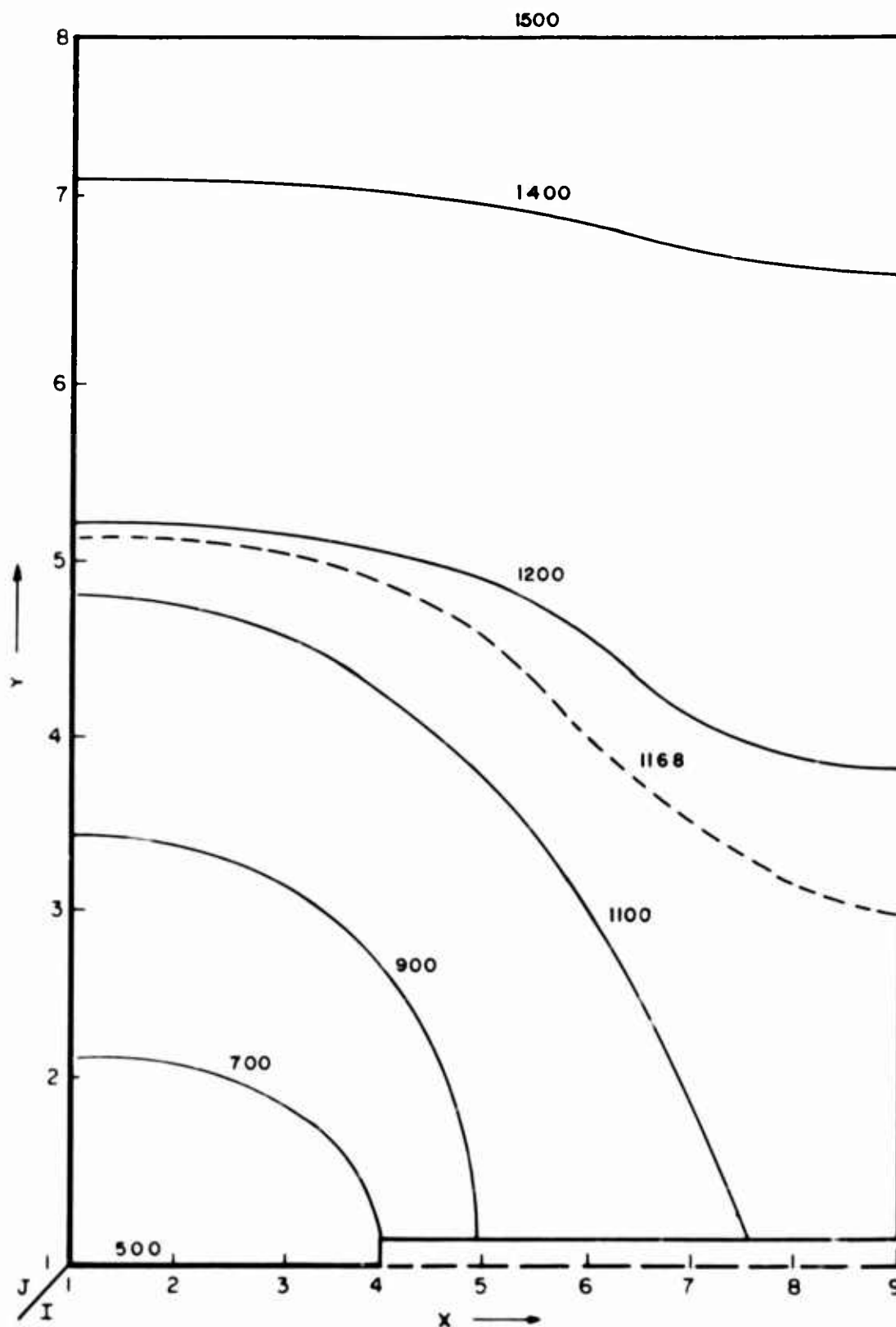


Figure 33. Isotherm Distribution in the Contact Element Quadrant with Normal Radiation Heat Transfer Coefficient

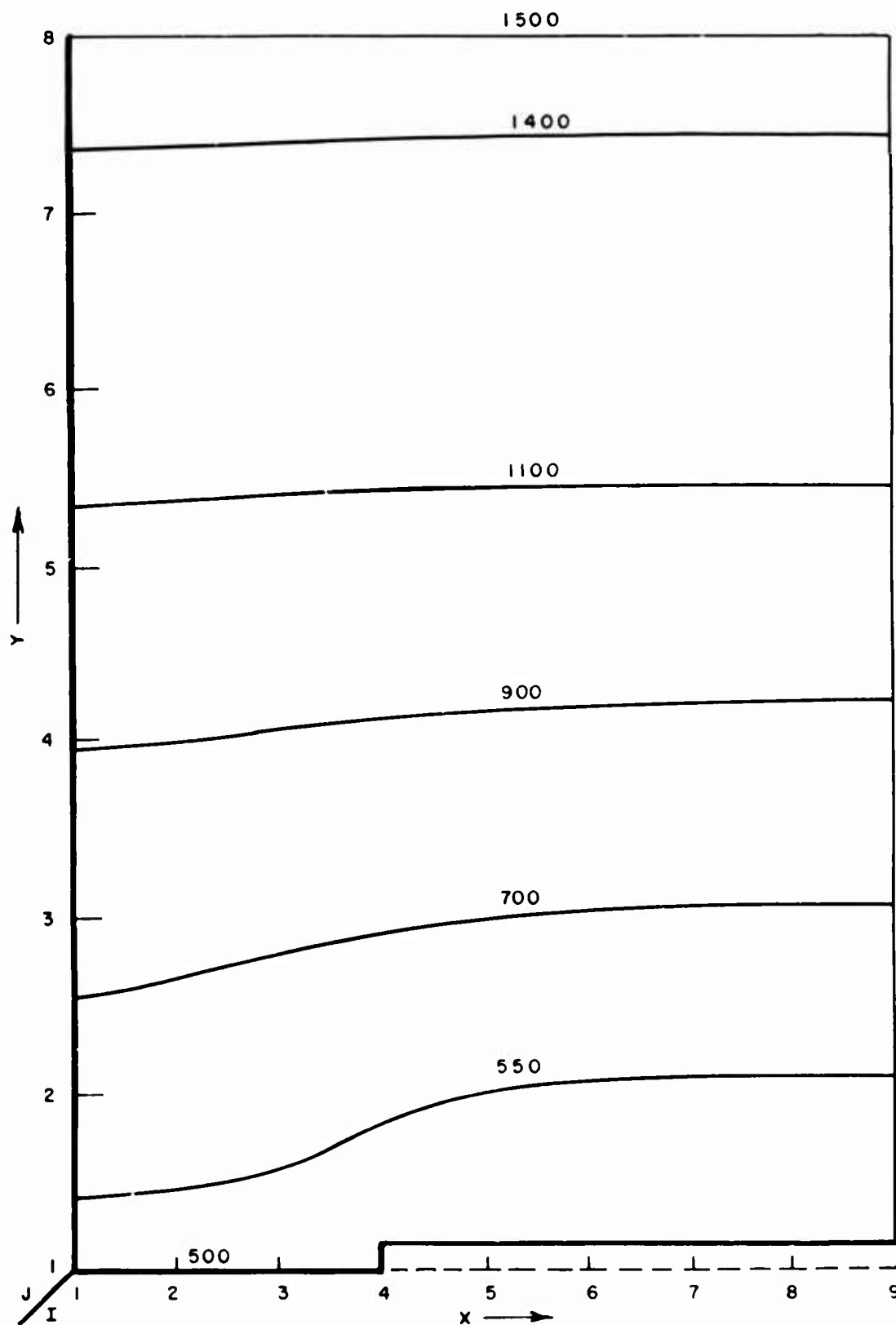


Figure 34. Isotherm Distribution in the Contact Element Quadrant with Increased Radiation Heat Transfer Coefficient

distribution given in Figure 33 was  $(h_c)_t = 150.93 \text{ BTU/hr-ft}^2\text{-}^\circ\text{F}$ . The value for the distribution in Figure 34 was  $(h)_t = -466.7$ . The negative quantity is expected since the artificially enhanced gap transport is a higher conduction region than the element material itself ( $h_R \ell / k > 1$ ).

The application of a finite element analysis to the constriction resistance problem has not been presented in the literature. Cetinkale and Fishenden (Reference 26) indicate that the Southwell relaxation method was used to obtain contact resistance values in a two-dimensional cylindrical contact element. Their analysis probably involved the use of an extensive grid network although the details are not discussed. These authors elaborated in much greater detail on the use of an exact analytical method of approximating the temperature field in the proximity of a constriction and the explicit formulation of contact resistance equations based on the model.

#### 4. The Combined Model

Analysis of the surface roughness and waviness profiles indicated that the beryllium oxide test surfaces exhibited significant degrees of both of these forms of surface irregularity. The interfacial heat transfer model included both of these effects. The first experimental evidence that more than the surface roughness contributed to the mean interfacial gap (of thickness  $\delta$ ) came from contact resistance measurements in argon. Equation 25 and the experimental results presented in Figures 27 and 28 for the 40 and 10  $\mu\text{in.}$  interface respectively were used to calculate an effective gap width. The average values were 119.6 and 756.3  $\mu\text{in.}$  for the 10 and 40  $\mu\text{in. CLA}$  interfaces, respectively. Where only surface roughness contributions are concerned, the effective gap widths calculated from the surface profiles were about 50  $\mu\text{in.}$  for the smoother interface and 100  $\mu\text{in.}$  for the rougher 40  $\mu\text{in.}$  interface. The disparity between these results suggested the presence of surface waviness patterns which would tend to increase considerably the effective  $\delta$ . Estimated waviness contributions are shown in Table VII along with the other results mentioned above.

The waviness contributions add another 60-70% to the effective  $\delta$  although the values still do not equal the estimates obtained from the contact resistance data in argon. The mean free path of the argon at the temperature and gas phase pressure of these tests was 5.39  $\mu\text{in.}$  the mechanism of gas phase conduction should then, be free of Knudsen transport regime effects. It would be expected that the accommodation coefficient between the relatively inert beryllium oxide and argon would be less than unity. The apparent increase in the effective gap width due to this characteristic has been discussed by Kennard (Reference 27) and by

TABLE VII  
EFFECTIVE GAP WIDTH COMPARISONS

Interface	$\delta$ , $\mu$ in.			
	Roughness Contribution per Specimen, $\delta_R$	Waviness Contribution per Specimen, $\delta_W$	Total ( $2\delta_R \pm 2\delta_W$ )	Measured in Argon using Equation 25
10 $\mu$ in.	25	15	80	119.6
40 $\mu$ in.	120	80	400	756.3

Rapier, Jones, and McIntosh (Reference 28). The apparent increase in the effective gap width due to accommodation coefficients less than unity is termed the accommodation jump distance,  $g$ , by these authors. It is proportional to the molecular mean free path and the quantity  $\{(2 - \mu)/\mu\}$  where  $\mu$  is the accommodation coefficient. The value of  $g$ , in microinches, which would add directly to the "Total" column in Table VII, ranged between 28.0 and 61.0 depending on the value of  $\mu$ ; values from 0.5 to 0.85 were considered.

These results along with the surface profile traces clearly indicate the importance of both roughness and waviness effects for the beryllium oxide surfaces studied here. The quantitative combined model used in generating analytically predicted curves of contact conductance as a function of temperature (and compressive load) is shown in Figure 35. The contact rings  $i$  and  $j$  produced by the waviness patterns each consist of a number of contact points produced by the roughness patterns. The thermal resistances induced by the waviness,  $(R_{W_I}, R_{W_{II}})_i$  and  $(R_{W_I}, R_{W_{II}})_j$ , are in series with those induced by the roughness,  $(R_{rgh_I}, R_{rgh_{II}})_i$  and  $(R_{rgh_I}, R_{rgh_{II}})_j$ , while the radiation gap resistances  $R_{Rad_I}$  and  $R_{Rad_{II}}$  are in parallel with both. The total thermal contact resistance of the network shown in Figure 35 is given by Equation 32.

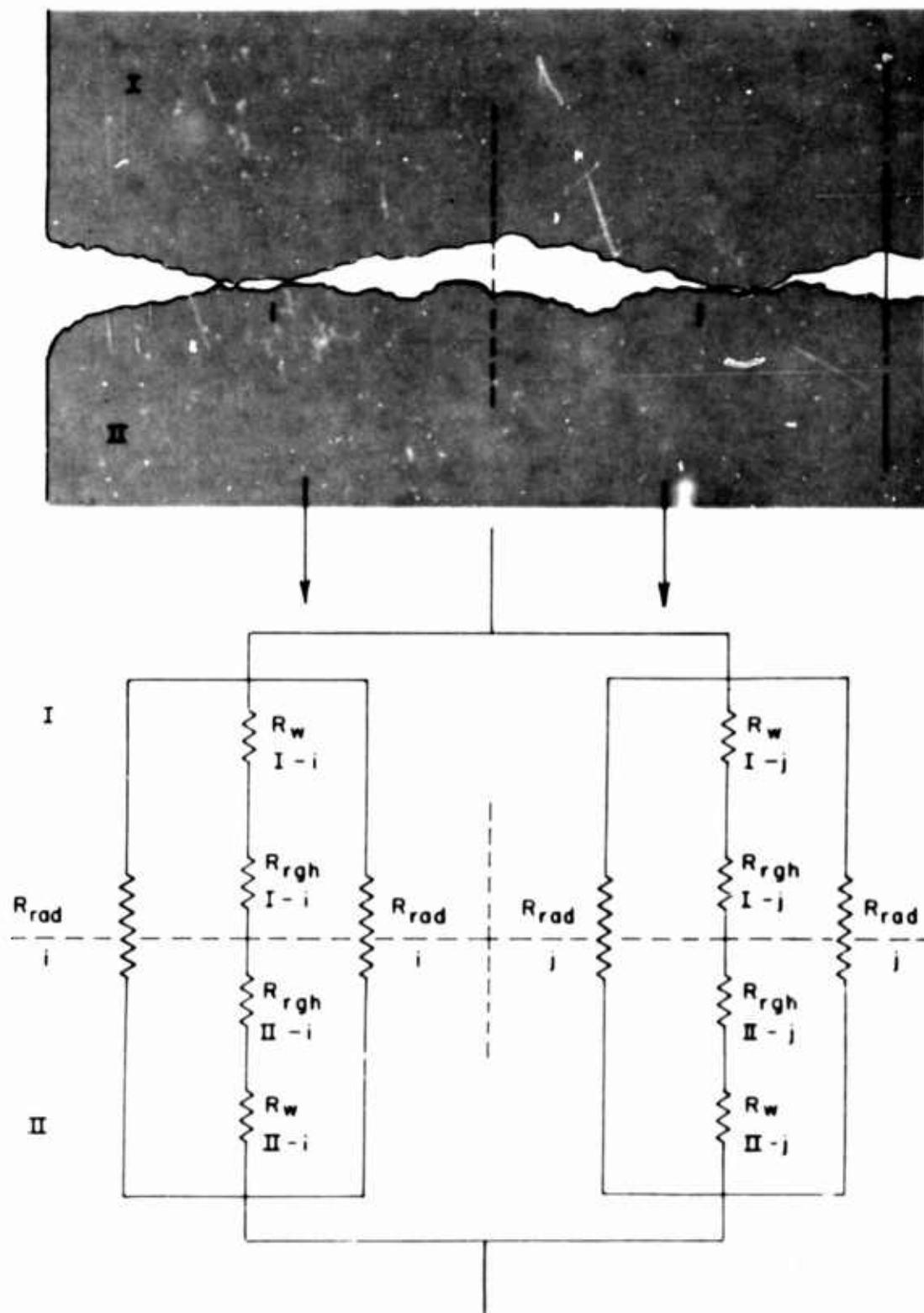


Figure 35. Combined Model Resistance Analog

$$(R_c)_T = \frac{\zeta \omega}{\omega \left[ \underset{\text{I}}{R_{Rad}} + \underset{\text{II}}{R_{Rad}} \right] + \left[ (\underset{\text{I}}{R_w} + \underset{\text{II}}{R_w} + \underset{\text{I}}{R_{rgh}} + \underset{\text{II}}{R_{rgh}})_i + (\underset{\text{I}}{R_w} + \underset{\text{II}}{R_w} + \underset{\text{I}}{R_{rgh}} + \underset{\text{II}}{R_{rgh}})_j \right]} \quad (32)$$

where

$$\zeta = \underset{i}{R_{Rad}} \underset{j}{R_{Rad}}$$

$$\omega = (\underset{\text{I}}{R_w} + \underset{\text{II}}{R_w} + \underset{\text{I}}{R_{rgh}} + \underset{\text{II}}{R_{rgh}})_i (\underset{\text{I}}{R_w} + \underset{\text{II}}{R_w} + \underset{\text{I}}{R_{rgh}} + \underset{\text{II}}{R_{rgh}})_j$$

The waviness and radiative thermal contact resistances  $R_w$  and  $R_{Rad}$  were determined by the methods outlined in Section III. The roughness thermal contact resistances,  $R_{rgh}$ , were calculated using the methods outlined in Section II. In Section V comparisons are made of these analytically predicted contact resistances with the experimentally measured contact resistance versus mean interface temperature results.

## B. COMPARISON OF ANALYTICALLY PREDICTED RESULTS WITH EXPERIMENTAL MEASUREMENTS

To generate an analytically predicted  $(h_c)_t$  versus mean interface temperature ( $T_m$ ) curve, three types of input data are required:

- a. Surface geometry data (roughness and waviness)
- b. Temperature dependent physical property data (thermal conductivity, emittance, and compressive strength) for the beryllium oxide.
- c. Gross temperature distribution data:  $T_m$  and an estimate of the range of temperatures found in the vicinity of the contact for a given  $T_m$ .

### 1. Input Parameters

Analysis of the surface profile data produced the set of geometrical parameters for the  $10\mu$  and  $40\mu$  in surfaces summarized in Table VII.

The thermal conductivity data used was measured on the test specimens and reported in Figure 10. The compressive strength data for BeO in the density and purity range used here was taken from the recent ceramic materials compendium issued by



TABLE VIII  
SURFACE GEOMETRY PARAMETERS

Waviness										Roughness	
Inner Ring					Outer Ring					Number of peaks	Average Radius $\mu$ in.
Mean Diam. in.	Ring Width in.	Gap Thickness $\delta/2$ , $\mu$ in.	Gap Width in.	Mean Diam. in.	Ring Width in.	Gap Thickness $\delta/2$ , $\mu$ in.	Gap Width in.				
10 $\mu$ in.											
0.346	0.0313	10.7	0.0814	0.762	0.0260	10.7	0.1068	30	1370		
40 $\mu$ in.											
0.0564	0.0147	53.3	0.0214	0.7464	0.0175	53.3	0.1562	11	882.0		

Battelle Memorial Institute (Reference 29). Emittance data on beryllium oxide was run during the course of this investigation on specimens in the same surface roughness range as the contact specimens. Spectral normal emittance was determined using a Perkin-Elmer spectrophotometer in accordance with the methods described in Reference 30. The numerical integration required in the conversion of this spectral data to the total hemispherical emittance values needed in the heat transfer calculation are discussed in Appendix III.

The radiative heat transfer coefficient given in Table VI requires evaluation of the geometrical and emittance shape factors,  $\mathcal{F}_0$  and  $\mathcal{F}_\epsilon$ , respectively. From Table VIII it is seen that the gap thickness to gap width ratio varies from  $1.0 \times 10^{-4}$  to  $2.7 \times 10^{-3}$ ; thus, the assumption that radiative transport occurs between infinite parallel planes is a good approximation (Reference 31). This leads to the conclusion that  $\mathcal{F}_0 = 1.0$  and that,

$$\mathcal{F}_\epsilon = \frac{1}{\frac{1}{\epsilon_1} + \frac{1}{\epsilon_2} - 1} \quad (33)$$

as long as the radiative transport is in the geometrical optics regime. The longest photon wavelength of interest in the Planck radiation distribution occurs at low interface temperatures and was on the order of  $10 \mu$  in. Thus, the assumption of geometrical optics, on which the derivation of Equation 33 is based, is valid.

Evaluation of Equation 33 is performed internally during the execution of the IBM 7094 finite element computer program using the varying radiation node temperatures and tabular  $\epsilon_{TH} = f(T)$  data in core storage to determine appropriate  $\epsilon_1$  and  $\epsilon_2$  values.

## 2. Analytically Developed Contact Conductances

The waviness pattern dimensions in Table VIII establish the basic geometry of the contact element to be analyzed in the finite element computer program. The spacing of the nodal points as determined by the parameter  $\mathcal{L}$  was chosen small enough to give numerous temperature points in regions of maximum temperature field distortion. The size of the nodal networks varied from  $20 \times 28$  for the  $10 \mu$  in. interface to  $20 \times 38$  for the  $40 \mu$  in. interface. Values of  $\mathcal{L}$  varied from 0.0039 to 0.0044 inches.

With the geometry of the network established, it was necessary to assign boundary temperatures along the fixed-temperature nodes. The relative position of these nodes is given in Figure 32. The assignment of these temperatures is not particularly critical at low

temperatures as long as the mean contact element temperature near the interface is approximately equal to  $T_m$ , the experimentally observed mean interface temperature. This is because the contact conductance is nearly heat flux independent at low temperatures; variation of the fixed-node temperatures at constant  $T_m$  changes only the net flux in the contact element. At high temperatures the contact conductance becomes temperature level and temperature gradient dependent due to the radiative contributions; thus, care is required in assigning boundary temperatures to produce  $T_m$  and temperature gradient values which correspond to those achieved experimentally.

To check the computer execution of the finite element program a hand calculation of one iteration for the entire network was performed. The nodal temperatures and the nodal residuals agreed exactly with those generated in the computer calculation. During the course of the successive iterations, selected nodal indexes, iteration indexes, nodal residuals, nodal temperatures, and heat transfer coefficients were printed out. This served as a check of calculation progression and allowed manual calculation of the heat transfer coefficients for comparison with computer-calculated values. In all cases agreement was exact. For the larger 20X30 node fields, convergence was fairly slow and, thus, printout of the complete nodal residual network was made to determine the number of iterations required. On the average, 600 iterations were sufficient to reduce the maximum residual to no more than 0.002% of the average temperature of the element.

To illustrate the application of the combined contact model, a set of  $(h_c)_T$  versus  $T$  curves for the 10 and 40  $\mu$  in. interfaces at a given load level were analytically generated for comparison with experimental measurements at the same load level. The low-load level curves for each interface, given in Figures 17 and 22 were chosen. In the case of the analytical prediction for the 40  $\mu$  in. interface, it was assumed that the contact area increased through brittle fracture at the peaks until the load of 3.94 lbs was supported. For the 10  $\mu$  in. interface it was assumed that the average load supported by the asperities was less by a factor of 6.2, the ratio of the contact areas versus displacement curves, for the two surfaces (Figure 16).

This assumption is based on the conclusion that very few of the 10  $\mu$  in. interface peaks undergo brittle fracture in supporting the fairly low 3.68 lbs load applied in this test. The surface roughness profiles (Figure 14) and the asperity geometry (Table VIII) for this interface indicate that the polishing employed produced contact areas with comparatively broad peaks. The results of the roughness and waviness contact resistance calculations are

summarized in Table IX. These values were employed in calculating the total interfacial contact resistance and its reciprocal, the total interfacial contact conductance  $(h_c)_T$ , using Equation 32. The values were based on total heat transferred,  $Q = \text{BTU/hr}$ , rather than on heat flux,  $q = \text{BTU/hr-ft}^2$ . After completion of the calculations the values were converted to a flux per unit area basis. In Table IX there is a consistent trend of increasing roughness and waviness contact resistance values as the temperature increases. This is due mainly to the decreasing thermal conductivity of the beryllium oxide. The roughness and waviness contact resistances are about the same order of magnitude. Also consistently observed is a decrease in the radiative contact resistance with increasing temperature. The decrease is by a factor of between 15 and 20 over the temperature range studied. Such a decrease in resistance is expected due to the  $T^{-3}$  dependence of this term.

The final results of the analytical calculation using Equation 32 are compared with the experimental measurements on the 10 and 40  $\mu$  in. interfaces in Figures 36 and 37, respectively. The predicted conductive and radiative contributions to the total interfacial conductance are also indicated. As inferred qualitatively in Section III.C., radiative contributions are much more important for the rougher 40  $\mu$  in. interface, the conductive and radiative contributions becoming equal at about 950° F for this interface; for the smoother interface, the radiative contribution does not equal the conductive contribution until a temperature of 1450° F is reached. In absolute magnitude, the radiative contributions are about the same for the two interfaces. However, the solid contribution is 4.5 times greater for the smooth interface, thus decreasing the relative importance of radiative transport.

The dimensionless grouping of Biot modulus form,  $\bar{h}_R \ell / k$ , introduced earlier, was calculated for each of the analytically predicted data points. Calculation of this group termed the Interfacial Heat Transport Modulus,  $H_I$ , is summarized in Table X. The characteristic length,  $\ell$ , is the horizontal distance between waviness contact areas, which is a quantitative measure of the distance from the interface, in which there is significant perturbation of the temperature field.

In general,  $h_R = f(T_m^3)$  and  $k = f(1/T_m)$ , thus it would be expected that the interfacial heat transport modulus should exhibit a  $T^4$  functionality,

$$H_I = h_R \ell / k = f(T_m^4) \quad (34)$$

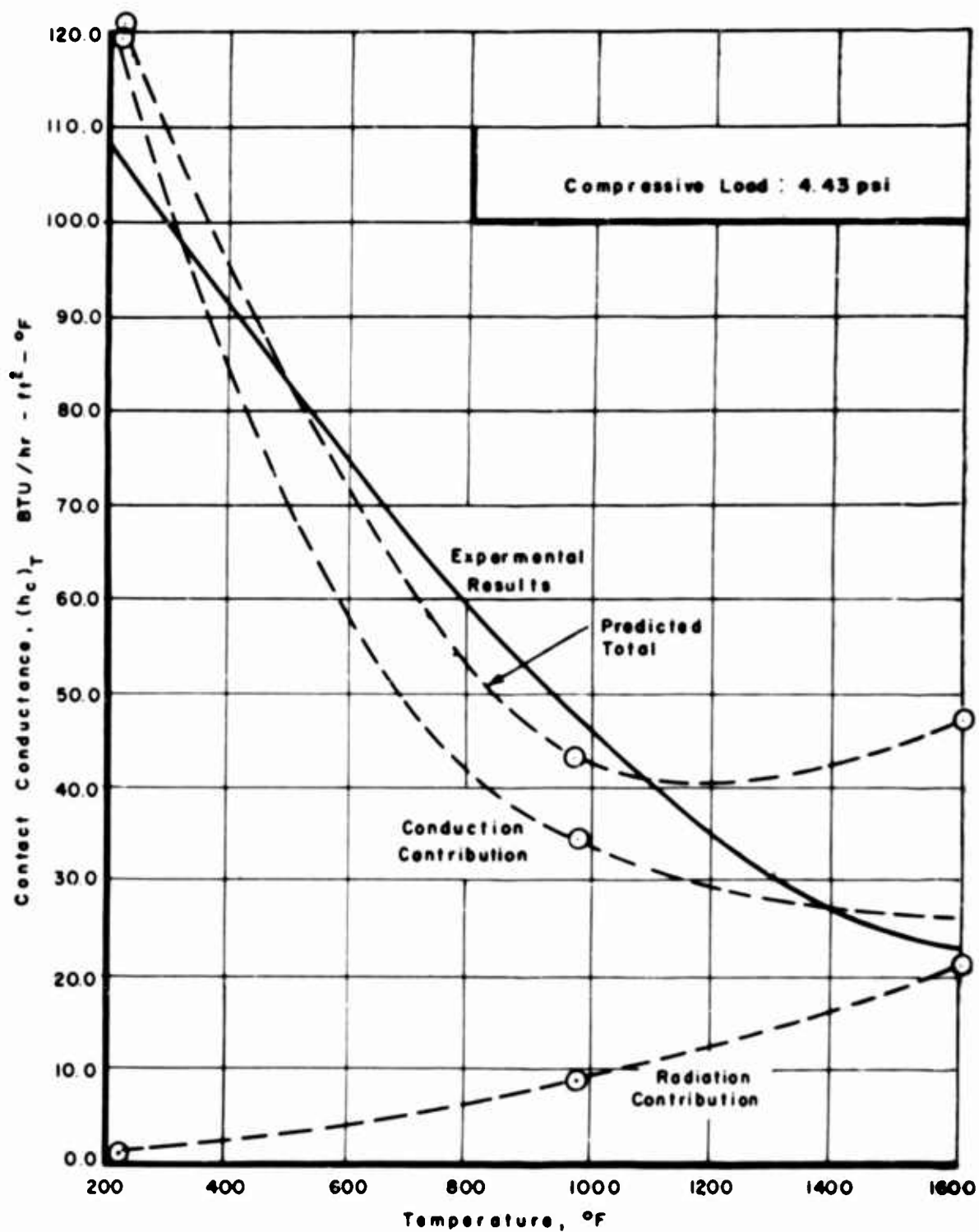
TABLE IX  
ROUGHNESS-WAVINESS CONTACT RESISTANCE RESULTS\*

$T_m$ °F	10 $\mu$ in. Interface					40 $\mu$ in. Interface		
	$R_w$ i	$R_{rgh}$ i	$R_{Rad}$ i	$R_w$ j	$R_{rgh}$ j	$R_{Rad}$ j	$R_w$	$R_{rgh}$ $R_{Rad}$
300	0.087	0.0704	476.0	0.144	0.129	1250.0	0.132	0.264 267.0
820	0.292	0.246	58.3	0.494	0.451	157.0	0.230	0.470 68.5
1600	0.580	0.317	23.6	0.913	0.581	63.7	0.751	1.220 20.5

\* All contact resistance values are in units of  $(\text{BTU/hr} \cdot ^\circ \text{F})^{-1}$

TABLE X  
INTERFACIAL HEAT TRANSPORT MODULUS RESULTS,  $H_I$

10 $\mu$ in. Interface						
$T_m$		$\bar{h}_R$	$l$	$k$	$\bar{h}_R l / k$	
$^{\circ}F$	$^{\circ}R$	BTU/hr-ft $^2$ - $^{\circ}F$	in.	BTU/in./hr-ft $^2$ - $^{\circ}F$		
228.5	688.5	1.10	0.213	1190.0	0.000197	
971.6	1431.5	8.67	0.213	339.0	0.00544	
1610.4	2070.4	21.43	0.213	176.0	0.02590	
40 $\mu$ in. Interface						
$T_m$		$\bar{h}_R$	$l$	$k$	$\bar{h}_R l / k$	
$^{\circ}F$	$^{\circ}R$	BTU/hr-ft $^2$ - $^{\circ}F$	in.	BTU/in./hr-ft $^2$ - $^{\circ}F$		
353.2	813.2	1.65	0.1672	920.0	0.000030	
722.5	1182.5	4.64	0.1672	519.0	0.00150	
1462.5	1922.5	17.10	0.1672	199.0	0.01440	

Figure 36. Experimental-Analytical Contact Conductance Comparisons: 10  $\mu$ in. Interface

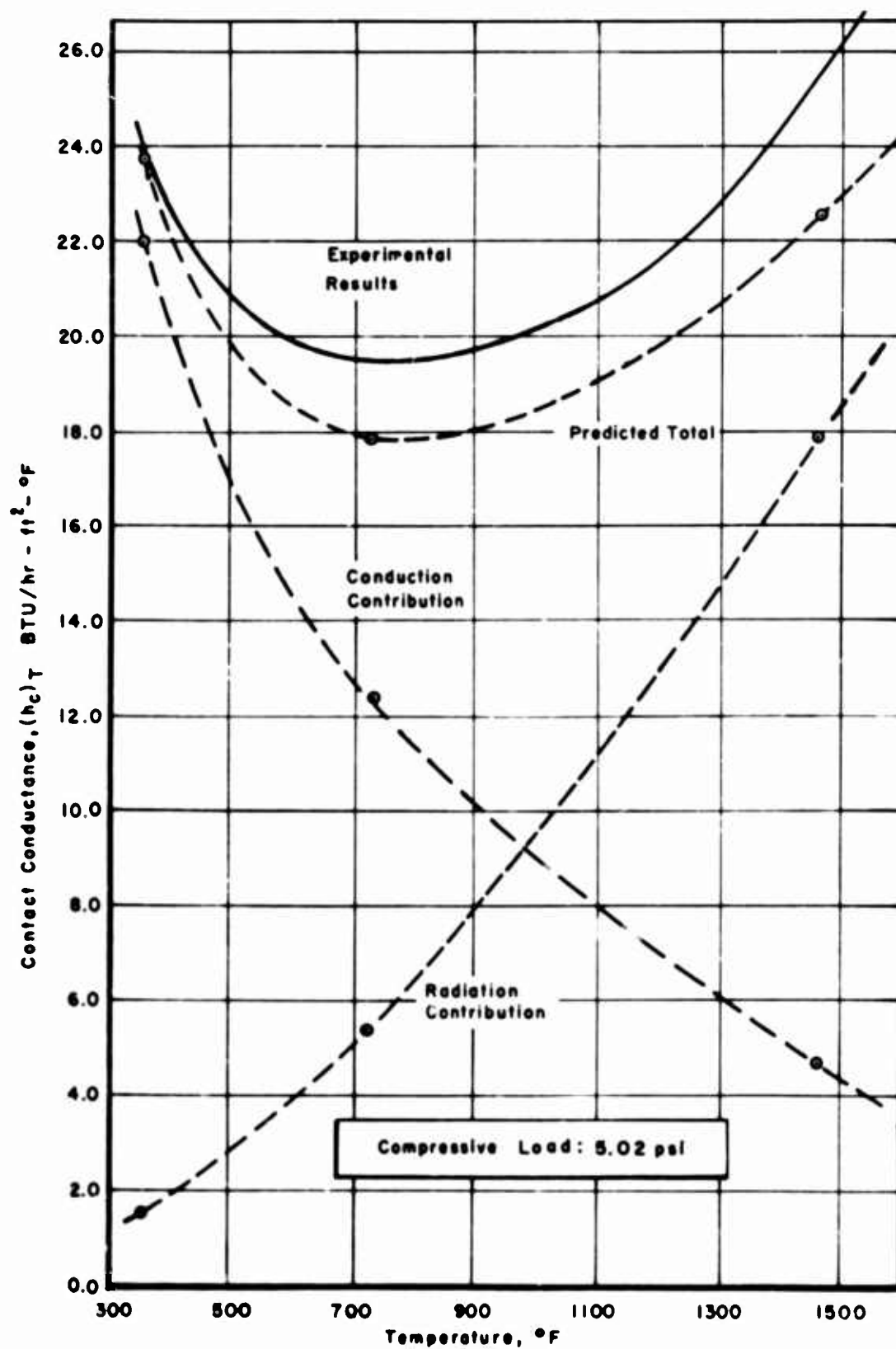


Figure 37. Experimental-Analytical Contact Conductance Comparisons: 40  $\mu$  in. Interface



where  $T_m$  is in degrees Rankine. The values in Table X are plotted on log-log coordinates in Figure 38. The  $H_I$  values clearly define straight lines. The slopes are the same and are just slightly above 4.0, in both cases equaling 4.4. That the curves for the two interfaces do not coincide but are offset by a constant amount is expected. This is because the absolute magnitude of the solid conduction contributions at low temperature are different for each interface:

$$k_{10 \mu \text{in.}} = C_1 f(1/T_m) \quad \text{and} \quad k_{40 \mu \text{in.}} = C_2 f(1/T_m), \quad C_1 \neq C_2$$

The  $H_I$  value is useful because it gives a direct measure of the relative contributions of conductive and radiative heat transport across the interface. Knowing the value for a given interface at a given temperature allows estimation of the value at other temperatures through the  $(T_m)^{4.4}$  dependence.

Clausing and Chao (Reference 25) have expressed the interfacial contact conductance in dimensionless form using the ratio of  $(h_c)_T$  times a characteristic surface dimension to the mean thermal conductivity of the contacting specimens. These authors term this ratio a Biot number although it has an entirely different physical significance from the interfacial heat transport modulus,  $H_I$ . Clausing and Chao considered the influence of roughness and waviness on solid conduction across the interface. Thus the Biot number they employ is basically a ratio of solid conduction across the interface to conduction in the bulk. The  $H_I$  grouping defined here is used in the more conventional sense of the Biot modulus (Reference 32). That is, it is defined as the ratio of a surface heat transfer coefficient to a bulk-media transport property.

The predicted contact conductance curves in Figures 37 and 38 fall an average of 11% below the measured values although they are within the scatter of the experimental results which was estimated to be  $\pm 12$  to  $\pm 23\%$  (Table V). The slightly lower predicted values are attributed to the fact that the contact model somewhat underestimates the solid conduction contribution due to the reduction in compressive strength of the beryllium oxide with increasing temperature. Because of the high radiative contributions at elevated temperatures, both predicted curves are sensitive to the emittance values in this range. The possible uncertainties in this data at elevated temperature is indicated in Figure 43 of Appendix III. The emittance data measured during this investigation falls between other data reported in the literature, which exhibits a very considerable spread.

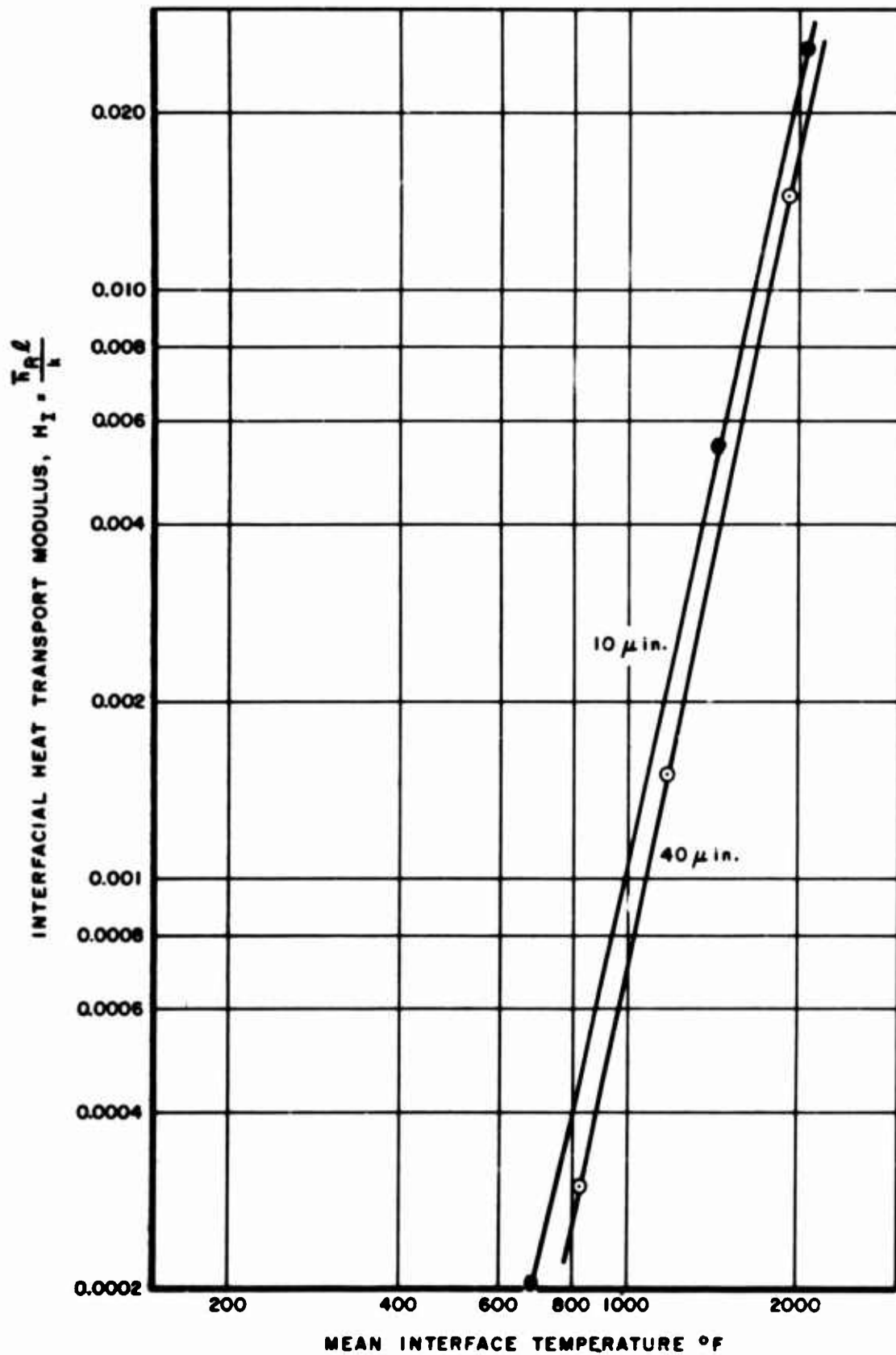


Figure 38. Interfacial Heat Transport Modulus for the 10 and 40  $\mu$  in. Interfaces

The analysis used here and the results obtained suggested a simpler, partially empirical method of obtaining predicted curves of  $(h_c)_T$  as a function of  $T_m$ . This simplified analysis is given in the next section.

### C. A SIMPLIFIED ANALYTICAL PREDICTION PROCEDURE

During the experimental measurements a value of  $\Delta T_c$  is obtained directly by gradient extrapolation to the interface. There certainly are temperature variations radially along the gap surfaces but the finite element analysis showed these to be fairly small. Thus, the measured  $\Delta T_c$  gives a representative average. The radiative transport across the interface could then be approximated fairly accurately by Equation 35,

$$q_{Rad} \cong \sigma \mathcal{F}_\epsilon (4T_m^3) \Delta T_c \quad (35)$$

and

$$(h_c)_{Rad} \cong \sigma \mathcal{F}_\epsilon (4T_m^3)$$

A great amount of surface profile analysis is required to arrive at an independent estimate of the interfacial contact area, and ultimately, the solid conduction contribution. Now, if the radiative contributions to the total contact conductance are small at low temperatures, it can usually be assumed that the total interfacial heat transfer is due only to conduction across the solid contacts. Knowing the beryllium oxide thermal conductivity temperature dependency makes it reasonable to assume that the change in the solid conduction contribution to the total contact resistance with temperature follows the same dependency. If the total low temperature contact conductance is defined as  $(h_c)_0$  then the solid conduction contribution as a function of temperature can be approximated as

$$(h_c)_{cond} = (h_c)_w + (h_c)_{rgh} = (h_{c_0}) / T_m$$

Using the experimentally determined values of  $T_m$ ,  $\Delta T_c$  and  $(h_c)_0$  and Equations 35 and 36, the predicted contact conductance curves shown in Figures 39 and 40 were generated for the 10 and 40  $\mu$  in. interfaces, respectively.

The shapes of the predicted curves in these figures are slightly different from those obtained from the exact analysis described earlier, but still the general similarity and the agreement between experimental and predicted results is striking considering the simplicity of this analysis. As stated initially, however, an experimental contact resistance measurement,  $(h_c)_0$ , is required to use the analysis.

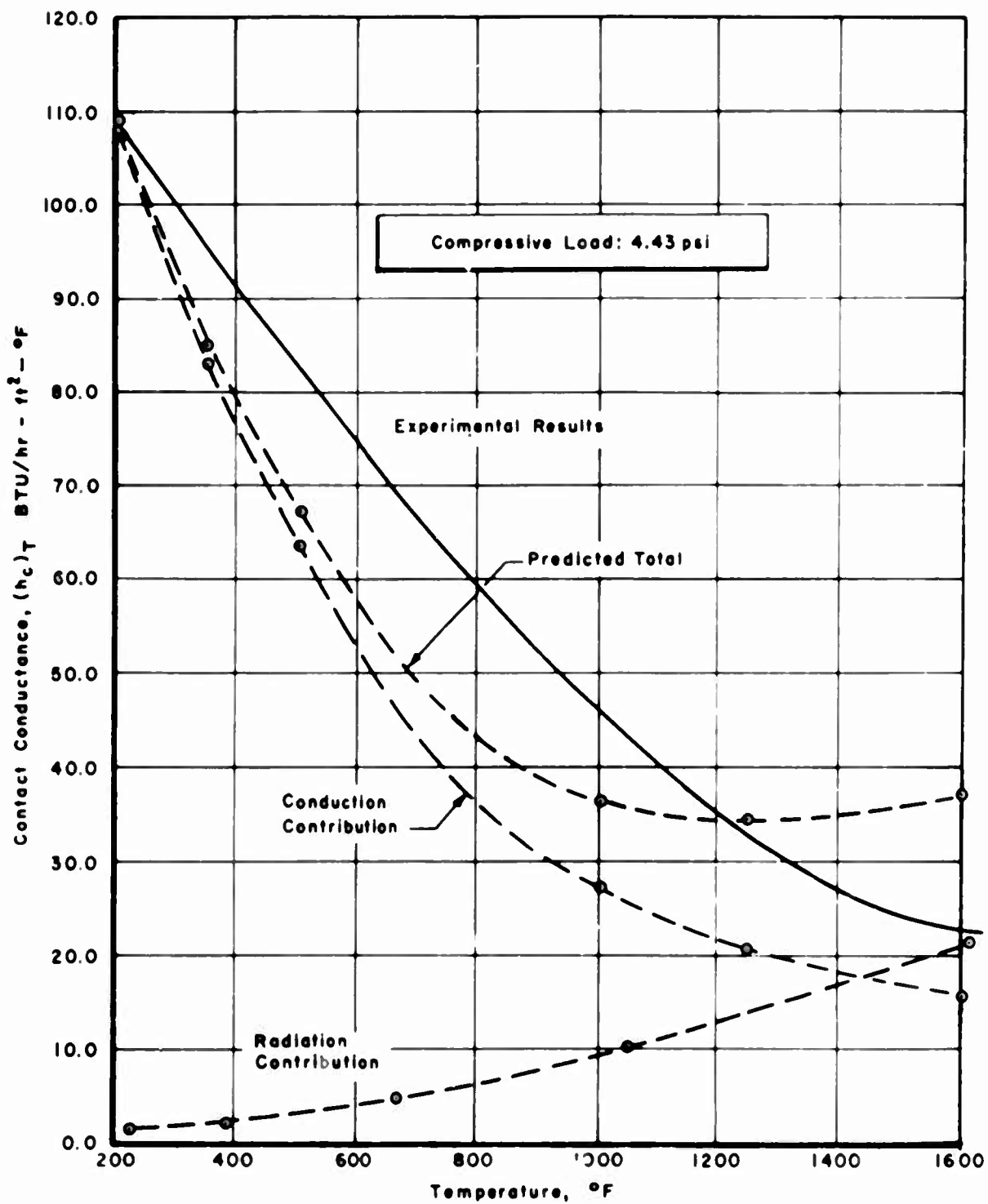


Figure 39. Experimental-Analytical Contact Conductance Comparisons: Simplified Analysis - 10  $\mu$  in. Interface

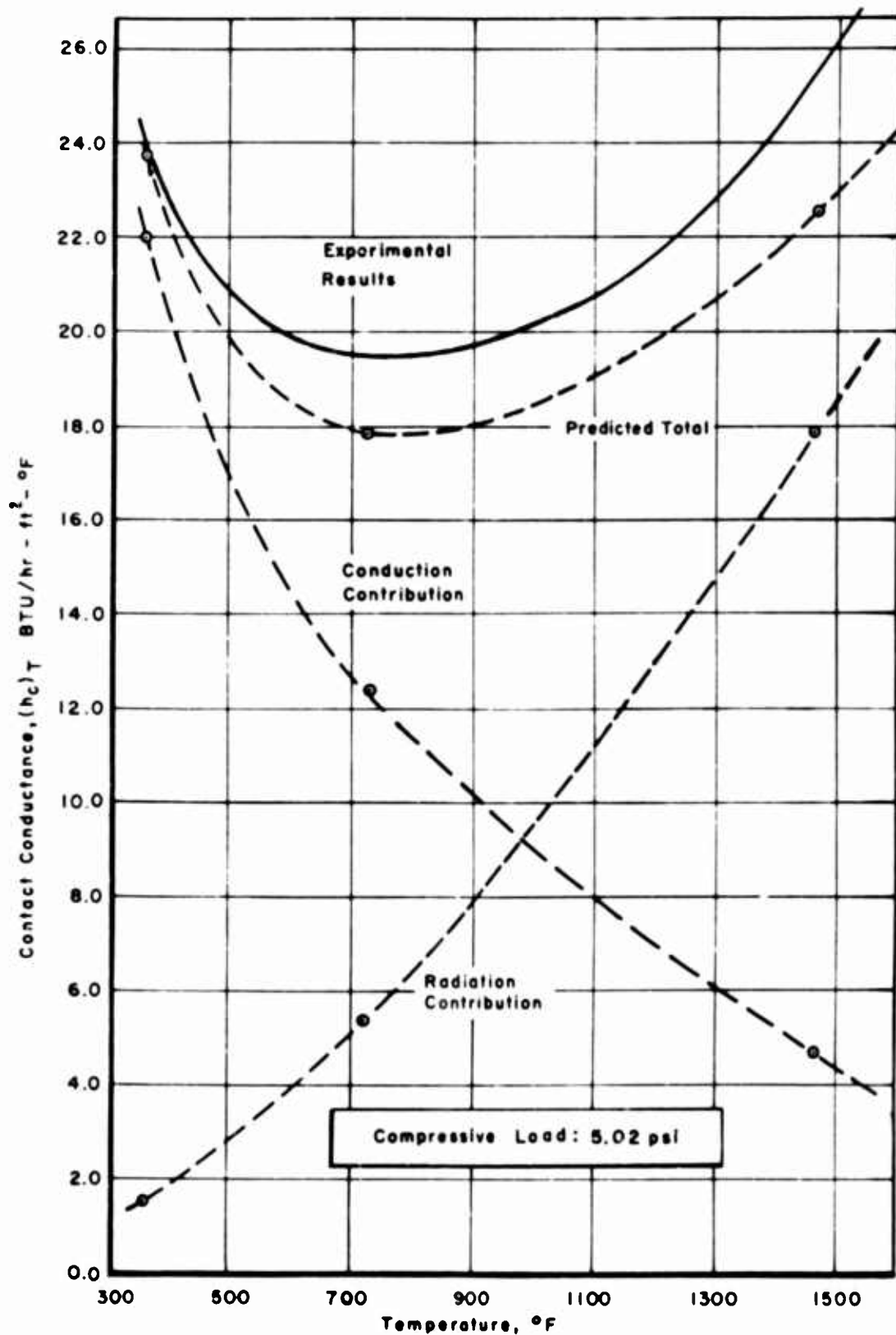


Figure 40. Experimental-Analytical Contact Conductance Comparisons:  
Simplified Analysis - 40  $\mu$  in. Interface

## SECTION V

### CONCLUSIONS AND RECOMMENDATIONS

In this section conclusions and recommendations are based on the extensive measurements and analyses conducted in assessing the performance of the experimental equipment and in studying the character of heat transport across beryllium oxide interfaces, as already discussed in this report. The conclusions and recommendations are presented by section topic as given earlier.

#### A. CONCLUSIONS

##### 1. Design, Construction, and Qualification Testing of Experimental Equipment

The design philosophy of providing a large lateral thickness of thermal insulation for the relatively high conductivity specimen column to minimize radial losses while at the same time maintaining only approximate thermal balancing requirements on the guard heater was proved sound. Continual operation with hot side temperatures of over 2000° F was achieved. Heat losses were held to within 5% with guard mismatching ranging from +23 to -11%, while thermal conductivity data was obtained in excellent agreement with data reported in the literature.

The beryllium oxide thermal conductivity data measured with the equipment designed and built during this program had a precision to within better than  $\pm 2\%$ . The temperature dependence of the results was in exact accord with theoretical predictions and the literature values (bracketed data) available on specimens in the same purity and density range. Estimated accuracy of the data was  $\pm 3\%$ . The thermal conductivity data run on tantalum as an additional check of equipment performance exhibited a precision of  $\pm 1.5\%$ . Available literature values for this metal exhibit a wide scatter; however, the data obtained in this investigation agreed with recommended values within  $\pm 2\%$  up to 750° F, and deviated no more than 7.5% at 1200° F.

Analytically predicted heat losses in the apparatus agreed within a factor of 1.2 to 3 with experimental measurements. Uncertainties in available physical property data and in true temperatures at the insulation boundaries prevented exact application of these analytical equations which could easily be parameterized to produce general design equations for the cut-bar type of conductivity-contact resistance apparatus.

## 2. Experimental Generation and Analyses of BeO Interfacial Contact Resistance

Detailed surface characterization is required which includes precise analysis of relatively large scale surface undulations (waviness and curvature) as well as the more conventionally studied microscopic surface irregularities (roughness). For the carefully prepared interfaces studied here, roughness and waviness contribute about equally in determining the nature of solid phase heat transport across the interfaces.

The physical character of the 10  $\mu$  in. CLA and the 40  $\mu$  in. CLA surfaces studied here were fundamentally different. The 10  $\mu$  in. specimens had relatively flat asperity surfaces reflecting the polishing procedures used, while the 40  $\mu$  in. specimens exhibited a rougher peak pattern due to the vapor-blasting operation employed in surface preparation. These differences in geometrical character lead to significantly different interfacial heat transfer patterns, which were consistently explained.

The thermal contact conductance results exhibited several consistent trends:

- a. The values for the smoother 10  $\mu$  in. interface were higher by a factor of 3 to 4 than those for the 40  $\mu$  in. interface at comparable compressive load levels.
- b. The values increased rapidly with compressive load.
- c. Radiative heat transport across the interfaces was important at high temperatures, particularly at low compressive load levels. This contribution increases by a factor of up to 20 in the temperature range from 200 to 1600° F and was a major contributor to the net interfacial heat transport.
- d. The contact conductance curves were repeatable on cooling. And,
- e. The compressive load on the interface serves to reduce the relative contributions of radiative transport indirectly by preventing the generation of large  $\Delta T_c$  values at higher temperatures.

An estimate of the effective interfacial gap width was obtained through thermal contact resistance measurements in argon. These data confirmed, by direct measurement, the importance of surface waviness on the pattern of interfacial heat transport.

A combined roughness-waviness interfacial heat transfer model was formulated which successfully correlated the experimental measurements within 10%, including the contributions of high temperature radiative transport across the contact. The thermal resistances induced

by surface waviness were in series with those induced by the roughness, the combination being in parallel with the thermal resistance across the radiation gap regions.

The nonlinear character of the radiative transport effects were successfully incorporated in a finite-element analysis that exhibited stable convergence over wide ranges of radiation heat transfer coefficient.

The relative contributions of radiative and conductive transport across the interface and their combined influence on the temperature field distortion were characterized by a dimensionless interfacial heat transport modulus,  $H_I = h_R \ell / k$ . This group was proportional to the 4.4 power of the mean interface temperature,  $T_m$ , expressed in °R; a 4.0 dependence was predicted theoretically for the beryllium oxide interface.

Analyses using the combined contact heat transport model showed quantitatively that radiative contributions were much more important for the rougher 40  $\mu$  in. interface, equalling the conductive contribution at 950° F for the low compressive load case. For the 10  $\mu$  in. interface, these contributions were not equal until an interface temperature of 1450° F was reached.

A simplified analytical procedure for predicting the temperature dependency of the thermal contact conductance was applied successfully, giving essentially the same results at the more detailed combined model analysis. This simplified procedure was empirical in nature, however, requiring one contact resistance measurement for a given interface at a given load level.

## B. RECOMMENDATIONS

### 1. Experimental Equipment

The apparatus should be modified to include a secondary heater between the bottom of the specimen column and the water-cooled copper pedestal (Figure 2). This modification would allow independent variation of the mean interface temperature and the heat flux in the specimens. Operation in this fashion is not possible unless there is independent control of the temperature at the bottom of the specimen column.



The analytical heat loss equations developed in Section II. B. 3 should be used to generate generalized apparatus design curves such as the following:

- a.  $q_{\text{loss}}$  as a function of insulation thermal conductivity with specimen conductivity as a parameter.
- b.  $q_{\text{loss}}$  as a function of insulation to specimen diameter ratio, with specimen to insulation conductivity ratio as a parameter. And,
- c.  $q_{\text{loss}}$  as a function of guard-specimen column temperature gradient mismatch with both of the parameterizations mentioned above.

For calculations in a, b, and c, Equations 21 and 22 are directly useful, since IBM 7094 programs have been written for their evaluation.

Additional thermal conductivity measurements on tantalum should be made to higher temperatures so that comparisons can be made with the higher temperature literature data of Figure 12. Concurrent electrical resistivity measurements would also be necessary.

## 2. Thermal Contact Resistance Measurement and Analysis Program

To allow convenient use of the analysis techniques developed in this investigation two extremely time consuming steps should be simplified:

- a. The analysis of the surface roughness and waviness data. And,
- b. The analysis of the contact element temperature distribution data required in calculating the waviness and radiation thermal resistances.

Statistical analyses of the surface data as suggested by Henry (Reference 33) is reasonable for random-lay finishes. Study of practical, non-Gaussian distributions should be emphasized. The analyses of the computer-generated finite element temperature fields could be conducted with the computer by incorporating an array of logic-comparison operations in picking the proper parameters for evaluating Equations 30 and 31 and for determining  $\Delta T_c$ .

Thermal contact resistance measurements to higher mean interface temperatures would be extremely useful in studying in more detail the radiative transport across different types of interfaces. Because the contact conductance is not an intrinsic property at high temperatures (i.e., it is heat flux and temperature gradient dependent), the interfacial flux,  $\Delta T_c$  and  $T_m$  should be varied systematically. The equipment modifications recommended above would facilitate these measurements.

It is recommended that future measurements be confined to surfaces with practical finishes. Idealized contact elements such as that depicted in Figure 30 have been experimentally studied by many investigators, proving quite conclusively that the basic model is physically sound. The major problem today is developing usable ways of incorporating these results in predictions for real surfaces. Studies on other nonmetallic interfaces are necessary due to the continual occurrence of such contacts in practice (Reference 1). Other brittle materials such as aluminum oxide, zirconium oxide, zirconium diboride, hafnium carbide, and various silicides should be studied as interface components along with semi-brittle materials such as Union Carbide ATJ graphite and the Poco Graphite Corporation series of materials.

APPENDIXES

# APPENDIX I

## HEAT LOSS ANALYSIS

The boundary conditions given in Figure 8 were used to formulate the Laplace equation for obtaining the temperature distribution in the cylindrical thermal insulation segment and is expressed in the following way for this two-dimensional axisymmetric case

$$\nabla^2 T = \frac{\partial^2 T}{\partial r^2} + \frac{1}{r} \frac{\partial T}{\partial r} + \frac{\partial^2 T}{\partial z^2} = 0$$

Implicit in the writing of this equation are temperature independent properties for the medium in which the temperature distribution is sought. Since the differential equation is linear, the influence of each boundary condition can be determined separately, that is, superposition can be applied. The solution considering only boundary condition 4 (Figure 8) is given first, followed by the solution considering boundary conditions 1 and 2 simultaneously.

### A. SOLUTION CONSIDERING BOUNDARY CONDITION 4

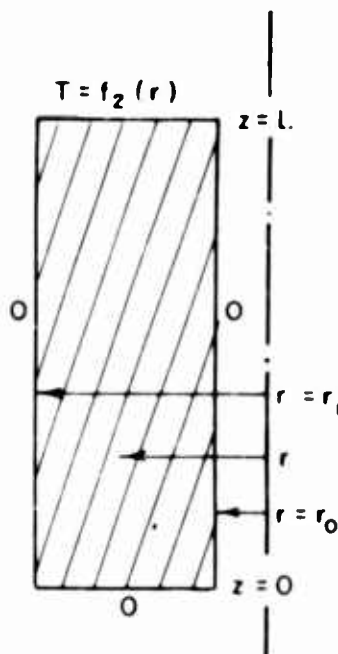
The simplified boundary conditions used in this development are as follows:

$$r = r_0, \quad z, \quad T = 0$$

$$r = r_1, \quad z, \quad T = 0$$

$$r_0 < r < r_1, \quad z = 0, \quad T = 0$$

$$r_0 < r < r_1, \quad z = L, \quad T = f_2(r)$$



Assuming a solution of the form

$$T(r, z) = R(r) Z(z)$$

and substituting in the differential equation:

$$\nabla^2 T = \frac{\partial^2 T}{\partial r^2} + \frac{1}{r} \frac{\partial T}{\partial r} + \frac{\partial^2 T}{\partial z^2} = 0$$

yields the following system of ordinary differential equations:

$$\frac{1}{Z(z)} \cdot \frac{d^2 Z(z)}{dz^2} = K^2$$

and

$$\frac{1}{R(r)} \cdot \frac{d^2 R(r)}{dr^2} + \frac{1}{r} \cdot \frac{1}{R(r)} \cdot \frac{dR(r)}{dr} = -K^2$$

or

$$\frac{d^2 Z(z)}{dz^2} - Z(z) K^2 = 0$$

and

$$\frac{d^2 R(r)}{dr^2} + \frac{1}{r} \frac{dR(r)}{dr} + K^2 R(r) = 0$$

A question may arise concerning the sign of  $K'^2$ . To satisfy boundary condition 4, it is necessary that the Fourier coefficient integrals involve  $J_0(r)$ . This condition is met when the generalized solution is in the form of the hyperbolic function, zero order Bessel function product; the sign of  $K'^2$  assumed here will lead to a solution of this form. In the next portion of the solution the opposite sign is required.

Transforming the independent variables to  $Kr$  and  $Kz$ , we get:

$$\frac{d^2 R(Kr)}{d(Kr)^2} + \frac{1}{Kr} \frac{dR(Kr)}{d(Kr)} + R(Kr) = 0$$

and

$$\frac{d^2 Z(Kz)}{d(Kz)^2} - Z(Kz) = 0$$

The equation in  $\chi r$  is in the form of Bessel's equation of zero order and has the general solution:

$$R(\chi r) = A J_0(\chi r) + B Y_0(\chi r)$$

where  $J_0$  and  $Y_0$  are the Bessel functions of first and second kind of zero order.

The equation in  $\chi z$  has a solution in terms of exponentials with real argument which, in the most general case, is expressed as follows:

$$Z(\chi z) = C \cosh(\chi z) + D \sinh(\chi z)$$

Thus, a solution of the original differential equation becomes

$$T(r, z) = [A J_0(\chi r) + B Y_0(\chi r)] [C \cosh(\chi z) + D \sinh(\chi z)]$$

Turning to the boundary conditions (Figure 8), from B.C. 3

$$\longrightarrow C = 0$$

or

$$T(r, z) = [A J_0(\chi r) + B Y_0(\chi r)] [D \sinh(\chi z)]$$

To apply B.C.'s 1 and 2 the following conditions must be met:

$$[A J_0(\chi r_0) + B Y_0(\chi r_0)] [D \sinh(\chi z)] = 0$$

and

$$[A J_0(\chi r_1) + B Y_0(\chi r_1)] [D \sinh(\chi z)] = 0$$

By combining these equations and eliminating the constants A and B the following condition is obtained:

$$Y_0(\chi r_0) J_0(\chi r_1) - Y_0(\chi r_1) J_0(\chi r_0) = 0$$

This condition is fulfilled by an infinite number of eigenvalues,  $\chi_n$ , which are the positive roots of this equation. Introducing cylindrical function notation,

$$u_0(\chi_n, r_0; r_1) = J_0(\chi_n r_0) Y_0(\chi_n r_1) - J_0(\chi_n r_1) Y_0(\chi_n r_0)$$

we can define the eigenvalues

$$u_0(\chi_n; r_0; r_1) = 0, \quad n = 1, 2, 3, \dots$$

Thus, there are an infinite number of general solutions to this boundary value problem of the form:

$$T(r, z) = [A_n J_0(\chi_n r) + B_n Y_0(\chi_n r)] [D_n \sinh(\chi_n z)]$$

or

$$T(r, z) = [E_n J_0(\chi_n r) + F_n Y_0(\chi_n r)] [\sinh(\chi_n z)]$$

Subsequent Fourier coefficient evaluations are facilitated if the above equation is cast in terms of the cylindrical function  $u_0(\chi_n; r_i, r_j)$ ,  $i$  and  $j = 0, 1$ .

Defining  $Q(\chi_n r)$  as

$$Q(\chi_n r) \equiv E_n J_0(\chi_n r) + F_n Y_0(\chi_n r)$$

then

$$Q(\chi_n r_0) = E_n J_0(\chi_n r_0) + F_n Y_0(\chi_n r_0)$$

and

$$Q(\chi_n r_1) = E_n J_0(\chi_n r_1) + F_n Y_0(\chi_n r_1)$$

Combining these equations to obtain expressions for  $E_n$  and  $F_n$  results in:

$$\begin{aligned} E_n &= \frac{Q(\chi_n r_1) Y_0(\chi_n r_0) - Q(\chi_n r_0) Y_0(\chi_n r_1)}{J_0(\chi_n r_1) Y_0(\chi_n r_0) - J_0(\chi_n r_0) Y_0(\chi_n r_1)} \\ &= \frac{Q(\chi_n r_1) Y_0(\chi_n r_0) - Q(\chi_n r_0) Y_0(\chi_n r_1)}{u_0(\chi_n; r_0; r_1)} \end{aligned}$$

and

$$\begin{aligned} F_n &= \frac{Q(\chi_n r_0) J_0(\chi_n r_1) - Q(\chi_n r_1) J_0(\chi_n r_0)}{Y_0(\chi_n r_0) J_0(\chi_n r_1) - Y_0(\chi_n r_1) J_0(\chi_n r_0)} \\ &= \frac{Q(\chi_n r_0) J_0(\chi_n r_1) - Q(\chi_n r_1) J_0(\chi_n r_0)}{u_0(\chi_n; r_0; r_1)} \end{aligned}$$

Now,

$$\begin{aligned}
 Q(\kappa_n r) &= \frac{[Q(\kappa_n r_1) Y_0(\kappa_n r_0) - Q(\kappa_n r_0) Y_0(\kappa_n r_1)] J_0(\kappa_n r)}{u_0(\kappa_n; r_0; r_1)} \\
 &+ \frac{[Q(\kappa_n r_0) J_0(\kappa_n r_1) - Q(\kappa_n r_1) J_0(\kappa_n r_0)] Y_0(\kappa_n r)}{u_0(\kappa_n; r_0; r_1)} \\
 &= \frac{Q(\kappa_n r_1) [Y_0(\kappa_n r_0) J_0(\kappa_n r) - J_0(\kappa_n r_0) Y_0(\kappa_n r)]}{u_0(\kappa_n; r_0; r_1)} \\
 &+ \frac{Q(\kappa_n r_0) [J_0(\kappa_n r_1) Y_0(\kappa_n r) - Y_0(\kappa_n r_1) J_0(\kappa_n r)]}{u_0(\kappa_n; r_0; r_1)}
 \end{aligned}$$

Simplifying, we get

$$Q(\kappa_n r) = \frac{Q(\kappa_n r_1) [u_0(\kappa_n; r_0; r)] + Q(\kappa_n r_0) [u_0(\kappa_n; r; r_1)]}{u_0(\kappa_n; r_0; r_1)}$$

Thus, a solution of the differential equation can be written:

$$T(r, z) = Q(\kappa_n r) \cdot \sinh(\kappa_n z)$$

In addition, any linear combination of solutions of the above form will be a solution of the equation. That is,

$$T(r, z) = \sum_{n=1}^{\infty} Q(\kappa_n r) \cdot \sinh(\kappa_n z)$$

or

$$T(r, z) = \sum_{n=1}^{\infty} \frac{Q(\kappa_n r_1) [u_0(\kappa_n; r_0; r)] + Q(\kappa_n r_0) [u_0(\kappa_n; r; r_1)]}{u_0(\kappa_n; r_0; r_1)} \cdot \sinh(\kappa_n z)$$

It now remains to satisfy B.C. 4. By substitution in the above equation

$$T(r, L) = f_2(r) = \sum_{n=1}^{\infty} \frac{Q(\kappa_n r_1) [u_0(\kappa_n; r_0; r)] + Q(\kappa_n r_0) [u_0(\kappa_n; r; r_1)]}{u_0(\kappa_n; r_0; r_1)} \sinh(\kappa_n L)$$



The quantities  $Q(\chi_n, r_1)$  and  $Q(\chi_n, r_0)$ , which contain the constants  $E_n$  and  $F_n$  can be considered the coefficients of a cylindrical function Fourier series with a general term of the form  $u_0(\chi_n; r; r_1) \cdot \sinh(\chi_n z)$ . The Euler formulas will then be of the form

$$a_n = \frac{1}{N\{u_0(r)\}} \int_{r=r_0}^{r=r_1} r f_2(r) u_0(r) dr$$

where the norm  $N\{u_0(r)\}$  is found by applying Lommel integral relations.

The final result for the case considered here is given by Carslaw and Jaeger (Reference 34) as:

$$T(r, z) = \frac{\pi^2}{2} \sum_{n=1}^{\infty} \frac{\chi_n^2 J_0^2(\chi_n r_0) u_0(\chi_n; r; r_1) \sinh(\chi_n z)}{[J_0^2(\chi_n r_0) - J_0^2(\chi_n r_1)] \sinh(\chi_n L)} \int_{r=r_0}^{r=r_1} r f_2(r) u_0(\chi_n; r; r_1) dr$$

where

$f_2(r)$  is an arbitrary temperature distribution along

$$r_0 < r < r_1, \quad z = L$$

and

$\chi_n$  are the positive roots of  $u_0(\chi_n; r_0; r_1) = 0$

## B. SOLUTION CONSIDERING BOUNDARY CONDITIONS 1 AND 2

With the above solution for boundary condition 4 now established, it is necessary to calculate the influence of boundary conditions 1 and 2 (Figure 8) on the overall temperature field. This is done in a manner somewhat analogous to the above derivation except that the solution will be in terms of modified Bessel functions and trigonometric functions to accommodate the cylindrical surfaces boundary conditions.

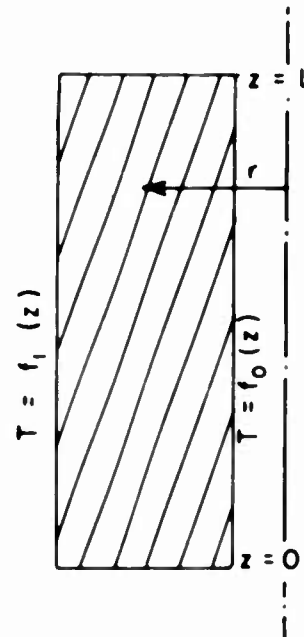
The problem to be solved is as follows. Given, are simplified Boundary Conditions (Specifically, originally P.C.'s 1 and 2):

$$(1) \quad r = r_0, z, T = f_0(z)$$

$$(2) \quad r = r_1, z, T = f_1(z)$$

$$(3) \quad r_0 < r < r_1, z = 0, T = 0$$

$$(4) \quad r_0 < r < r_1, z = L, T = 0$$



We will assume a solution of the form:

$$T(r, z) = \rho(r) \mathcal{J}(z)$$

Substituting in the differential equation:

$$\mathcal{J}(z) \frac{\partial^2 \rho(r)}{\partial r^2} + \frac{1}{r} \mathcal{J}(z) \frac{\partial \rho(r)}{\partial r} + \rho(r) \frac{\partial^2 \mathcal{J}(z)}{\partial z^2} = 0$$

and rearranging yield

$$\frac{1}{\rho(r)} \frac{\partial^2 \rho(r)}{\partial r^2} + \frac{1}{r} \frac{1}{\rho(r)} \frac{\partial \rho(r)}{\partial r} = - \frac{1}{\mathcal{J}(z)} \frac{\partial^2 \mathcal{J}(z)}{\partial z^2}$$

Since variables have been separated, two equations result:

$$\left. \begin{aligned} \frac{1}{\rho(r)} \frac{\partial^2 \rho(r)}{\partial r^2} + \frac{1}{r} \frac{1}{\rho(r)} \frac{\partial \rho(r)}{\partial r} &= +\lambda^2 \\ \frac{1}{\mathcal{J}(z)} \frac{\partial^2 \mathcal{J}(z)}{\partial z^2} &= -\lambda^2 \end{aligned} \right\} \lambda^2 = \text{constant}$$

or

$$\frac{d^2 \rho(r)}{dr^2} + \frac{1}{r} \frac{d\rho(r)}{dr} - \lambda^2 \rho(r) = 0$$

and

$$\frac{d^2 \mathcal{J}(z)}{dz^2} + \lambda^2 \mathcal{J}(z) = 0$$

Again, a question may arise concerning the sign of  $\lambda^2$ . If  $\lambda^2$  were negative, a solution could be obtained in terms of  $J_0(r)$  and  $Y_0(r)$ , zero order Bessel functions of the first and second kind, respectively, and in terms of the hyperbolic functions  $\sinh(z)$  and  $\cosh(z)$ , as shown earlier. As indicated below, if  $\lambda^2$  is assumed positive the solution is in terms of  $I_0(r)$  and  $K_0(r)$ , zero modified Bessel functions of the first and second kind, respectively, and in terms of the simple transcendental functions  $\sin(z)$  and  $(z) \cos$ . The latter alternative is used in order that a solution satisfying boundary conditions 1 and 2 can be obtained in Fourier series form.

The following relationships between the alternate solutions follows directly from examination of the differential equation:

$$\left. \begin{aligned} I_0(r) &= (i)^0 J_0(ir) \\ \sin(z) &= \frac{1}{i} \sinh(iz) \end{aligned} \right\} i = \sqrt{-1}$$

Transforming the independent variables to  $\lambda r$  and  $\lambda z$ :

$$\frac{d^2 \rho(\lambda r)}{d(\lambda r)^2} + \frac{1}{\lambda r} \frac{d\rho(\lambda r)}{d\lambda r} - \rho(\lambda r) = 0$$

This is the modified Bessel equation of zero order and has the solution:

$$\rho(\lambda r) = A' I_0(\lambda r) + B' K_0(\lambda r)$$

and

$$\frac{d^2 \mathcal{J}(\lambda z)}{dz^2} + \mathcal{J}(\lambda z) = 0$$

This transcendental equation has a solution of the form

$$\mathcal{G}(\lambda z) = C' \cos(\lambda z) + D' \sin(\lambda z)$$

Thus, a solution of the differential equation becomes

$$T(r, z) = [A' I_0(\lambda r) + B' K_0(\lambda r)] [C' \cos(\lambda z) + D' \sin(\lambda z)]$$

From B.C. 3:

$$\longrightarrow C'_3 = 0$$

or

$$T(r, z) = [A' I_0(\lambda r) + B' K_0(\lambda r)] D' \sin(\lambda z)$$

From B.C. 4:

$$T(r, L) = [A' I_0(\lambda r) + B' K_0(\lambda r)] D' \sin(\lambda L) = 0$$

This condition is fulfilled when

$$\lambda L = n\pi, \quad n = 0, 1, 2, \dots$$

or

$$\lambda = \frac{n\pi}{L}$$

Hence,

$$T(r, z) = \left[ E'_n I_0\left(\frac{n\pi r}{L}\right) + F'_n K_0\left(\frac{n\pi r}{L}\right) \right] \sin\left(\frac{n\pi z}{L}\right)$$

where now the constants  $E'$  and  $F'$  are subscripted as  $E'_n$  and  $F'_n$ , since there is a solution for each value of  $n$ .

A representation for  $E'_n$  and  $F'_n$  more convenient for Fourier coefficient evaluation can be obtained by defining the following quantities in cylindrical function form. In general, let

$$\rho(\lambda r) = \rho\left(\frac{n\pi r}{L}\right) \equiv E'_n I_0\left(\frac{n\pi r}{L}\right) + F'_n K_0\left(\frac{n\pi r}{L}\right)$$

Specifically,

$$\rho\left(\frac{n\pi r_0}{L}\right) = E'_n I_0\left(\frac{n\pi r_0}{L}\right) + F'_n K_0\left(\frac{n\pi r_0}{L}\right)$$

and

$$\rho \left( \frac{n \pi r_1}{L} \right) = E'_n I_0 \left( \frac{n \pi r_1}{L} \right) + F'_n K_0 \left( \frac{n \pi r_1}{L} \right)$$

Solving these equations for the constants  $E'_n$  and  $F'_n$  results in

$$E'_n = \frac{\rho \left( \frac{n \pi r_1}{L} \right) K_0 \left( \frac{n \pi r_0}{L} \right) - \rho \left( \frac{n \pi r_0}{L} \right) K_0 \left( \frac{n \pi r_1}{L} \right)}{I_0 \left( \frac{n \pi r_1}{L} \right) K_0 \left( \frac{n \pi r_0}{L} \right) - I_0 \left( \frac{n \pi r_0}{L} \right) K_0 \left( \frac{n \pi r_1}{L} \right)}$$

and

$$F'_n = \frac{\rho \left( \frac{n \pi r_0}{L} \right) I_0 \left( \frac{n \pi r_1}{L} \right) - \rho \left( \frac{n \pi r_1}{L} \right) I_0 \left( \frac{n \pi r_0}{L} \right)}{K_0 \left( \frac{n \pi r_0}{L} \right) I_0 \left( \frac{n \pi r_1}{L} \right) - K_0 \left( \frac{n \pi r_1}{L} \right) I_0 \left( \frac{n \pi r_0}{L} \right)}$$

These equations can be simplified by defining the function:

$$G_n(r_1, r_0) \equiv I_0 \left( \frac{n \pi r_1}{L} \right) K_0 \left( \frac{n \pi r_0}{L} \right) - I_0 \left( \frac{n \pi r_0}{L} \right) K_0 \left( \frac{n \pi r_1}{L} \right)$$

Thus,

$$E'_n = \frac{\rho \left( \frac{n \pi r_1}{L} \right) K_0 \left( \frac{n \pi r_0}{L} \right) - \rho \left( \frac{n \pi r_0}{L} \right) K_0 \left( \frac{n \pi r_1}{L} \right)}{G_n(r_1, r_0)}$$

and

$$F'_n = \frac{\rho \left( \frac{n \pi r_0}{L} \right) I_0 \left( \frac{n \pi r_1}{L} \right) - \rho \left( \frac{n \pi r_1}{L} \right) I_0 \left( \frac{n \pi r_0}{L} \right)}{G_n(r_1, r_0)}$$

Finally, by writing the equation for  $\rho \left( \frac{n \pi r}{L} \right)$  terms of these equations, the following result is obtained:

$$\rho \left( \frac{n \pi r}{L} \right) = \frac{\rho \left( \frac{n \pi r_1}{L} \right) G_n(r, r_0) + \rho \left( \frac{n \pi r_0}{L} \right) G_n(r_1, r)}{G_n(r_1, r_2)}$$

A solution of the differential equation can now be rewritten as

$$T(r, z) = \rho \left( \frac{n \pi r}{L} \right) \sin \left( \frac{n \pi z}{L} \right)$$

In addition, any linear combination of solutions of the above form will be a solution of the equation. In the most general sense,

$$T(r, z) = \sum_{n=1}^{\infty} \rho \left( \frac{n\pi r}{L} \right) \sin \left( \frac{n\pi z}{L} \right)$$

It now remains to satisfy boundary conditions 1 and 2 along the cylindrical surfaces  $r = r_0$  and  $r = r_1$ . Appropriate substitution in the above solution yields

$$\begin{aligned} T(r_0, z) = f_0(z) &= \sum_{n=1}^{\infty} \rho \left( \frac{n\pi r_0}{L} \right) \sin \left( \frac{n\pi z}{L} \right) \\ &= \sum_{n=1}^{\infty} \frac{\rho \left( \frac{n\pi r_1}{L} \right) G_n(r_0, r_0) + \rho \left( \frac{n\pi r_0}{L} \right) G_n(r_1, r_0)}{G_n(r_1, r_0)} \cdot \sin \left( \frac{n\pi z}{L} \right) \end{aligned}$$

Simplifying, we get

$$T(r_0, z) = f_0(z) = \sum_{n=1}^{\infty} \rho \left( \frac{n\pi r_0}{L} \right) \sin \left( \frac{n\pi z}{L} \right) = \sum_{n=1}^{\infty} \alpha_n \sin \left( \frac{n\pi z}{L} \right)$$

Similarly, by applying the boundary condition  $z, r = r_1$ :

$$T(r_1, z) = f_1(z) = \sum_{n=1}^{\infty} \rho \left( \frac{n\pi r_1}{L} \right) \sin \left( \frac{n\pi z}{L} \right) = \sum_{n=1}^{\infty} \beta_n \sin \left( \frac{n\pi z}{L} \right)$$

Then, if  $\alpha_n$  and  $\beta_n$  are considered as coefficients of the indicated Fourier series, the following expressions can be derived using the standard procedures (Reference 2) in developing Euler formulas for Fourier coefficients

$$\alpha_n = R \left( \frac{n\pi r_0}{L} \right) = \frac{2}{L} \int_0^L f_0(z) \sin \left( \frac{n\pi z}{L} \right) dz$$

and

$$\beta_n = R \left( \frac{n\pi r_1}{L} \right) = \frac{2}{L} \int_0^L f_1(z) \sin \left( \frac{n\pi z}{L} \right) dz$$

Combining results obtains

$$\begin{aligned} T(r, z) &= \frac{2}{L} \sum_{n=1}^{\infty} \frac{\sin \left( \frac{n\pi z}{L} \right)}{G_n(r_1, r_0)} \left\{ G_n(r, r_0) \int_0^L f_1(z) \sin \left( \frac{n\pi z}{L} \right) dz \right. \\ &\quad \left. + G_n(r_1, r) \int_0^L f_0(z) \sin \left( \frac{n\pi z}{L} \right) dz \right\} \end{aligned}$$

This equation combined with the result obtained separately for the original boundary condition 4 gives the following equation describing the temperature distribution in the annular insulation sketched at the outset:

$$T(r, z) = \frac{\pi^2}{2} \sum_{n=1}^{\infty} \frac{K_n^2 J_0^2(K_n r_0) u_0(K_n, r; r_1) \sinh K_n z}{[J_0^2(K_n r_0) - J_0^2(K_n r_1)] \sinh K_n L} \int_{r_0}^{r_1} r f_2(r) u_0(K_n; r, r_1) dr$$

$$+ \frac{2}{L} \sum_{n=1}^{\infty} \frac{\sin\left(\frac{n\pi z}{L}\right)}{G_n(r_1; r_0)} \left\{ G_n(r, r_0) \int_0^L f_1(z) \sin\left(\frac{n\pi z}{L}\right) dz \right.$$

$$\left. + G_n(r_1, r) \int_0^L f_0(z) \sin\left(\frac{n\pi z}{L}\right) dz \right\}$$

where

$$u_0(K_n; r_i; r_j) \equiv J_0(K_n r_i) Y_0(K_n r_j) - J_0(K_n r_j) Y_0(K_n r_i)$$

$$K'_n = \text{positive roots of } u_0(K'_n; r_0; r_1) = 0$$

$$G_n(r_i; r_0) \equiv I_0\left(\frac{n\pi r_i}{L}\right) K_0\left(\frac{n\pi r_0}{L}\right) - I_0\left(\frac{n\pi r_0}{L}\right) K_0\left(\frac{n\pi r_i}{L}\right)$$

$f_0(z), f_1(z), f_2(r)$  = arbitrary temperature distributions subject only to the requirement that the above integrals exist.

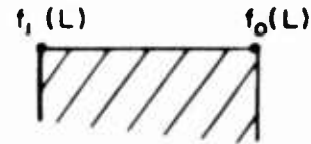
### C. EVALUATION OF FOURIER COEFFICIENT INTEGRALS

An explicit equation for  $T(r, z)$  describing the temperature field in the insulation with the experimentally observed boundary conditions is found through evaluation of the integrals in the above equation, and by making appropriate substitutions for the expressions  $f_0(z)$ ,  $f_1(z)$ , and  $f_2(r)$ .

For the particular experimental arrangement used here,  $f_2(r)$  is not arbitrary. Actually  $f_2(r)$  is uniquely defined by the condition that  $\nabla^2 T = 0$  along the surface,  $z = L$ , where the temperatures at positions  $r = r_0$  and  $r = r_1$  are  $f_0(L)$  and  $f_1(L)$ , respectively. For the

plane  $z = L$ , the temperature distribution defined by the equation  $\nabla^2 T = 0$  can be found via a one-dimensional solution:

$$\nabla^2 T = \frac{d^2 T}{dr^2} + \frac{1}{r} \frac{dT}{dr} = 0$$



Rewriting, we get

$$\frac{d}{dr} \left[ \frac{dT}{dr} \right] + \frac{1}{r} \left( \frac{dT}{dr} \right) = 0$$

Separating variables and integrating produces

$$\int \frac{d \left( \frac{dT}{dr} \right)}{\frac{dT}{dr}} = - \int \frac{dr}{r} \rightarrow \ln \left( \frac{dT}{dr} \right) = - \ln r + \overbrace{\ln c}^{\text{constant}}$$

or

$$\frac{dT}{dr} = \frac{C_1}{r}$$

Integrating again yields

$$\int dT = C_1 \int \frac{dr}{r} \rightarrow T = C_1 \ln r + C_2$$

Evaluation of constants gives

$$r = r_0, \quad T = f_0(L)$$

$$r = r_1, \quad T = f_1(L)$$

$$f_0(L) = C_1 \ln r_0 + C_2, \quad f_1(L) = C_1 \ln r_1 + C_2$$

$$C_2 = f_0(L) - C_1 \ln r_0, \quad f_1(L) = C_1 \ln r_1 + f_0(L) - C_1 \ln r_0$$

$$C_1 = \frac{f_1(L) - f_0(L)}{\ln \frac{r_1}{r_0}}, \quad C_2 = f_0(L) - \ln r_0 \left[ \frac{f_1(L) - f_0(L)}{\ln \frac{r_1}{r_0}} \right]$$



Thus,

$$T = \frac{f_1(L) - f_0(L)}{\ln\left(\frac{r_1}{r_0}\right)} \ln r + f_0(L) - \frac{f_1(L) - f_0(L)}{\ln\left(\frac{r_1}{r_0}\right)} \ln r_0$$

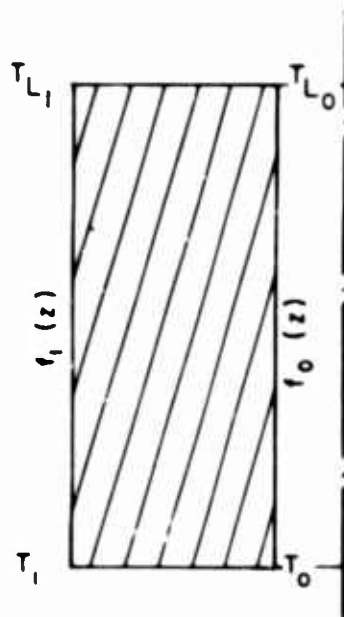
$$T = f_0(L) + \{f_1(L) - f_0(L)\} \left[ \frac{\ln \frac{r}{r_0}}{\ln \frac{r_1}{r_0}} \right]$$

Consider now the integral in the first series of the Equation for  $T(r, z)$ , which reads as follows:

$$\begin{aligned} & \int_{r_0}^{r_1} r f_2(r) u_0(K_n, r, r_1) dr \\ &= \frac{1}{\ln\left(\frac{r_1}{r_0}\right)} \int_{r_0}^{r_1} \left\{ f_0(L) + [f_1(L) - f_0(L)] \ln\left(\frac{r}{r_0}\right) \right\} r \cdot u_0(K_n, r, r_1) dr \\ &= \frac{1}{\ln\left(\frac{r_1}{r_0}\right)} \left[ f_0(L) \int_{r_0}^{r_1} r u_0(K_n, r, r_1) dr + [f_1(L) - f_0(L)] \int_{r_0}^{r_1} r u_0(K_n, r, r_1) \ln\left(\frac{r}{r_0}\right) dr \right] \\ &= \frac{1}{\ln\left(\frac{r_1}{r_0}\right)} \left[ f_0(L) \left\{ 2 \frac{[J_0(K_n r_0) - J_0(K_n r_1)]}{\pi K_n^2 J_0(K_n r_0)} \right. \right. \\ &\quad \left. \left. + \{f_1(L) - f_0(L)\} \left\{ 2 \frac{[J_0(K_n r_0) \ln r_1 - J_0(K_n r_1) \ln r_0]}{\pi K_n^2 J_0(K_n r_0)} - \ln r_0 \left( 2 \frac{J_0(K_n r_0) - J_0(K_n r_1)}{\pi K_n^2 J_0(K_n r_0)} \right) \right\} \right] \right] \end{aligned}$$

The integrals in the second series of the equation for  $T(r, z)$ , for which we will assume linear representations for both  $f_0(z)$  and  $f_1(z)$ , is stated so that

$$\begin{aligned} f_0(z) &= T_0 + (T_{L_0} - T_0) \alpha, \quad \alpha \equiv \frac{z}{L} \\ &= T_0 (1 - \alpha) + \alpha T_{L_0} \end{aligned}$$



and

$$\begin{aligned} f_1(z) &= T_i + (T_{L_i} - T_i) \alpha \\ &= T_i (1 - \alpha) + \alpha T_{L_i} \end{aligned}$$

Also, by using this nomenclature,

$$f_0(L) = T_{L_0}, \quad f_1(L) = T_{L_i}$$

And, evaluating the Fourier coefficient integrals, we obtain

$$\begin{aligned} \int_0^L f_0(z) \sin\left(\frac{n\pi z}{L}\right) dz &= \int_0^L T_0 \left(1 - \frac{z}{L}\right) \sin\left(\frac{n\pi z}{L}\right) dz + \int_0^L T_{L_0} \left(\frac{z}{L}\right) \sin\left(\frac{n\pi z}{L}\right) dz \\ &= \frac{T_0 L}{n\pi} - \frac{T_{L_0} L}{n\pi} \cos(n\pi) = \frac{L}{n\pi} \left[ T_0 - T_{L_0} (-1)^n \right] \end{aligned}$$

and

$$\begin{aligned} \int_0^L f_1(z) \sin\left(\frac{n\pi z}{L}\right) dz &= \int_0^L T_i \left(1 - \frac{z}{L}\right) \sin\left(\frac{n\pi z}{L}\right) dz + \int_0^L T_{L_i} \left(\frac{z}{L}\right) \sin\left(\frac{n\pi z}{L}\right) dz \\ &= \frac{T_i L}{n\pi} - \frac{T_{L_i} L}{n\pi} \cos(n\pi) = \frac{L}{n\pi} \left[ T_i - T_{L_i} (-1)^n \right] \end{aligned}$$

And substituting in the expression for  $T(r, z)$  we will derive the following nomenclature:

$$T(r, z) = \frac{\pi}{\ln\left(\frac{r_1}{r_0}\right)} \sum_{n=1}^{\infty} \left[ \frac{J_0(K_n r_0) u_0(K_n; r; r_0) \sinh(K_n z)}{[J_0^2(K_n r_0) - J_0^2(K_n r_1)] \sinh(K_n L)} \right] \times$$

$$\left[ \left\{ T_{L_0} \ln\left(\frac{r_1}{r_0}\right) (1 + \ln r_0) - T_{L_1} \ln(r_0) \right\} \{ J_0(K_n r_0) - J_0(K_n r_1) \} \right.$$

$$\left. + (T_{L_1} - T_{L_0}) \{ J_0(K_n r_0) \ln r_1 - J_0(K_n r_1) \ln r_0 \} \right]$$

$$+ \frac{2}{L} \sum_{n=1}^{\infty} \frac{\sin\left(\frac{n\pi z}{L}\right)}{G_n(r_1; r_0)} \left\{ G_n(r; r_0) \left(\frac{L}{n\pi}\right) [T_1 - T_{L_1} (-1)^n] + G_n(r_1; r) \left(\frac{L}{n\pi}\right) [T_0 - T_{L_0} (-1)^n] \right\}$$

To determine the total heat loss into the insulation from the specimens it is necessary to evaluate the radial temperature gradient at the surface  $r = r_0$  and perform the integration

$$q_{\text{loss}} = 2 \pi r_0 k_i \int_0^L \left( \frac{\partial T}{\partial r} \right)_{r=r_0} dz$$

where

$k_i$  = insulation thermal conductivity (assumed temperature and position independent in this development)

By writing  $T(r, z)$  in the following abbreviated form,

$$T(r, z) = \frac{\pi}{\ln\left(\frac{r_1}{r_0}\right)} \sum_{n=1}^{\infty} \left[ \xi_n u_0(K_n; r; r_1) \sinh(K_n z) \right] \eta_n$$

$$+ \frac{2}{L} \sum_{n=1}^{\infty} \frac{\sin\left(\frac{n\pi z}{L}\right)}{G_n(r_1; r_0)} \left\{ G_n(r; r_0) \frac{L}{n\pi} [T_1 - T_{L_1} (-1)^n] + G_n(r_1; r) \frac{L}{n\pi} [T_0 - T_{L_0} (-1)^n] \right\}$$

where,

$$\xi_n = J_0(K_n r_0) / \left[ \{ J_0^2(K_n r_0) - J_0^2(K_n r_1) \} \sinh(K_n L) \right]$$

$$\eta_n = T_{L_0} \ln\left(\frac{r_1}{r_0}\right) (1 + \ln r_0) - T_{L_1} \ln r_1 \{ J_0(K_n r_0) - J_0(K_n r_1) \}$$

$$+ (T_{L_1} - T_{L_0}) \{ J_0(K_n r_0) \ln r_1 - J_0(K_n r_1) \ln r_0 \}$$

Differentiating this equation with respect to  $r$  leads to the following:

$$\frac{\partial T(r, z)}{\partial r} = \frac{\pi}{\ln\left(\frac{r_1}{r_0}\right)} \sum_{n=1}^{\infty} \xi_n \eta_n \sinh(K_n z) \cdot \frac{\partial}{\partial r} [u_n(K_n, r; r_1)] \\ + \frac{2}{L} \sum_{n=1}^{\infty} \frac{\partial}{\partial r} \left[ \rho\left(\frac{n\pi r}{L}\right) \right] \sin\left(\frac{n\pi z}{L}\right)$$

And evaluating the differentials,

$$\frac{\partial}{\partial r} [u_n(K_n, r; r_1)] = K_n \left[ Y_0(K_n r_1) \frac{\partial}{\partial r} J_0(K_n r) - J_0(K_n r_1) \frac{\partial}{\partial r} Y_0(K_n r) \right]$$

Since  $K_n$  is a root of  $u_0(K_n, r_0; r_1) = 0$

$$\frac{J_0(K_n r_0)}{J_0(K_n r_1)} = \frac{Y_0(K_n r_0)}{Y_0(K_n r_1)} \equiv \beta$$

then,

$$\frac{\partial}{\partial r} [u_0(K_n, r; r_1)] = K_n \left[ \frac{Y_0(K_n r_0)}{\beta} \frac{\partial}{\partial r} J_0(K_n r) - \frac{J_0(K_n r_0)}{\beta} \frac{\partial}{\partial r} Y_0(K_n r) \right]$$

Evaluating at  $r = r_0$  yields

$$\frac{\partial}{\partial r} [u_0(K_n, r; r_1)]_{r=r_0} = \frac{K_n}{\beta} [Y_0(K_n r_0) J_0'(K_n r_0) - J_0(K_n r_0) Y_0'(K_n r_0)] \\ = \frac{K_n}{\beta} \left[ -\frac{2}{K_n r_0 \pi} \right] = -\frac{2}{\pi r_0} \left[ \frac{J_0(K_n r_1)}{J_0(K_n r_0)} \right]$$

For differentials of terms of the second series in  $T(r, z)$ ,

$$\frac{\partial}{\partial r} G_n(r, r_0) = \left[ \frac{\partial}{\partial r} I_0\left(\frac{n\pi r}{L}\right) \right] K_0\left(\frac{n\pi r_0}{L}\right) - I_0\left(\frac{n\pi r_0}{L}\right) \left[ \frac{\partial}{\partial r} K_0\left(\frac{n\pi r}{L}\right) \right] \\ = \frac{n\pi}{L} \left\{ I_1\left(\frac{n\pi r}{L}\right) K_0\left(\frac{n\pi r_0}{L}\right) + I_0\left(\frac{n\pi r_0}{L}\right) K_1\left(\frac{n\pi r}{L}\right) \right\}$$

Which are defined as

$$G_n'(r, r_0) \equiv I_1\left(\frac{n\pi r}{L}\right) K_0\left(\frac{n\pi r_0}{L}\right) + I_0\left(\frac{n\pi r_0}{L}\right) K_1\left(\frac{n\pi r}{L}\right)$$

then

$$\frac{\partial}{\partial r} G_n(r, r_0) = \frac{n\pi}{L} G_n'(r, r_0)$$

Similarly,

$$\frac{\partial}{\partial r} G_n(r_1; r) = \frac{n\pi}{L} G'_n(r; r_1)$$

where,

$$G'_n(r; r_1) = I_1\left(\frac{n\pi r}{L}\right) K_0\left(\frac{n\pi r_1}{L}\right) + I_0\left(\frac{n\pi r_1}{L}\right) K_1\left(\frac{n\pi r}{L}\right)$$

Combining results gives

$$\begin{aligned} \left[ \frac{\partial T(r, z)}{\partial r} \right]_{r=r_0} &= \frac{\pi}{\ln\left(\frac{r_1}{r_0}\right)} \sum_{n=1}^{\infty} \xi_n \eta_n \sinh(K_n z) \left\{ -\frac{2}{\pi r_0} \left[ \frac{J_0(K_n r_1)}{J_0(K_n r_0)} \right] \right\} \\ &+ \frac{2}{L} \sum_{n=1}^{\infty} \left\{ \frac{G'_n(r_0; r_0)}{G_n(r_1; r_0)} [T_1 - T_{L_1} (-1)^n] + \frac{G'_n(r_0; r_1)}{G_n(r_1; r_0)} [T_0 - T_{L_0} (-1)^n] \sin\left(\frac{n\pi z}{L}\right) \right\} \end{aligned}$$

Integrating with respect to Z to determine  $q_{\text{loss}}$  producer

$$\begin{aligned} q_{\text{loss}} &= 2\pi r_0 k_i \int_0^L \left( \frac{\partial T}{\partial r} \right)_{r=r_0} dz = \\ &2\pi r_0 k_i \left\{ 2 \sum_{n=1}^{\infty} \left[ \frac{G'_n(r_0; r_0)}{G_n(r_1; r_0)} \{T_1 - T_{L_1} (-1)^n\} + \frac{G'_n(r_0; r_1)}{G_n(r_1; r_0)} \{T_0 - T_{L_0} (-1)^n\} \right] \left\{ \frac{1 - (-1)^n}{n\pi} \right\} \right. \\ &\left. - \frac{2}{r_0 \ln\left(\frac{r_1}{r_0}\right)} \sum_{n=1}^{\infty} \xi_n \eta_n \frac{J_0(K_n r_1)}{J_0(K_n r_0)} \left[ \frac{\cosh(K_n L) - 1}{K_n} \right] \right\} \end{aligned}$$

Alternate terms of the first summation are zero due to the factor  $[1 - (-1)^n]$ .

Thus, only odd values of n need be considered in this summation.

In the second summation, determination of the eigenvalues,  $K'_n$ , is necessary. These values were defined by the condition

$$J_0(K_n r_0) Y_0(K_n r_1) - J_0(K_n r_1) Y_0(K_n r_0) = 0$$

For the experimental arrangement used here,

$$\frac{r_1}{r_0} = 6$$

thus the above equation can be rewritten in terms of  $r_0$  to read

$$J_0(K_n r_0) Y_0(6 K_n r_0) - J_0(6 K_n r_0) Y_0(K_n r_0) = 0$$

Roots of this equation for low values of  $r_1/r_0$  have been tabulated (Reference 35). For the case considered here, the following expansion may be used in evaluating the  $n^{\text{th}}$  root (Reference 36):

$$r_0 K_n = \delta + \frac{\rho}{\delta} + \frac{q - \rho^2}{\delta^3} + \frac{r - 4\rho q + 2\rho^3}{\delta^5} + \dots$$

where

$$\rho = \frac{r_1}{r_0}, \quad \delta = \frac{n\pi}{\rho - 1}, \quad \rho = -\frac{1}{8\rho}$$

$$q = \frac{100(\rho^3 - 1)}{3(8\rho)^3(\rho - 1)}, \quad r = \frac{(32)(1073)(\rho^5 - 1)}{5(8\rho)^5(\rho - 1)}$$

The results are given in Table I.

Finally, the evaluation of  $q_{\text{loss}}$  requires the experimental temperature distribution data. This data obtained directly from analysis of measured temperature distributions is as follows:

TABLE XI  
BeO THERMAL CONDUCTIVITY GUARDING DATA

Data Point	$T_{L_1}$	$T_1$	$T_{L_0}$	$T_0$	$\bar{T}_1$	$\bar{k}_1$
2	221.3	112.3	165.2	82.5	166.8	0.08
4	293.0	131.5	249.0	111.0	212.3	0.10
10	687.0	359.5	748.0	165.0	523.3	0.18
11	819.3	421.2	936.0	177.0	620.3	0.21
12	894.2	458.8	950.0	188.0	676.5	0.23
13	988.2	494.8	972.0	194.0	741.6	0.26
14	1060.0	508.5	1215.0	188.0	784.3	0.29
16	1204.2	533.2	1537.0	114.0	863.2	0.33
19	1333.8	541.2	1910.0	60.0	937.5	0.38

Physically, the surface  $r_0 \leq r \leq r_1, z=0$  can be assumed to be at the temperature  $f_0(0) = T_0$ . Since in the derivation, it was assumed that this surface was at zero (original B.C. 3), the temperature in the above table must be adjusted to this base.

The adjustment has no effect on the calculation so long as the values of  $\bar{k}_i$  are consistently retained.

TABLE XII  
ADJUSTED TEMPERATURE DISTRIBUTION DATA

Data Point	$T_{L_1}$	$T_1$	$T_{L_0}$	$T_0$	$\bar{k}_i$
2	138.0	29.8	82.7	0.0	0.08
4	172.0	20.5	138.0	0.0	0.10
10	522.0	194.5	583.0	0.0	0.18
11	642.3	244.2	759.0	0.0	0.21
12	706.2	270.8	762.0	0.0	0.23
13	794.3	300.8	778.0	0.0	0.26
14	872.0	320.5	1027.0	0.0	0.29
16	1090.2	419.2	1423.0	0.0	0.33
19	1273.8	481.2	1850.0	0.0	0.38

The final form of the equation for computer solution is then:

$$\begin{aligned}
 q_{\text{loss}} = & 2 \pi r_0 \bar{k}_i \left[ \frac{4}{\pi} (T_i + T_{L_1}) \sum_{n=1}^{\infty} \frac{G'_n(r_0; r_0)}{n G_n(r_1; r_0)} + \frac{4}{\pi} (T_{L_0}) \sum_{n=1}^{\infty} \frac{G'_n(r_0; r_1)}{n G_n(r_1; r_0)} \right. \\
 & n = 1, 3, 5, \dots \\
 & - \frac{2}{r_0 \ln\left(\frac{r_1}{r_0}\right)} \sum_{n=1}^{\infty} \frac{1}{[J_0^2(K_n r_0) - J_0^2(K_n r_1)] \sinh(K_n L)} \left\{ [T_{L_0} (1 + \ln r_0) - T_{L_1} \ln r_0] [J_0(K_n r_0) - J_0(K_n r_1)] \right. \\
 & \left. + (T_{L_1} - T_{L_0}) [J_0(K_n r_0) \ln r_1 - J_0(K_n r_1) \ln r_0] \right\} J_0(K_n r_1) \left\{ \frac{\cosh(K_n L) - 1}{K_n} \right\} \left. \right] \\
 & n = 1, 2, 3, \dots
 \end{aligned}$$



## APPENDIX II

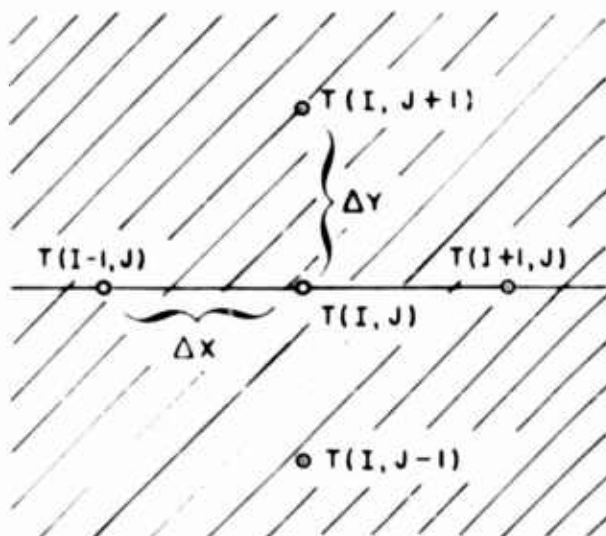
### FINITE ELEMENT ANALYSIS

#### A. NODAL EQUATION DERIVATIONS

The following paragraphs give the derivation of equations for each nodal type depicted in Figure 32; the nomenclature used follows that given in this figure.

##### 1. Internal Nodes:

The internal nodes can be represented as sketched at the right.



The equations for the heat flux in each direction are written

$$q_{\text{from } I, J+1} = \frac{k}{\Delta y} [T(I, J+1) - T(I, J)] \Delta x$$

$$q_{\text{from } I, J-1} = \frac{k}{\Delta y} [T(I, J-1) - T(I, J)] \Delta x$$

$$q_{\text{from } I+1, J} = \frac{k}{\Delta x} [T(I+1, J) - T(I, J)] \Delta y$$

$$q_{\text{from } I-1, J} = \frac{k}{\Delta x} [T(I-1, J) - T(I, J)] \Delta y$$

Summing, we get

$$\frac{k\Delta x}{\Delta y} [T(I, J+1) + T(I, J-1) - 2T(I, J)] + k \frac{\Delta y}{\Delta x} [T(I+1, J) + T(I-1, J) - 2T(I, J)]$$

If

$$\Delta x = \Delta y = \ell$$

$$T(I, J+1) + T(I, J-1) + T(I+1, J) + T(I-1, J) - 4[T(I, J)] = 0$$

## 2. Nodes Along Lines of Temperature Symmetry

The centerline of the conducting element ( $I = 1, J$ ) was assumed to be a line of temperature symmetry and, thus, it can be assumed that,

$$T(I+1, J) = T(I-1, J)$$

From the result for the previous case it can be seen by inspection that

$$T(I, J+1) + T(I, J-1) + T(I+1, J) + T(I-1, J) - 4[T(I, J)] = 0$$

or

$$T(I, J) = \frac{1}{4} [T(I, J+1) + T(I, J-1) + 2T(I+1, J)]$$

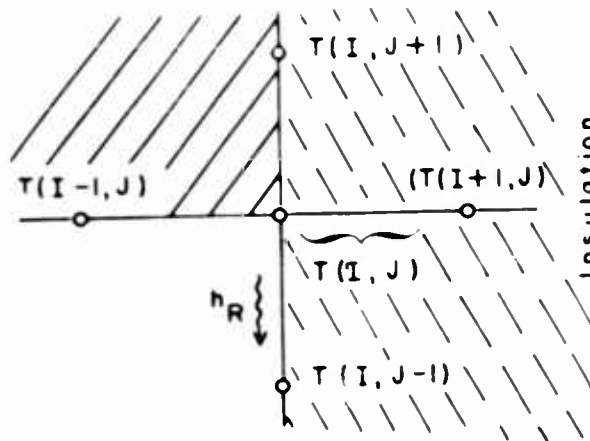
The surface  $I = 9, J \geq 2$ , is an adiabatic boundary and thus can also be assumed to be a line of temperature symmetry. In this case the nodal equation will be of the form

$$T(I, J) = \frac{1}{4} [T(I, J+1) + T(I, J-1) + 2T(I-1, J)]$$

## 3. External Corner Node

From Figure 32 we see that the external corner node occurs at the position  $I = 9, J = 2$ . An expanded view of this node and definition of appropriate nomenclature are given below. The radiation heat transfer coefficient,  $h_R$  is defined by

$$h_R = \frac{q_{\text{radiation}}}{\Delta T}$$



An explicit relationship for  $h_R$  will be given later. By writing the heat flux equations about this node, we obtain

$$q)_{from\ I, J-1} = h_R [T(I, J-1) - T(I, J)] \Delta x$$

$$q)_{from\ I, J+1} = \frac{k}{\Delta y} [T(I, J+1) - T(I, J)] \Delta x$$

$$q)_{from\ I+1, J} = \frac{k}{\Delta x} [T(I+1, J) - T(I, J)] \frac{\Delta y}{2}$$

$$q)_{from\ I-1, J} = \frac{k}{\Delta x} [T(I-1, J) - T(I, J)] \frac{\Delta y}{2}$$

Since the surface  $I = 3, J$ , is insulated,

$$T(I-1, J) = T(I+1, J)$$

Summing the heat fluxes yields

$$\begin{aligned} h_R \Delta x [T(I, J-1) - T(I, J)] + \frac{k \Delta x}{\Delta y} [T(I, J+1) - T(I, J)] \\ + 2 \left( \frac{k}{\Delta x} \cdot \frac{\Delta y}{2} \right) [T(I-1, J) - T(I, J)] = 0 \end{aligned}$$

Simplifying, we get

$$T(I, J) = \left\{ \frac{T(I-1, J)\Delta Y^2 + T(I, J+1)\Delta X^2 + \frac{h_R}{k} \Delta X^2 \Delta Y T(I, J-1)}{[\Delta X^2 + \Delta Y^2 + \frac{h_R}{k} \Delta X^2 \Delta Y]} \right\}$$

Since

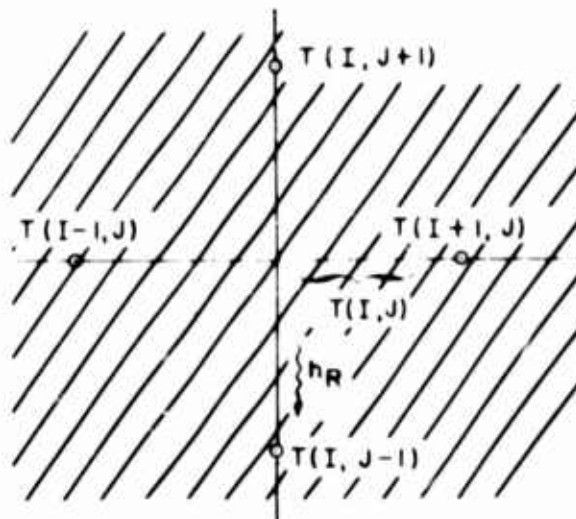
$$\Delta X = \Delta Y = \ell \quad \text{then}$$

$$T(I, J) = \frac{T(I-1, J) + T(I, J+1) + \frac{h_R \ell}{k} T(I, J-1)}{[2 + \frac{h_R \ell}{k}]}$$

#### 4. Internal Corner Node

Referring again to Figure 32 we see that an internal corner node occurs at  $I = 4$ ,

$J = 2$ . Definition of terms for this node are below.



The heat flux equations about this node are written as follows:

$$q_{\text{from } T(I-1, J)} = \frac{k}{\Delta X} [T(I-1, J) - T(I, J)] \Delta Y$$

$$q)_{from\ I+1,J} = \frac{k}{\Delta x} [T(I+1,J) - T(I,J)] \frac{\Delta y}{2}$$

$$q)_{from\ I,J+1} = \frac{k}{\Delta y} [T(I,J+1) - T(I,J)] \Delta x$$

$$q)_{from\ I,J-1} = h_R [T(I,J-1) - T(I,J)] \frac{\Delta x}{2} + \frac{k}{\Delta y} [T(I,J-1) - T(I,J)] \frac{\Delta x}{2}$$

Summing produces

$$\begin{aligned} & \frac{k\Delta y}{\Delta x} [T(I-1,J) - T(I,J)] + \frac{k\Delta y}{2\Delta x} [T(I+1,J) - T(I,J)] + \frac{k\Delta x}{\Delta y} [T(I,J+1) - T(I,J)] \\ & + \frac{h_R \Delta x}{2} [T(I,J-1) - T(I,J)] + \frac{k\Delta x}{2\Delta y} [T(I,J-1) - T(I,J)] = 0 \end{aligned}$$

Simplifying gives

$$T(I,J) = \left\{ \frac{[2T(I-1,J) + T(I+1,J)]\Delta y^2 + [2T(I,J+1) + T(I,J-1)]\Delta x^2 + \frac{h_R \Delta x^2 \Delta y}{k} T(I,J-1)}{3[\Delta x^2 + \Delta y^2] + \frac{h_R}{k} [\Delta x^2 \Delta y]} \right\}$$

And, since

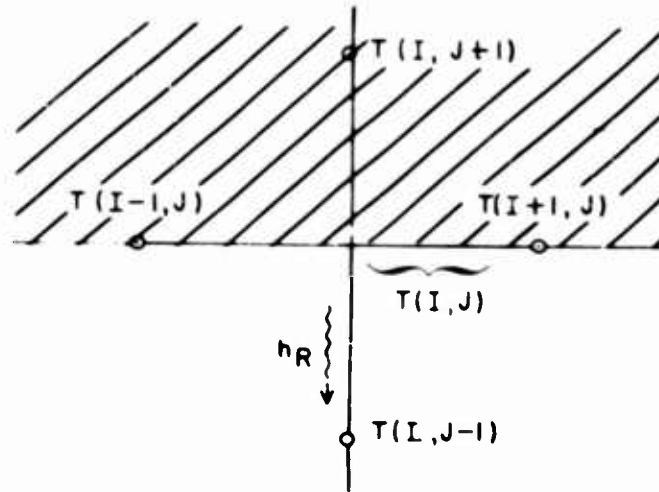
$$\Delta x = \Delta y = \ell, \text{ then}$$

$$T(I,J) = \frac{2[T(I-1,J) + T(I,J+1) + T(I+1,J) + T(I,J-1)] + \frac{h_R \ell}{k} T(I,J-1)}{6 + \frac{h_R \ell}{k}}$$

## 5. Radiation Nodes

Radiation nodes occur at positions,  $I = 5-8$ ,  $J = 2$ , and are characterized by radiation heat transfer only in the  $y$ -direction from the surface  $J = 2$  to the constant

temperature surface  $J = 1$ . A sketch of the heat transfer paths is given below.



The flux equations are:

$$q)_{\text{from } I, J+1} = \frac{k}{\Delta Y} [T(I, J+1) - T(I, J)] \Delta X$$

$$q)_{\text{from } I, J-1} = h_R [T(I, J-1) - T(I, J)] \Delta X$$

$$q)_{\text{from } I-1, J} = \frac{k}{\Delta X} [T(I-1, J) - T(I, J)] \frac{\Delta Y}{2}$$

$$q)_{\text{from } I+1, J} = \frac{k}{\Delta X} [T(I+1, J) - T(I, J)] \frac{\Delta Y}{2}$$

Summing, we get

$$\begin{aligned} \frac{k \Delta X}{\Delta Y} [T(I, J+1) - T(I, J)] + \frac{k \Delta Y}{2 \Delta X} [T(I-1, J) - T(I+1, J) - 2T(I, J)] \\ + h_R \Delta X [T(I, J-1) - T(I, J)] = 0 \end{aligned}$$

or

$$T(I, J) = \frac{[T(I-1, J) + T(I+1, J)] \Delta Y^2 + 2T(I, J+1) \Delta X^2 + \frac{2h_R \Delta X^2 \Delta Y}{k} T(I, J-1)}{[2(\Delta X^2 + \Delta Y^2) + \frac{2h_R \Delta X^2 \Delta Y}{k}]}$$

Since

$$\Delta x = \Delta y = \ell$$

$$T(I, J) = \frac{T(I-1, J) + T(I+1, J) + 2T(I, J+1) + \frac{2h_R \ell}{k} T(I, J-1)}{4 + \frac{2h_R \ell}{k}}$$

## 6. Heat Transfer Coefficient Formulation

From the definition of  $h_R$  as  $q_R / \Delta T$ , it follows that,

$$h_R = \frac{q_R}{\Delta T} = \mathcal{F}_0 \mathcal{F}_\epsilon \sigma (T_1^4 - T_0^4) / (T_1 - T_0)$$

where

$\mathcal{F}_0$  = geometrical view factor

$\mathcal{F}_\epsilon$  = emittance view factor

$T_1, T_0$  = temperatures of radiation surfaces,

Setting  $T_1 = T_0 + \Delta T$  we then have

$$\begin{aligned} [T_1^4 - T_0^4] &= [(T_0 + \Delta T)^4 - T_0^4] \\ &= 4T_0^3 \Delta T + 6T_0^2 \Delta T^2 + 4T_0 \Delta T^3 + \Delta T^4 \end{aligned}$$

We can write

$$\Delta T = (T_1 - T_0)$$

and simplify the above to

$$\frac{[T_1^4 - T_0^4]}{\Delta T} = T_0^3 + T_0^2 T_1 + T_0 T_1^2 + T_1^3$$

Thus,

$$h_R = \frac{q}{\Delta T} \mathcal{F}_0 \mathcal{F}_\epsilon \sigma (T_1^3 + T_1^2 T_0 + T_1 T_0^2 + T_0^3)$$

Table VI gives a summary of the necessary nodal equations derived above.

## B. NUMERICAL EVALUATION

The table below gives a "first-guess" temperature distribution based on the flux pattern depicted in Figure 31, assuming that the surfaces I, J = 1, and I, J = 8, are fixed temperature planes at 500 and 1500° C, respectively.

TABLE XIII  
"FIRST GUESS" TEMPERATURE DISTRIBUTION

Node	1500	1500	1500	1500	1500	1500	1500	1500	1500
8	1500	1500	1500	1500	1500	1500	1500	1500	1500
7	1400	1400	1400	1400	1400	1400	1400	1400	1400
6	1300	1300	1300	1300	1300	1300	1300	1300	1300
5	1200	1200	1200	1200	1200	1200	1200	1200	1200
4	1050	1060	1070	1080	1090	1100	1110	1120	1130
3	880	890	900	920	950	980	1010	1040	1070
2	700	710	720	740	790	840	900	960	1020
1	500	500	500	500	500	500	500	500	500
J/I	1	2	3	4	5	6	7	8	9 Node

Assigning a quantitative geometrical size to the nodal grid (i.e., defining the magnitude of  $\ell$  in the case where  $\Delta x = \Delta y$ ) is dependent on the magnitude of the heat flux expected for the assumed overall temperature drop:

$$\Delta T = 1500 - 500 = 1000^\circ \text{F.}$$

Our experimental data has shown that a heat flux of  $q/A = 30,000 \text{ BTU/hr-ft}^2$  is a typical value. If we assume a mean conductivity value of  $400 \text{ BTU-in/hr-ft}^2\text{-}^\circ \text{F}$ , which was observed experimentally for BeO at  $1000^\circ \text{F}$ , the following equation results,

$$\Delta y = \Delta x = 7\ell = \frac{k \Delta T}{(q/A)} = \frac{(400)(1000)}{30,000} = 13.3 \text{ in}$$

$$\ell \cong 2.0 \text{ in}$$



Assuming a total hemispherical emittance of  $\epsilon = 0.3$  for BeO will define the following emittance shape factor:

$$F_{\epsilon} = \frac{1}{\left[\frac{2}{\epsilon} - 1\right]} = 0.18$$

For this calculation it will be assumed that  $F_0 = 1.0$ . Since  $T_0 = 500^\circ \text{F} = 960^\circ \text{R}$  and  $T_1$  is a variable, the final equation for  $h_R$  becomes

$$h_R = f(T_1) = \left\{ 3.33 \times 10^{-10} T_1^3 + 3.20 \times 10^{-7} T_1^2 + 3.07 \times 10^{-4} T_1 + 0.294 \right\}$$

Inserting numerical values for  $\ell$ ,  $k$ , and  $T$  ( $I = 1, 8, J = 1$ ) =  $500^\circ \text{F}$  into the appropriate nodal equations leads to the set of equations displayed in Table XIV for computer evaluation:

TABLE XIV  
NODAL EQUATIONS FOR COMPUTER EVALUATION

Type	Nodal Equation
Internal	Same as Table VI
Line of Symmetry	Same as Table VI
Internal Corner	$T(I, J) = \frac{2 \left[ T(I-1, J) + T(I, J+1) \right] + T(I+1, J) + T(I, J-1) + 2.5 h_R}{6.0 + 0.005 h_R}$
External Corner	$T(I, J) = \frac{T(I-1, J) + T(I, J+1) + 2.5 h_R}{2.0 + 0.005 h_R}$
Radiation	$T(I, J) = \frac{T(I-1, J) + T(I+1, J) + 2T(I, J+1) + 5.0 h_R}{4.0 + 0.01 h_R}$
Heat Transfer Coefficient	$h(I, J) = 3.33 \times 10^{-10} T^3 + 3.20 \times 10^{-7} T^2 + 3.07 \times 10^{-4} T + 0.294$

### APPENDIX III

#### PHYSICAL PROPERTY DATA

##### A. THERMAL CONDUCTIVITY OF THE ALUMINA BUBBLE INSULATION

To determine the heat exchange between the specimen column and the alumina bubble insulation using Equation 22, it was necessary to have values of the insulation conductivity. This conductivity was not measured in the investigation; thus, it was necessary to estimate values from data in the literature.

Literature data on alumina powders are reported for a range of densities and particle sizes. Extrapolation of the data to other ranges of density or particle size is not straightforward because of the high radiative contribution to the total thermal conductivity. The data of Laubitz (Reference 37) was found to be particularly useful since the solid conduction and radiation contributions to the effective conductivity were presented separately as a function of temperature. Further, the data were found to be consistent with other alumina powder data in the same density and particle size range (References 38 and 39).

The results of Laubitz, measured in vacuum, on a powder with density of  $1.77 \text{ gms/cm}^3$  and particle sizes in the range 300-420 is given as curve (1) in Figure 41. This particle size range encompasses the average particle diameter of the alumina bubbles used here  $\bar{d} = 396 \mu$ . The alumina bubbles have a lower density, however, the average value being  $1.01 \text{ gms/cm}^3$ . The bubbles are hollow but since the radiative contribution is essentially size dependent (See Equation 2 of Reference 37), it was assumed that this contribution was the same as that inferred by Laubitz for material having the same particle size range as the alumina bubbles (curve (2), Figure 41). The solid conduction contribution for the alumina bubbles was calculated by reducing that measured by Laubitz in the ratio  $1.01/1.77$ . The estimated effective conductivity for the alumina bubbles, found by adding the conductive and radiative contributions, is given as curve (3) in Figure 41. That this curve is of the right order of magnitude is demonstrated by the dotted curve in the figure. This curve gives vacuum environment conductivity results by Wechsler and Glaser (Reference 40) for an alumina bubble/graphite fiber composite.

Data points taken from curve (3) are tabulated in Table XI, Appendix I, where they were used in calculating the heat exchange between the specimen column and the insulation.

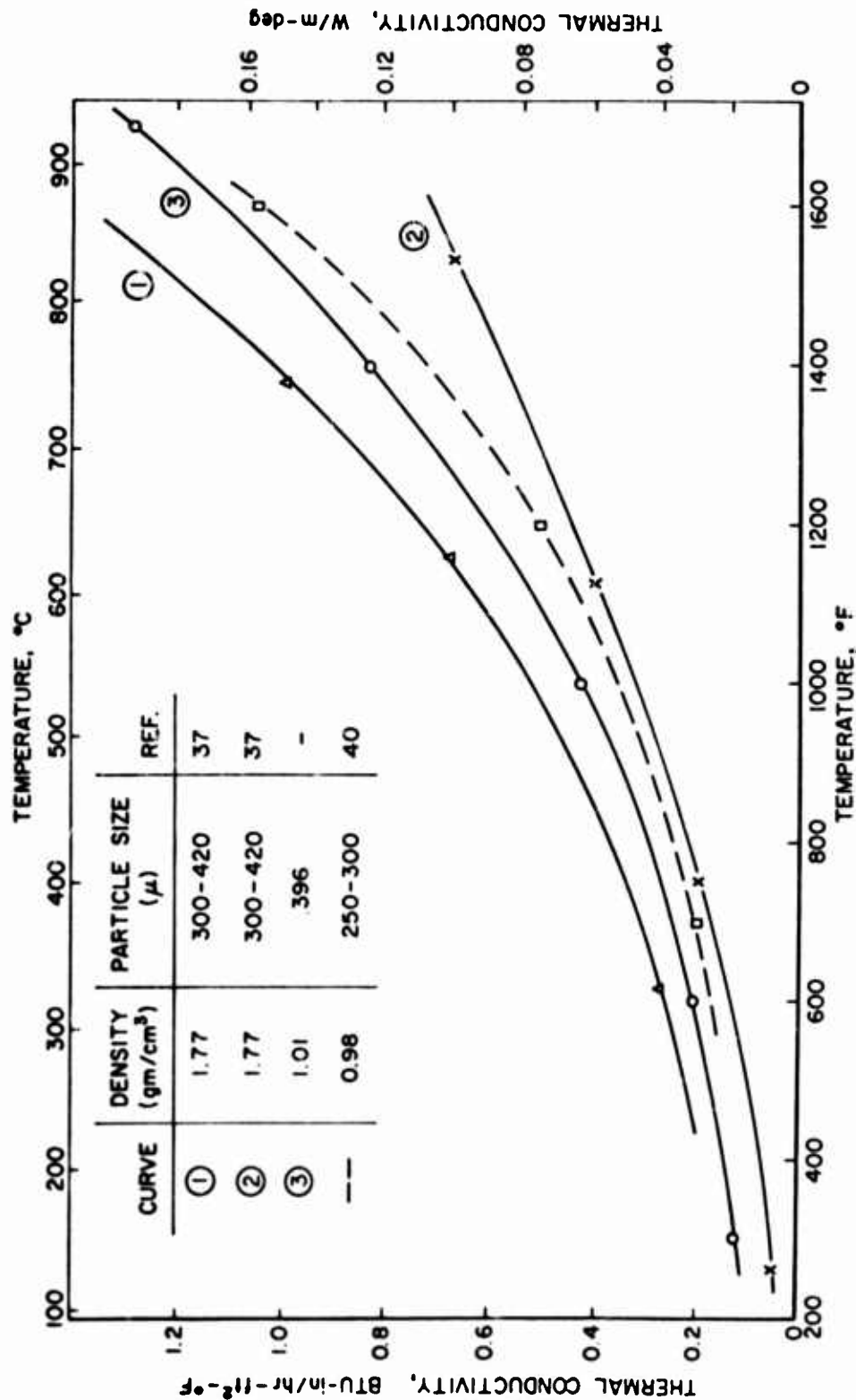


Figure 41. Thermal Conductivity of Aluminum Oxide Powder Insulations

## B. BERYLLIUM OXIDE EMITTANCE DATA

Total hemispherical emittance data is required in the evaluation of the emissivity shape factor, Equation 33. To provide this data spectral normal emittance measurements were run on beryllium oxide disks using the equipment and methods described in Reference 30. A ratio recording Perkin-Elmer model 13 U spectrophotometer was used in double beam mode. The basic measurement consisted of a comparison between the emissive power of the BeO specimen surface and the emissive power of a blackbody reference cavity at the same temperature. Systems calibrations were performed with National Bureau of Standards reference standards. A sodium chloride prism was used to obtain spectral normal emittance data over the range from 1.8 to 14 microns. The results at a specimen temperature of 980° F are shown in Figure 42 for two BeO specimens of different surface roughness and density. The specimen of higher surface roughness has higher spectral emittance, particularly in the region where the absorption coefficient is high (4 to 9  $\mu$ ), and where emission is predominately a surface phenomenon. This behavior is consistent with the expected phenomenon in the geometrical optics regime: increased emittance with increased surface roughness. Also, the data is typical of a dielectric material in the infrared and compares favorably with other published data on the spectral emittance of beryllium oxide (Reference 41).

The spectral data was converted to total normal emittance form by use of the following equation,

$$\epsilon_{TN} = \frac{\int_0^{\infty} \epsilon_{\lambda N} E_{BB}(\lambda) d\lambda}{\int_0^{\infty} E_{BB}(\lambda) d\lambda} \cong \frac{\sum_{\lambda_1}^{\lambda_2} \epsilon_{\lambda N} E_{BB} \Delta\lambda}{\sum_{\lambda_1}^{\lambda_2} E_{BB} \Delta\lambda}$$

Numerical integration was performed using the spectral data in Figure 42,  $\epsilon_{\lambda N} = f(\lambda)$ , and blackbody emissive power curves calculated from the universal Planckian distribution given in Reference 32. To obtain an  $\epsilon_{TN}$  value at a given temperature, the blackbody distribution at that temperature is used in the above equation. Since the  $\epsilon_{\lambda N}$  curves were obtained at a constant temperature of 980° F it is implicitly assumed that the spectral emittance of BeO is not strongly temperature dependent. Experimental evidence available (References 41 and 42) indicates that the spectral emittance is nearly temperature independent and thus the evaluation procedure is correct. The final results of the numerical integrations are presented in Figure 43 as  $\epsilon_{TN}$  versus T. Literature data on similar BeO materials

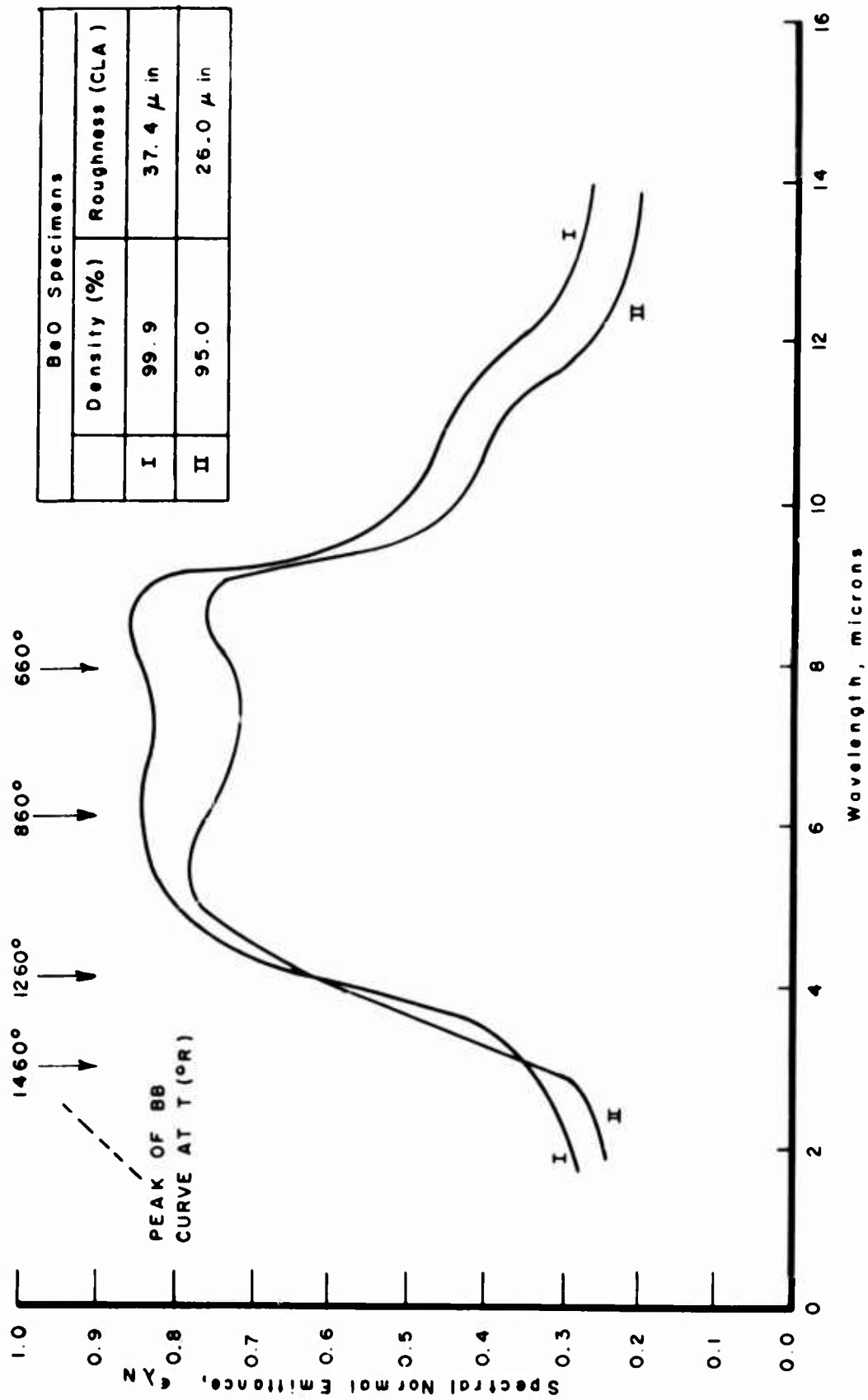


Figure 42. Spectral Normal Emittance of Beryllium Oxide in the Infrared

is also presented in this figure. As the temperature increases, the total normal emittance would be expected to decrease, because the blackbody curve is shifting toward shorter wavelengths as indicated in Figure 42, weighing the spectral data in the 1 to 4 micron range more heavily.

A small correction is required to convert total normal to total hemispherical emittance for this dielectric material, which has a zero absorption index. The correction curve given by Dunkle (Reference 43) was used to produce final  $\epsilon_{TH}$  curves. The equation of the mean curve used in the computer evaluation of Equation 33 was as follows:

$$\underline{200^{\circ} \text{ F} \leq T \leq 700^{\circ} \text{ F}}$$

$$\epsilon_{TH} = 0.650 - (T-200) (0.000023)$$

$$\underline{700^{\circ} \text{ F} < T \leq 2000^{\circ} \text{ F}}$$

$$\epsilon_{TH} = 0.639 - (T-700) (0.0000129)$$

The characteristics of the BeO specimens on which total normal emittance literature data is reported in Figure 43 are summarized in Table XV. There is no clear rationale for the wide disparity in results, although, for dielectric materials, both surface and volume emission are important over fairly narrow wavelength intervals. This implies that the total emittance will be a strong function of specimen surface finish, chemical purity, and density. The influence of density is particularly important for near-theoretical density materials, since the porosity (and, in turn, the effective optical scattering cross section) changes rapidly in this range. From the characterization information available in the literature, it is clear that the results presented in Figure 43 are on BeO materials of widely differing character. Incompleteness of the supporting data prevents quantitative rationalization of these differences.

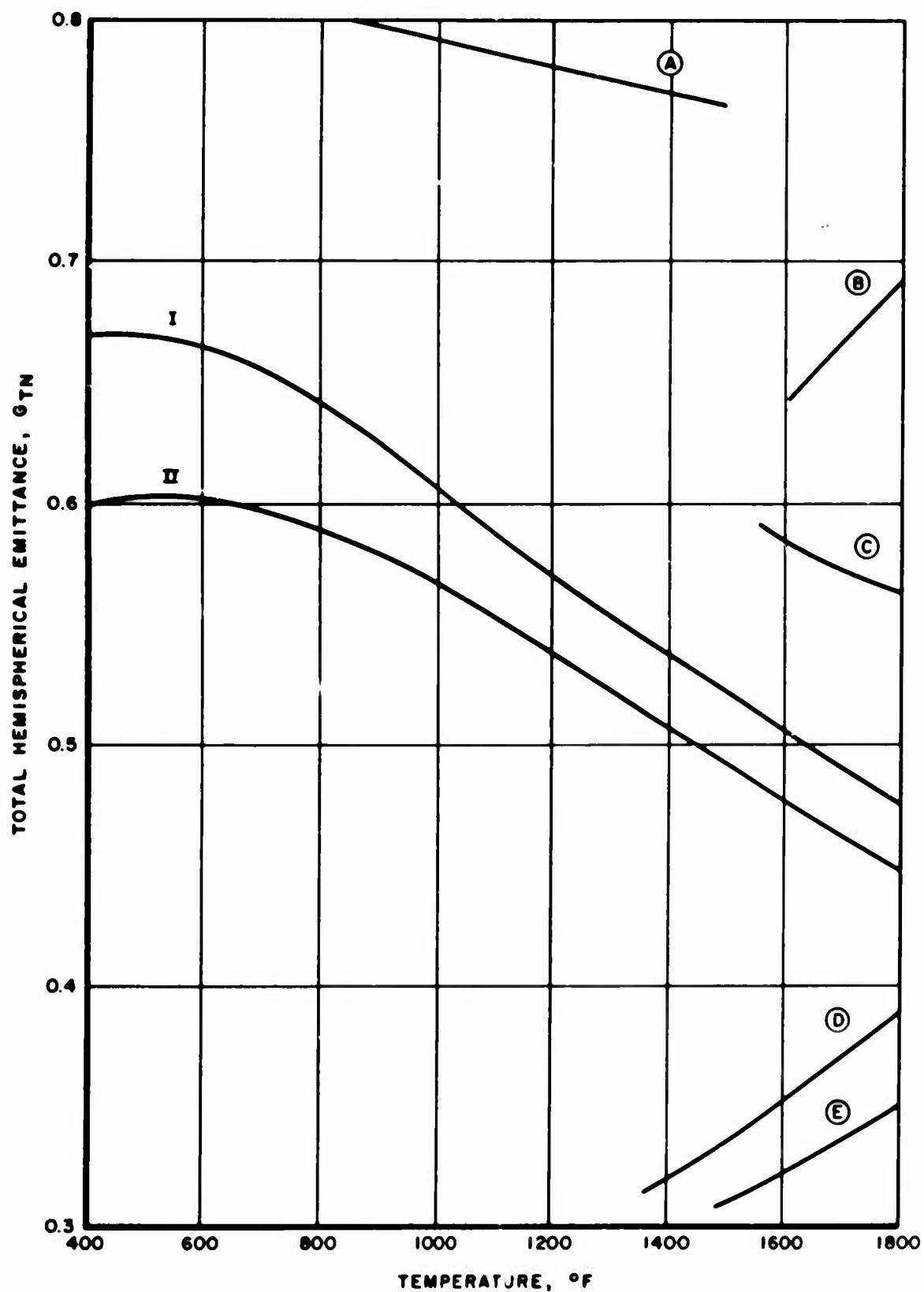


Figure 43. Total Normal Emittance of Beryllium Oxide as a Function of Temperature

TABLE XV  
BERYLLIUM OXIDE EMITTANCE SPECIMEN CHARACTERISTICS

Curve	Density	Purity	Other Characteristics	Ref.
A	--	--	Meas. in Air	44
B	2.844	S. P. Powder	Grey Inclusions, Mea. in Vacuum Hot Pressed, Polished	45
C	3.0	--	Sintered Meas. in Argon	46
D	2.778	S. P. Powder	Hot pressed, Air Fired Meas. in Vacuum	10
E	2.88	99.5	Sintered, Meas. in Vacuum	10



## APPENDIX IV

## TABULATED EXPERIMENTAL DATA

## A. BERYLLIUM OXIDE THERMAL CONDUCTIVITY DATA

The thermal conductivity data given below was obtained by comparing the temperature gradients in the Armco iron meter bars with the temperature gradient in the beryllium oxide specimen (Figure 9). Since the conductivity of the Armco iron is known accurately, the following equation can be used to calculate the BeO conductivity. The  $k_{upper}$  and  $k_{lower}$  values for the BeO were determined using the temperature gradient in the upper and lower Armco Iron specimen, respectively.

$$K_{BeO} = K_{AI} \left[ (\Delta T / \Delta x)_{AI} / (\Delta T / \Delta x)_{BeO} \right]$$

All conductivity values have the units BTU-in./hr-ft<sup>2</sup>·°F. The  $k$  column is the arithmetic average of the previous columns.

TABLE XVI

## BeO THERMAL CONDUCTIVITY RESULTS

Data Point	Mean Temperature, °F	$k_{upper}$	$k_{lower}$	$\bar{k}_{BeO}$
1	97.3	1584.0	1602.0	1593.0
2	129.1	1522.0	1444.0	1483.0
3	156.9	1478.0	1397.0	1437.5
4	181.3	1353.0	1322.0	1337.5
5	235.2	1206.0	1168.0	1187.0
6	296.2	1167.0	1106.0	1136.5
7	364.9	1032.0	973.0	1002.5
8	403.7	979.0	930.0	954.5
9	501.1	818.5	775.0	796.8
10	602.5	716.5	673.5	695.0
11	618.3	679.0	642.5	660.8
12	634.2	652.5	630.0	641.3
13	758.9	559.0	535.5	547.3
14	860.9	512.5	471.5	492.0
15	933.1	431.0	434.0	432.5
16	979.4	400.0	411.5	405.8
17	1032.3	370.0	389.0	379.5
18	1115.9	340.8	360.2	350.5
19	718.7	520.0	566.5	543.3
20	562.2	656.0	697.5	676.8
21	565.4	673.5	701.0	687.3
22	248.5	1088.0	1098.0	1093.0

## B. TANTALUM THERMAL CONDUCTIVITY DATA

The tantalum data given in Table XVII was obtained in the same manner as that described for the beryllium oxide.

TABLE XVII  
TANTALUM THERMAL CONDUCTIVITY RESULTS

Data Point	Mean Temperature, ° F	$k_{upper}$	$k_{lower}$	$\bar{k}_{Ta}$
1	125.6	371.4	412.2	391.8
2	203.2	386.5	424.5	405.5
3	206.0	371.5	426.3	398.9
4	300.5	384.0	421.7	402.9
5	386.6	391.2	415.7	403.5
6	523.2	391.5	407.4	399.5
7	689.4	385.5	392.9	389.2
8	837.1	395.0	397.3	396.2
9	1065.4	382.1	396.8	389.5

## C. THERMAL CONTACT RESISTANCE DATA

Tables XVIII through XXVII give the tabular experimental data obtained on this program during the contact resistance measurements. The second column of each table gives the interfacial temperature drop. The next two columns give the heat flux in the specimens above and below the interface, respectively, while the following two columns give the corresponding thermal contact conductance values. The next column gives the mean interface temperature. The last column is the average thermal contact conductance calculated as the arithmetic mean of the conductance values in the previous columns.

TABLE XVIII

THERMAL CONTACT CONDUCTANCE RESULTS -  $40\ \mu$  in. /  $40\ \mu$  in.  
INTERFACE: 5.02 psia COMPRESSIVE LOAD

Data Point	$\Delta T_c$ °F	$(q/A)_A$ $\frac{\text{BTU}}{\text{hr-ft}^2}$	$(q/A)_B$ $\frac{\text{BTU}}{\text{hr-ft}^2}$	$(h_c)_A$ $\frac{\text{BTU}}{\text{hr-ft}^2\text{-}^\circ\text{F}}$	$(h_c)_B$ $\frac{\text{BTU}}{\text{hr-ft}^2\text{-}^\circ\text{F}}$	$T_m$ °F	$(h_c)_m$ $\frac{\text{BTU}}{\text{hr-ft}^2\text{-}^\circ\text{F}}$
1	140.3	3,040	2,980	21.7	21.2	253.0	21.5
2	166.2	3,810	4,320	22.9	26.0	353.2	23.6
3	198.1	4,610	5,280	23.3	26.7	404.0	23.4
4	261.7	5,865	5,025	22.4	19.2	505.3	18.6
5	312.1	5,860	6,620	18.8	21.2	574.0	19.8
6	394.9	7,280	8,460	18.5	21.4	722.5	19.4
7	409.8	7,900	9,390	19.3	22.9	809.0	21.0
8	412.6	8,640	9,770	20.9	23.7	802.5	22.3
9	466.8	8,720	9,260	18.7	19.8	872.9	19.2
10	445.1	8,900	10,450	20.0	23.5	878.3	22.4
11	579.9	10,000	10,450	17.2	18.0	1052.6	18.5
12	565.4	11,780	9,860	20.9	17.4	1119.0	19.9
13	574.5	11,670	8,990	20.3	15.6	1122.3	18.5
14	604.5	14,520	10,840	24.0	17.9	1293.8	21.4
15	618.4	16,930	12,900	27.4	20.8	1410.5	24.5
16	587.1	16,400	12,500	28.0	21.3	1462.5	25.0

TABLE XIX

THERMAL CONTACT CONDUCTANCE RESULTS -  $40\mu$  in./ $40\mu$  in.  
INTERFACE: 65.2 psia COMPRESSIVE LOAD

Data Point	$\Delta T_c$ °F	$(q/A)_A$ BTU hr-ft <sup>2</sup>	$(q/A)_B$ BTU hr-ft <sup>2</sup>	$(h_c)_A$ BTU hr-ft <sup>2</sup> -°F	$(h_c)_B$ BTU hr-ft <sup>2</sup> -°F	$T_m$ °F	$(h_c)_m$ BTU hr-ft <sup>2</sup> -°F
1	122.9	9,080	6,050	73.9	49.2	240.2	72.23
2	157.4	12,620	10,930	80.3	69.7	302.6	74.20
3	260.6	19,970	11,590	76.7	44.4	464.5	68.23
4	270.4	21,300	18,930	78.7	70.0	597.4	73.40
5	342.9	23,400	26,400	68.2	74.1	647.9	65.40
6	426.2	26,950	35,550	63.3	83.3	832.5	63.80
7	457.0	27,900	35,750	61.1	78.2	928.6	61.50
8	517.7	31,000	35,750	60.0	72.7	1049.0	58.50
9	578.6	35,070	36,450	59.8	61.3	1213.7	57.40
10	556.1	31,350	37,500	56.3	67.4	1067.6	58.67
11	590.2	37,450	39,050	63.6	66.2	1295.8	60.80
12	611.3	41,250	40,750	67.4	66.7	1444.8	62.63
13	603.7	37,650	40,500	62.3	67.1	1253.0	61.07
14	592.6	34,050	43,200	58.4	73.0	1064.0	56.83
15	398.3	24,850	31,320	62.3	78.7	680.4	60.50
16	269.0	19,830	26,200	73.7	97.5	456.8	70.13

TABLE XX  
THERMAL CONTACT CONDUCTANCE RESULTS -  $40 \mu$  in. /  $40 \mu$  in.  
INTERFACE: 149.3 psi COMPRESSIVE LOAD

Data Point	$\Delta T_c$ °F	$(q/A)_A$ $\frac{\text{BTU}}{\text{hr-ft}^2}$	$(q/A)_B$ $\frac{\text{BTU}}{\text{hr-ft}^2}$	$(h_c)_A$ $\frac{\text{BTU}}{\text{hr-ft}^2\text{-}^\circ\text{F}}$	$(h_c)_B$ $\frac{\text{BTU}}{\text{hr-ft}^2\text{-}^\circ\text{F}}$	$T_m$ °F	$(h_c)_m$ $\frac{\text{BTU}}{\text{hr-ft}^2\text{-}^\circ\text{F}}$
1	95.9	12,230	13,420	127.5	139.9	266.4	133.7
2	110.9	16,900	17,770	152.4	160.2	344.8	156.3
3	187.2	25,650	22,200	137.0	118.7	495.8	127.9
4	224.5	29,350	31,100	131.0	138.7	605.0	134.9
5	283.5	32,100	36,550	113.2	129.0	752.9	121.1
6	292.3	35,660	42,200	122.0	144.3	868.2	133.2
7	295.5	41,000	46,400	138.7	157.2	991.3	148.0
8	307.6	44,200	47,800	143.7	155.5	1112.9	149.6
9	288.8	35,800	41,800	123.8	144.7	788.3	134.3
10	293.6	45,600	48,500	155.4	165.3	1122.4	160.4
14	355.7	46,500	46,850	130.8	132.0	1318.0	131.4
15	384.4	52,300	51,000	136.9	132.7	1606.4	134.8
19	98.8	17,210	14,780	174.7	149.5	346.1	162.1
20	236.6	26,950	28,600	114.0	121.0	772.8	117.5
21	350.0	35,300	37,900	102.5	108.3	1080.1	105.4

TABLE XXI

THERMAL CONTACT CONDUCTANCE RESULTS -  $40\mu$  in. /  $40\mu$  in.  
INTERFACE: 368.6 psi COMPRESSIVE LOAD

Data Point	$\Delta T_c$ ° F	$(q/A)_A$ $\frac{\text{BTU}}{\text{hr-ft}^2}$	$(q/A)_B$ $\frac{\text{BTU}}{\text{hr-ft}^2}$	$(h_c)_A$ $\frac{\text{BTU}}{\text{hr-ft}^2\text{-}^\circ\text{F}}$	$(h_c)_B$ $\frac{\text{BTU}}{\text{hr-ft}^2\text{-}^\circ\text{F}}$	$T_m$ ° F	$(h_c)_m$ $\frac{\text{BTU}}{\text{hr-ft}^2\text{-}^\circ\text{F}}$
1	40.7	12,030	6,440	295.7	158.3	352.1	227.0
2	89.0	21,630	17,700	243.4	199.0	646.2	221.2
3	153.5	25,500	25,350	166.2	165.3	988.7	165.8
4	187.3	29,600	28,050	158.0	149.7	1164.7	153.9
5	205.5	31,340	30,050	152.4	146.3	1280.0	149.4
6	247.4	37,250	35,360	150.6	143.0	1513.5	146.8
7	203.6	31,700	30,200	156.0	148.4	1264.5	152.2
8	257.9	38,720	36,400	150.3	136.0	1574.2	143.2
9	213.3	33,450	31,550	157.2	148.3	1305.6	152.8
10	126.9	22,700	24,900	179.0	196.0	898.0	187.5

TABLE XXII

THERMAL CONTACT CONDUCTANCE RESULTS -  $40 \mu$  in./ $40 \mu$  in.  
INTERFACE: 511.5 psi COMPRESSIVE LOAD

Data Point	$\Delta T_c$ ° F	$(q/A)_A$ $\frac{\text{BTU}}{\text{hr-ft}^2}$	$(q/A)_B$ $\frac{\text{BTU}}{\text{hr-ft}^2}$	$(h_c)_A$ $\frac{\text{BTU}}{\text{hr-ft}^2\text{-}^\circ\text{F}}$	$(h_c)_B$ $\frac{\text{BTU}}{\text{hr-ft}^2\text{-}^\circ\text{F}}$	$T_m$ ° F	$(h_c)_m$ $\frac{\text{BTU}}{\text{hr-ft}^2\text{-}^\circ\text{F}}$
1	31.2	13,100	--	420.0	--	348.6	420.0
2	66.5	21,400	17,000	320.0	256.5	595.5	288.3
3	130.4	28,350	20,850	217.5	160.0	895.2	188.8
4	144.2	29,050	29,050	201.4	201.4	1049.2	201.4
5	169.8	32,600	30,950	192.0	182.4	1201.8	187.2
6	204.6	38,000	34,600	185.6	169.2	1404.4	177.4
7	165.0	32,200	29,650	195.2	179.6	1181.2	187.4
8	224.9	42,150	38,300	187.3	170.3	1567.0	178.8

TABLE XXIII

THERMAL CONTACT CONDUCTANCE RESULTS -  $10 \mu$  in./ $10 \mu$  in.  
INTERFACE: 4.43 psia COMPRESSIVE LOAD

Data Point	$\Delta T_c$ °F	$(q/A)_A$ $\frac{\text{BTU}}{\text{hr-ft}^2}$	$(q/A)_B$ $\frac{\text{BTU}}{\text{hr-ft}^2}$	$(h_c)_A$ $\frac{\text{BTU}}{\text{hr-ft}^2\text{-}^\circ\text{F}}$	$(h_c)_B$ $\frac{\text{BTU}}{\text{hr-ft}^2\text{-}^\circ\text{F}}$	$T_m$ °F	$(h_c)_m$ $\frac{\text{BTU}}{\text{hr-ft}^2\text{-}^\circ\text{F}}$
11	42.52	4362	2709	102.6	63.7	239.3	83.15
12	70.85	6593	6203	93.1	87.6	389.7	90.35
13	103.1	8198	6528	79.5	63.3	535.5	71.40
14	128.3	10,050	7325	78.3	57.1	668.9	67.70
15	178.3	9838	8057	55.2	45.2	992.1	50.20
16	171.6	10,678	9452	62.2	55.1	971.6	58.65
17	203.3	13,080	11,460	64.4	56.3	1146.6	60.35
18	162.3	11,870	10,840	73.3	66.9	971.9	70.10
19	146.2	13,150	15,820	89.9	108.2	1071.2	99.50
20	129.6	7930	11,220	61.2	86.7	760.1	73.95
21	113.1	6260	5500	55.3	48.7	589.0	52.00
22	244.1	6800	3940	27.8	16.1	1610.4	21.45
23	26.8	3360	2760	125.3	103.0	228.5	114.15
24	101.4	12,400	9430	122.3	93.0	554.6	107.65
25	75.9	3220	1600	42.5	21.1	1262.2	31.80
26	144.4	8030	6280	55.6	43.5	1045.0	49.55
27	124.2	5700	2860	45.9	23.0	1457.0	34.45
28	177.1	3700	2050	20.9	11.7	1546.9	16.30
29	107.1	9060	10,680	84.5	99.5	659.1	92.0



TABLE XXIV

THERMAL CONTACT CONDUCTANCE RESULTS -  $10\ \mu$  in./ $10\ \mu$  in.  
INTERFACE: 64.7 psi COMPRESSIVE LOAD

Data Point	$\Delta T_c$ ° F	$(q/A)_A$ $\frac{\text{BTU}}{\text{hr-ft}^2}$	$(q/A)_B$ $\frac{\text{BTU}}{\text{hr-ft}^2}$	$(h_c)_A$ $\frac{\text{BTU}}{\text{hr-ft}^2\text{-}^\circ\text{F}}$	$(h_c)_B$ $\frac{\text{BTU}}{\text{hr-ft}^2\text{-}^\circ\text{F}}$	$T_m$ ° F	$(h_c)_m$ $\frac{\text{BTU}}{\text{hr-ft}^2\text{-}^\circ\text{F}}$
1	20.2	3792.0	3150.0	187.7	155.9	208.0	171.8
2	21.6	8526.0	8400.0	394.7	388.9	305.7	391.8
3	29.3	11,212	10,956	382.7	373.7	380.0	378.3
4	53.6	17,670	17,395	329.7	324.5	572.1	327.1
5	58.9	9126	9222	154.9	156.6	484.2	155.8
6	31.8	10,780	10,280	339.0	323.5	351.4	331.3
7	60.5	17,230	16,240	285.0	269.0	553.9	277.0
8	91.4	19,860	20,850	217.4	228.5	736.5	223.0
9	116.1	19,880	23,500	179.5	202.5	900.9	191.0
10	130.6	24,520	26,500	187.8	203.0	1053.6	195.4
11	145.6	27,400	28,850	191.3	203.6	1182.9	193.2
12	168.6	28,200	27,800	167.2	175.4	1308.7	166.1
13	163.9	32,250	33,000	197.0	202.5	1409.8	199.3
14	142.9	33,700	37,620	264.6	273.3	1545.3	249.8
15	159.6	26,200	27,400	164.2	171.8	1410.9	168.0
16	154.7	20,080	25,180	129.7	162.7	1176.5	146.2
17	150.9	19,270	20,040	127.6	133.0	1146.1	130.3
18	120.1	13,680	14,700	114.0	122.4	842.6	118.2
19	81.1	8,530	7880	105.2	97.2	507.8	101.2

TABLE XXV  
THERMAL CONTACT CONDUCTANCE RESULTS -  $10 \mu$  in./ $10 \mu$  in.  
INTERFACE: 148.7 psia COMPRESSIVE LOAD

Data Point	$\Delta T_c$ °F	$(q/A)_A$ $\frac{\text{BTU}}{\text{hr-ft}^2}$	$(q/A)_B$ $\frac{\text{BTU}}{\text{hr-ft}^2}$	$(h_c)_A$ $\frac{\text{BTU}}{\text{hr-ft}^2\text{-}^\circ\text{F}}$	$(h_c)_B$ $\frac{\text{BTU}}{\text{hr-ft}^2\text{-}^\circ\text{F}}$	T °F	$(h_c)_m$ $\frac{\text{BTU}}{\text{hr-ft}^2\text{-}^\circ\text{F}}$
1	11.8	8,480	7,860	719.0	666.5	187.3	453.2
2	19.1	11,330	10,370	593.0	543.0	245.2	568.0
3	26.1	14,450	14,200	553.0	544.0	317.9	548.5
4	39.8	16,680	15,320	418.0	385.0	404.9	401.5
5	47.8	18,200	16,080	379.8	336.2	466.4	358.0
6	71.3	23,400	22,400	328.0	313.8	618.3	320.9
7	105.0	24,850	25,200	236.6	240.0	769.8	238.3
8	139.4	25,200	25,200	180.5	180.5	943.5	180.5
9	149.2	27,550	20,080	184.5	206.5	1052.2	195.5
10	129.5	31,080	29,600	242.4	230.9	1180.8	236.7
11	127.4	34,200	33,950	287.6	276.2	1318.6	281.9
12	91.5	40,300	39,080	455.9	427.5	1469.5	449.0
13	89.0	32,950	36,750	370.5	412.5	1356.4	391.5
14	67.2	2,124	1,974	316.1	293.7	579.7	304.9

TABLE XXVI

THERMAL CONTACT CONDUCTANCE RESULTS -  $10 \mu$  in./ $10 \mu$  in.  
INTERFACE: 368.5 psia COMPRESSIVE LOAD

Data Point	$\Delta T_c$ °F	$(q/A)_A$ $\frac{\text{BTU}}{\text{hr-ft}^2}$	$(q/A)_B$ $\frac{\text{BTU}}{\text{hr-ft}^2}$	$(n_c)_A$ $\frac{\text{BTU}}{\text{hr-ft}^2\text{-}^\circ\text{F}}$	$(h_c)_B$ $\frac{\text{BTU}}{\text{hr-ft}^2\text{-}^\circ\text{F}}$	$T_m$ °F	$(h_c)_m$ $\frac{\text{BTU}}{\text{hr-ft}^2\text{-}^\circ\text{F}}$
1	6.4	7,500	6,970	1172.0	1054.0	165.2	1113.0
2	10.5	12,340	12,460	1175.0	1185.0	240.0	1180.0
3	23.7	19,000	19,530	801.5	824.5	368.8	813.0
4	38.7	26,700	26,750	690.0	692.0	549.4	691.0
5	66.0	29,450	31,420	446.5	476.5	743.8	461.5
6	96.4	30,700	32,650	318.5	338.8	947.7	328.7
7	98.5	35,850	36,860	395.4	375.9	1089.6	369.3
8	101.6	38,740	38,100	419.7	387.6	1225.8	403.7
9	63.4	45,450	46,400	793.1	757.1	1303.5	775.1
10	61.6	47,000	46,900	833.0	786.1	1398.5	809.5
11	71.1	38,650	42,000	638.6	621.9	1133.7	630.2
12	42.0	36,100	38,800	860.0	924.0	745.3	892.0
13	31.0	33,450	22,350	765.0	721.5	448.4	738.8

TABLE XXVII

THERMAL CONTACT CONDUCTANCE RESULTS -  $10\mu$  in./ $10\mu$  in.  
INTERFACE: 512.0 psia COMPRESSIVE LOAD

Data Point	$\Delta T_c$ °F	$(q/A)_A$ BTU hr-ft <sup>2</sup>	$(q/A)_B$ BTU hr-ft <sup>2</sup>	$(h_c)_A$ BTU hr-ft <sup>2</sup> -°F	$(h_c)_B$ BTU hr-ft <sup>2</sup> -°F	$T_m$ °F	$(h_c)_m$ BTU hr-ft <sup>2</sup> -°F
1	4.1	6,880	6,830	1678	1666	144.5	1672
2	5.1	9,220	9,160	1775	1762	180.1	1768.5
3	8.3	13,070	13,840	1574	1668	240.1	1621
4	15.4	19,570	20,550	1270	1333	359.4	1301.5
5	27.3	28,450	29,400	1042	1076	523.2	1059
6	43.7	33,600	36,500	768.5	834.5	715.8	801.5
7	61.4	36,150	40,000	588.5	652.0	898.1	620.3
8	60.3	39,850	43,350	661.0	718.0	1054.8	689.5
9	54.4	44,800	47,000	823	865	1183.8	844.0
10	51.3	49,150	50,700	958	988	1294.8	973
11	42.2	51,400	52,300	1218	1239	1403.9	1228.5
12	47.7	43,000	46,500	902.0	976.0	1114.1	939
13	31.4	32,816	35,245	1045.1	1122.5	623.1	1083.8

## REFERENCES

1. M. L. Minges, Thermal Contact Resistance - A Review of the Literature, AFML-TR-65-375, Vol I. (1966).
- 1a. E. J. Gilchrist, Experimental Interface Heat Transfer Contact Coefficients in the Minuteman Solid Rocket Nozzle, Report on Air Force Contract 04(694)-258, Aerojet General Corp. (1964).
2. E. Kreyszig, Advanced Engineering Mathematics, John Wiley and Sons, New York, N. Y. 1962.
3. A. Gray, G. B. Mathews, A Treatise on Bessel Functions, p 260, MacMillan and Co., Ltd., London, 1931.
4. E. Jahnke, F. Emde, Funktion entafeln, p 205, Dover Publications, New York, 1945.
5. R. W. Powell, "Armco Iron as a Thermal Conductivity Standard," Proc. 2nd Sym. Thermophysical Properties, p 455, (1962).
6. R. K. Day, R. J. Brown, J. F. Lynch, "Thermal Conductivity Measurements on ASTM C-25 Round Robin Samples," Progress Report, Proc 4th Thermal Cond. Conf., (1964).
7. R. W. Powell, "The Thermal Conductivity of Beryllia," Trans. Brit Ceramic Soc., 53, 389-97, (1954).
8. A. Goldsmith, et al., Thermophysical Properties of Solid Materials, Vol III-Ceramics, WADC TR 58-476, p VII-A-2-a, (1960).
9. R. E. Taylor, A High Temperature Thermal Conductivity Apparatus, ASD TDR 62-348, (1962).
10. E. J., Chapin, D. G. Howe, An Exploratory Study of Radiant Energy Transport in BeO, US Naval Research Laboratory Report 6195, (1965).
11. National Standard Reference Data System report No. NSRDS-NBS-8, Thermal Conductivity of Selected Materials, (Nov 1966).
12. R. P. Tye, "Preliminary Measurements on the Thermal and Electrical Conductivities of Molybdenum, Niobium, Tantalum and Tungsten," J. of the Less-Common Metals, 3, pp 13-18, (1961).
13. M. Cutler, "Small Area Contact Methods," Adv. Energy Conv., 2, 29-42, (1962).
14. G. L. Denman, Private Communication, August 1967.
15. M. J. Wheeler, Brit. J. Appl. Phys., 16, 365-376, (1965).
16. M. J. Wheeler, "Thermal Diffusivity at Incandescent Temperatures By a Modulated Electron Beam Technique," NPL Thermal Conductivity Conference, London (1964).

REFERENCES (CONTD)

17. C. K. Jun, M. Hoch, Thermal Conductivity of Tantalum, Tungsten, Rhenium in The Temperature Range 1500-2800° K, AFML-TR-66-367, (1966).
18. N. S. Rasor, J. D. McClelland, "Thermal Properties of Graphite, Molybdenum and Tantalum to Their Destruction Temperatures," International J. Phys and Chem. of Solids, 15, p 17-26, (1960).
19. Fansteel Metallurgical Corp. Data Sheet, (1960).
20. J. F. Archard, "Contact and Rubbing of Flat Surfaces," J. Appl. Phys., 24, No. 8, 981-988, (1958).
21. R. G. Wheeler, Thermal Contact Conductance, Harford Laboratories Operation, General Electric Co., AEC Report No. HW-53598, (1957).
22. F. Kottler, "Elektrostatik der Leiter," Handbuch der Physik, Band 12, 472-473, Springer, Berlin (1927).
23. W. T. Clark, R. W. Powell, "Measurement of Thermal Conduction by the Thermal Comparator," J. Sci Instr. (G.B.), 39, 545-551, (1962).
24. L. C. Roess, "Theory of Spreading Conductance," Appendix A, Unpublished Report, Beacon Laboratories of the Texas Company Beacon, New York.
25. A. M. Clausing, B. T. Chao, Thermal Contact Resistance in a Vacuum Environment, Department of Mechanical and Industrial Engineering, University of Illinois, Report No. ME-TN-242-1, (August 1963).
26. T. N. Cetinkale, M. Fishenden, "Thermal Conductance of Metal Surfaces in Contact," General Discussion on Heat Transfer, Conf. Inst. Mech. Eng. and ASME, (1951).
27. E. H. Kennard, Kinetic Theory of Gases, McGraw Hill Book Co., New York, N. Y. (1933).
28. A. C. Rapier, I. M. Jones, J. E. McIntosh, "The Thermal Conductance of UO<sub>2</sub>/Stainless Steel Interfaces," Int. J. Heat Mass Trans. 6, 397-416, (1963).
29. J. F. Lynch, C. G. Ruderer, W. H. Duckworth, Engineering Properties of Ceramics, AFML TR 66-52. Battelle Memorial Institute, (1966).
30. D. F. Stevison, Effect of Surface Roughness on the Reflectance of Refractory Metals, AFML TR 66-232, (1966).
31. W. H. Walker, W. K. Lewis, W. H. McAdams, E. R. Gilliland, Principles of Chemical Engineering, McGraw-Hill Book Co., Inc., New York, N. Y., (1937).
32. E. R. G. Eckert, R. M. Drake, Heat and Mass Transfer, McGraw-Hill Book Co., Inc., New York, N. Y., (1959).
33. J. J. Henry, Some Methods of Surface Analysis for the Prediction of Thermal Resistance of Metal Contacts, AEC Report No. NYO-9459, (1963).

## REFERENCES (CONTD)

34. H. S. Carslaw, J. C. Jaeger, Conduction of Heat in Solids, Oxford Clarendon Press, London, England, (1959).
35. E. Jahnke, F. Emde, Funktionentafeln, p. 205, Dover Publications, New York, N. Y. (1945).
36. A. Gray, G. B. Mathews, A Treatise on Bessel Functions, p. 260, MacMillan and Co., Ltd., London, (1931).
37. M. J. Laubitz, "A Note on the Thermal Conductivity of Powders in Vacuum," Proc. Third Conf. Thermal Cond, II, 628-635, (1963).
38. H. W. Godbee, W. T. Ziegler, "The Thermal Conductivity of MgO, Al<sub>2</sub>O<sub>3</sub>, and ZrO<sub>2</sub> Powders to 850° C," Proc Third Conf Thermal Cond, II, 557-612, (1963).
39. D. R. Flynn, J. Res NBS-C, Engg. and Inst., 67C(2), 129-137, (1963).
40. A. E. Wechsler, P. E. Glaser, Investigation of the Thermal Properties of High Temperature Insulating Materials, ASD-TDR-63-574, 91, (1963).
41. R. C. Folweiler, W. D. Kingery, Thermal Radiation Characteristics of Transparent and Translucent Materials, ASD-TDR-62-719, (1964).
42. Y. S. Touloukian, Editor, Thermophysical Properties of High Temperature Solid Materials, Vol 4, Part I, The MacMillan Co., New York, N. Y., (1967).
43. R. V. Dunkle, "Emissivity and Inter-Reflection Relationships for Infinite Parallel Specular Surfaces," Proc Sym Thermal Radiation of Solids, NASA special report SP-55, (1965).
44. O. H. Olson, J. C. Morris, Determination of Emissivity and Reflectivity Data on Aircraft Structural Materials, WADC TR 56-222, III, (1960).
45. R. L. Seifert, "The Spectral and Total Emissivity of Beryllium Oxide," Phys Rev, 73, (10), 1181-1187, (1948).
46. C. D. Pears, Southern Research Institute, ASD TDR 62-765, (1962).

UNCLASSIFIED

Security Classification

DOCUMENT CONTROL DATA - R&D		
(Security classification of title, body of abstract and indexing annotation must be entered when the overall report is classified)		
1. ORIGINATING ACTIVITY (Corporate author) Air Force Materials Laboratory Wright-Patterson Air Force Base, Ohio		2a. REPORT SECURITY CLASSIFICATION
		2b. GROUP
3. REPORT TITLE The Temperature Dependence of the Thermal Contact Resistance Across Nonmetallic Interfaces		
4. DESCRIPTIVE NOTES (Type of report and inclusive dates)		
5. AUTHOR(OR(S)) (Last name, first name, initial) Merrill L. Minges		
6. REPORT DATE June 1969	7a. TOTAL NO. OF PAGES	7b. NO. OF REFS 46
8a. CONTRACT OR GRANT NO.  a. PROJECT NO 7381  c. Task 738102  d.	9a. ORIGINATOR'S REPORT NUMBER(S) AFML-TR-69-1  9b. OTHER REPORT NO(S) (Any other numbers that may be assigned in a report)	
10. AVAILABILITY/LIMITATION NOTICES This document has been approved for public release and sale; its distribution is unlimited. In DDC. Avail from CFSTI.		
11. SUPPLEMENTARY NOTES	12. SPONSORING MILITARY ACTIVITY Air Force Materials Laboratory Wright-Patterson Air Force Base, Ohio	
13. ABSTRACT Extensive measurements of thermal contact resistance were conducted in the following study areas, where no previous systematic measurements have been performed: (1) interfaces consisting of brittle, nonmetallic components, and (2) radiative transport across the interface at high temperatures.  An apparatus for performing the measurements to elevated temperatures was designed, constructed, and performance tested. The equipment, operated in vacuum environments, utilized tantalum heaters to develop heat flow down a specimen column which was water cooled at its base. The contact resistance specimen column consisted of two high purity beryllium oxide cylinders, 1 inch in diameter and 1.5 inches in length. The successful performance of the apparatus was demonstrated by measuring the thermal conductivity of beryllium oxide and tantalum as a function of temperature. The beryllium oxide and tantalum conductivity results exhibited a precision of at least $\pm 2\%$ while the accuracy of the data was estimated to be $\pm 3\%$ by comparison with literature values.  Analytical predictions of heat losses from the specimen column were made through solution of the boundary-value problem for the temperature field in the insulation segment surrounding this column. The results compared favorably with experimental heat loss measurements.		

(Continued)



UNCLASSIFIED

Security Classification

14 KEY WORDS	LINK A		LINK B		LINK C	
	ROLE	WT	ROLE	WT	ROLE	WT
Thermal Contact Resistance Beryllium Oxide Tantalum Thermal Conductivity Interfacial Heat Transfer						

## INSTRUCTIONS

1. **ORIGINATING ACTIVITY:** Enter the name and address of the contractor, subcontractor, grantee, Department of Defense activity or other organization (corporate author) issuing the report.

2. **REPORT SECURITY CLASSIFICATION:** Enter the overall security classification of the report. Indicate whether "Restricted Data" is included. Marking is to be in accordance with appropriate security regulations.

2b. **GROUP:** Automatic downgrading is specified in DoD Directive 5200.10 and Armed Forces Industrial Manual. Enter the group number. Also, when applicable, show that optional markings have been used for Group 3 and Group 4 as authorized.

3. **REPORT TITLE:** Enter the complete report title in all capital letters. Titles in all cases should be unclassified. If a meaningful title cannot be selected without classification, show title classification in all capitals in parenthesis immediately following the title.

4. **DESCRIPTIVE NOTES:** If appropriate, enter the type of report, e.g., interim, progress, summary, annual, or final. Give the inclusive dates when a specific reporting period is covered.

5. **AUTHOR(S):** Enter the name(s) of author(s) as shown on or in the report. Enter last name, first name, middle initial. If military, show rank and branch of service. The name of the principal author is an absolute minimum requirement.

6. **REPORT DATE:** Enter the date of the report as day, month, year, or month, year. If more than one date appears on the report, use date of publication.

7a. **TOTAL NUMBER OF PAGES:** The total page count should follow normal pagination procedures, i.e., enter the number of pages containing information.

7b. **NUMBER OF REFERENCES:** Enter the total number of references cited in the report.

8a. **CONTRACT OR GRANT NUMBER:** If appropriate, enter the applicable number of the contract or grant under which the report was written.

8b, 8c, & 8d. **PROJECT NUMBER:** Enter the appropriate military department identification, such as project number, subproject number, system numbers, task number, etc.

9a. **ORIGINATOR'S REPORT NUMBER(S):** Enter the official report number by which the document will be identified and controlled by the originating activity. This number must be unique to this report.

9b. **OTHER REPORT NUMBER(S):** If the report has been assigned any other report numbers (either by the originator or by the sponsor), also enter this number(s).

10. **AVAILABILITY/LIMITATION NOTICES:** Enter any limitations on further dissemination of the report other than those

imposed by security classification, using standard statements such as:

- (1) "Qualified requesters may obtain copies of this report from DDC."
- (2) "Foreign announcement and dissemination of this report by DDC is not authorized."
- (3) "U. S. Government agencies may obtain copies of this report directly from DDC. Other qualified DDC users shall request through \_\_\_\_\_."
- (4) "U. S. military agencies may obtain copies of this report directly from DDC. Other qualified users shall request through \_\_\_\_\_."
- (5) "All distribution of this report is controlled. Qualified DDC users shall request through \_\_\_\_\_."

If the report has been furnished to the Office of Technical Services, Department of Commerce, for sale to the public, indicate this fact and enter the price, if known.

11. **SUPPLEMENTARY NOTES:** Use for additional explanatory notes.

12. **SPONSORING MILITARY ACTIVITY:** Enter the name of the departmental project office or laboratory sponsoring (paying for) the research and development. Include address.

13. **ABSTRACT:** Enter an abstract giving a brief and factual summary of the document indicative of the report, even though it may also appear elsewhere in the body of the technical report. If additional space is required, a continuation sheet shall be attached.

It is highly desirable that the abstract of classified reports be unclassified. Each paragraph of the abstract shall end with an indication of the military security classification of the information in the paragraph, represented as (TS), (S), (C), or (U).

There is no limitation on the length of the abstract. However, the suggested length is from 150 to 225 words.

14. **KEY WORDS:** Key words are technically meaningful terms or short phrases that characterize a report and may be used as index entries for cataloging the report. Key words must be selected so that no security classification is required. Identifiers, such as equipment model designation, trade name, military project code name, geographic location, may be used as key words but will be followed by an indication of technical context. The assignment of links, rules, and weights is optional.

UNCLASSIFIED

Security Classification